

DEAN  
28 Sept 93

**ELECTROCHEMICAL STUDIES OF THE HYDROGEN SORPTION  
AND THE IODINE OXIDATION REACTIONS ON PLATINUM**

by

**Tarek Rafic Farhat  
B.Sc., Thames Polytechnic, 1989**

**A Thesis Submitted in Partial Fulfillment of the  
Requirements for the Degree of**

**MASTER OF SCIENCE**


**in the Department of Chemistry**

**We accept this thesis as conforming  
to the required standard**

  
Dr. D.A. Harrington, Supervisor (Department of Chemistry)

  
Dr. T.E. Gough, Departmental Member (Department of Chemistry)

  
Dr. G.A. Beer, Outside Member (Department of Physics)

  
Dr. A. Watton, External Examiner (Department of Physics)

© TAREK RAFIC FARHAT, 1993

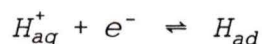
University of Victoria

QD181  
P8F3

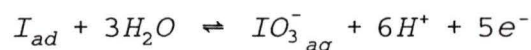
Supervisor : Dr. David A. Harrington

ABSTRACT

The kinetics of the hydrogen sorption reaction,



and the iodine oxidation reaction,



on polycrystalline platinum were studied using cyclic voltammetry, a.c. voltammetry, and potential sweep-step measurements. The hydrogen sorption reaction is fast and required development of a rapid response, low noise potentiostat for its study. For this purpose a combined electrochemical-potentiostatic system was theoretically simulated in order to study the effect of the instrumental and non-faradaic parameters on the response time of this system. The non-faradaic parameters are the solution or electrolyte resistance and the double-layer capacitance which develops at the electrode/solution interface.

From the simulation, the instrumental and electrochemical parameters of the potentiostat and the electrochemical cell,

respectively, were optimized for the best response. The design of an optimized, compatible potentiostat is proposed.

The hydrogen sorption reaction was studied using the Potential Sweep-Step method. The method was successful in elucidating the values of both forward and reverse rate constants. The Langmuir isotherm was found to hold approximately for the adsorbed hydrogen, though there is some evidence for small lateral interactions between adsorbates. The validation of this technique in this work makes it a strong candidate for future combined electrochemistry/ultra high vacuum work. The variation of the overall rate constant with electrode potential, at different concentrations of acid solutions, was also determined.

The a.c. voltammetry technique was used to study the iodine oxidation reaction on polycrystalline platinum. A single relaxation process was found, having an equivalent circuit consisting of the double layer capacitance in parallel with a faradaic resistance and a faradaic capacitance. These results were interpreted in terms of a multi-step mechanism, in which the first step is a rate determining charge transfer step ( $\beta=0.63$ ) which is second order in iodine coverage. The same mechanism also quantitatively explains the shape of the d.c. cyclic voltammogram.

Examiners :

Dr. D.A. Harrington, Supervisor (Department of Chemistry)

Dr. T.E. Gough, Departmental Member (Department of Chemistry)

Dr. G.A. Beer, Outside Member (Department of Physics)

Dr. A. Watton, External Examiner (Department of Physics)

## Table of contents

Abstract	(ii)
Table of contents	(v)
List of tables	(ix)
List of figures	(x)
List of symbols	(xvi)
Acknowledgements	(xxi)

### CHAPTER 1:

#### Introduction

	Page
1.1) The hydrogen sorption reaction on platinum.	1
1.1.1) Purpose of designing a fast response potentiostat.	2
1.1.2) Analysis on the kinetics of the hydrogen sorption reaction.	3
1.2) The iodine oxidation reaction on platinum.	7

### CHAPTER 2:

#### Experimental

2.1) Introduction	14
2.2) The electrochemical cell	14

2.3) Instrumentation used to monitor the hydrogen sorption reaction on platinum	16
2.4) Instrumentation used to monitor the iodine oxidation reaction on platinum	17

### CHAPTER 3:

#### Potentiostatic Circuit Analysis

3.1) Introduction	21
3.2) Theory	30
3.2.1) Transfer function (TF)	31
3.2.2) System stability	38
3.2.3) Frequency-domain response analysis on the TF of the CEP system	42
3.2.4) Time domain response analysis on the response of the CEP system to a step signal	45
3.3) Results, discussion, and conclusion	48
3.3.1) Bode plots	48
3.3.2) Voltage and current responses due to an input step signal	58
3.4) Circuit Design	69
3.4.1) Brief review of potentiostat design	70
3.4.2) Design requirements and circuit layout	71

## CHAPTER 4:

The Hydrogen Sorption Reaction

4.1) Introduction	76
4.2) Experimental procedure	77
4.3) Theory	79
4.4) Results and discussion	86
4.5) Conclusion	97

## CHAPTER 5:

The Iodine Oxidation Reaction

5.1) Introduction	100
5.2) Experimental procedure	102
5.3) Results	105
5.4) Theory	115
5.4.1) Derivation of the magnitude of the impedance and the phase from experimental results	115
5.4.2) Devising a reaction mechanism for the iodine oxidation reaction	116
5.4.3) Reaction kinetics	119
5.4.4) Simulating the d.c. cyclic voltammogram	120
5.4.5) A.C. impedance analysis	123
5.5) Discussion	137
5.5.1) Examining the d.c. cyclic voltammogram	137

	viii
5.5.2) Examining the a.c. cyclic voltammogram	138
5.5.3) Examining the Bode plots	139
5.5.4) The reaction mechanism and kinetics	141
5.6) Conclusion	142
CHAPTER 6:	
<u>CONCLUSION</u>	144
REFERENCES:	147
APPENDIX I:	152

List of Tables

	Page
Table 3.1 Bode parameters, output current and response time of the CEP system.	50
Table 4.1 Total charge under the decay current signal	88
Table 4.2 Total charge between $E_b$ and $E_h$	88
Table 5.1 Instrumental settings of the a.c. impedance experiment	104

LIST OF FIGURES

	Page
Chapter 1 :	
Figure 1.1 Cyclic voltammogram of polycrystalline platinum in 2M H <sub>2</sub> SO <sub>4</sub> solution.	3
Chapter 2 :	
Figure 2.1 Schematic of the instrumental setup used to study the hydrogen sorption reaction on the platinum surface.	19
Figure 2.2 Schematic of the instrumental setup used to study the iodine oxidation reaction on the platinum surface.	20
Chapter 3 :	
Figure 3.1 Basic Op-amp circuit, inverting configuration	22
Figure 3.2 Schematic of the circuit for a single Op-amp potentiostat	23
Figure 3.3 Circuit of the combined electrochemical cell and potentiostat (CEP)	26
Figure 3.4 Schematic of the potentiostatic response for a perfect electrochemical system	28
Figure 3.5 Schematic of the potentiostatic response for a real electrochemical system	28
Figure 3.6 The RC circuit	31
Figure 3.7 The complex s-plane	39

Figure 3.8 Bode plot of the frequency dependence of the gain	44
Figure 3.9 Flow diagram of transform analysis	46
Figure 3.10 Frequency dispersion of the transfer function at the RE. Variation with the d.c. gain of the op-amp.	51
Figure 3.11 Frequency dispersion of the transfer function at the RE. Variation with the break frequency of the op-amp.	52
Figure 3.12 Frequency dispersion of the transfer function at the RE. Variation with the uncompensated resistance.	53
Figure 3.13 Frequency dispersion of the transfer function at the RE. Variation with the double-layer capacitance at the CE.	54
Figure 3.14 Frequency dispersion of the transfer function at the RE. Variation with the solution resistance.	55
Figure 3.15 Frequency dispersion of the transfer function at the RE. Variation with the double-layer capacitance at the WE.	56
Figure 3.16 Frequency dispersion of the transfer function at the RE. Variation with the load resistance.	57
Figure 3.17 Response plots of the voltage output at the RE, and current output of the CA. Variation with the d.c. gain of the op-amp.	60

Figure 3.18 Response plots of the voltage output at the RE, and current output of the CA. Variation with the break frequency of the op-amp.	61
Figure 3.19 Response plots of the voltage output at the RE, and current output of the CA. Variation with the uncompensated resistance.	62
Figure 3.20 Response plots of the voltage output at the RE, and current output of the CA. Variation with the double-layer capacitance at the CE.	63
Figure 3.21 Response plots of the voltage output at the RE, and current output of the CA. Variation with the solution resistance.	64
Figure 3.22 Response plots of the voltage output at the RE, and current output of the CA. Variation with the double-layer capacitance at the WE.	65
Figure 3.23 Response plots of the voltage output at the RE, and current output of the CA. Variation with the load resistance.	66
Figure 3.24 Response plots of the current output of the CA using high load resistance.	70
Figure 3.25 Fast response, Low noise potentiostat [ Circuit layout ]	74
Figure 3.26 Fast response, Low noise potentiostat [ Circuit board ]	75

## Chapter 4 :

Figure 4.1 Schematic of the Sweep-Step signal used in the Sweep-Step method	77
Figure 4.2 A plot of the decay current due to H-desorption on platinum	78
Figure 4.3 Schematic showing the change of coverage with potential	81
Figure 4.4 Schematic showing the change of overall rate constant with potential	82
Figure 4.5 Cyclic voltammogram of polycrystalline platinum in 1M H <sub>2</sub> SO <sub>4</sub> solution.	84
Figure 4.6 A plot of ln(j) vs Time	86
Figure 4.7 A plot of $k/\Gamma_m$ vs $E_h$ in 1M HClO <sub>4</sub> for $\pm 10$ mV potential steps.	90
Figure 4.8 A plot of $k/\Gamma_m$ vs $E_h$ in 2M H <sub>2</sub> SO <sub>4</sub> for $\pm 10$ mV potential steps.	91
Figure 4.9 A plot of $k/\Gamma_m$ vs $E_h$ in 4M H <sub>2</sub> SO <sub>4</sub> for $\pm 20$ mV potential steps.	92
Figure 4.10 A plot of $k/\Gamma_m$ vs $E_h$ in 6M H <sub>2</sub> SO <sub>4</sub> for $\pm 20$ mV potential steps.	93
Figure 4.11 A plot of $k/\Gamma_m$ vs $E_h$ in 4M H <sub>2</sub> SO <sub>4</sub> for potential steps of +5, +10, +15, and +20 mV.	94

## Chapter 5 :

Figure 5.1 Nyquist plot of impedance of the expected reaction mechanism of iodine oxidation on platinum	101
---	-----

Figure 5.2 D.c. cyclic voltammogram of iodine oxidation on platinum.	106
Figure 5.3 A.c. cyclic voltammograms of iodine oxidation on platinum (from 5 to 500 Hz)	107
Figure 5.4 A.c. cyclic voltammograms of iodine oxidation on platinum (from 0.5 to 7.5 kHz)	108
Figure 5.5 A.c. cyclic voltammograms of platinum oxidation in pure sulfuric acid solution, $0.5 \text{ mol dm}^{-3}$ (from 2 to 100 Hz)	109
Figure 5.6 Bode plots of the impedance for the iodine monolayer	110
Figure 5.7 Bode plots of the impedance for iodine oxidation on platinum	111
Figure 5.8 Bode plots of the impedance after completion of the iodine oxidation	112
Figure 5.9 Bode plots of the impedance during the reduction of PtO	113
Figure 5.10 Nyquist plot of impedance of the observed reaction mechanism of iodine oxidation on platinum	114
Figure 5.11 Schematic of the likely mechanisms of the iodine oxidation reaction	118
Figure 5.12 The simulated d.c. cyclic voltammogram	123
Figure 5.13 Equivalent circuit for the iodine oxidation reaction	129
Figure 5.14 CPE sample plots to determine $\varphi$ and the double-layer capacitance	131

Figure 5.15 CPE sample plots to determine the faradaic resistance	132
Figure 5.16 Change in the double-layer capacitance with potential during the iodine oxidation reaction	133
Figure 5.17 Change in the faradaic resistance with potential during the iodine oxidation reaction	134
Figure 5.18 The observed a.c. cyclic voltammograms of iodine oxidation on platinum	135
Figure 5.19 The calculated a.c. cyclic voltammograms of iodine oxidation on platinum	137

LIST OF SYMBOLS

- A Surface area of the working electrode.
- $A_v$  Integral area (V s) under a cyclic voltammogram peak.
- B Transfer function of the dummy cell at  $e_{out}$ .
- C Capacitance, Capacitance at the counter electrode.
- CA Control amplifier.
- $C_d$  Double-layer capacitance at the working electrode.
- CE Counter electrode.
- CEP Combined electrochemical-potentiostatic system.
- $C_f$  Faradaic capacitance.
- $C_h$  Double-layer capacitance of the oxide adlayer.
- $C_l$  Double-layer capacitance of the iodine adlayer.
- CV Cyclic Voltammogram.
- D Denominator.
- $e_c$  Potential between load resistance and capacitance at counter electrode.
- $e_d$  Potential between uncompensated resistance and capacitance at the working electrode.
- $e_i$  Input voltage signal.
- $e_{op}$  Potential at the output of the control amplifier.
- $e_{out}$  Potential at the tip of the luggin probe.
- $e_s$  Potential at virtual ground.
- $e_t$  Potential between C and solution resistance.
- $e^+$  Potential at the positive input of the control amplifier.

$e^-$	Potential at the negative input of the control amplifier.
$E$	Electrode potential.
$E_b$	Sweep potential before a potential step.
$E_h$	Hold potential after a potential step.
$E_p$	Peak potential.
$E_{RE}$	Potential at the surface of the reference electrode.
$E_s$	Starting potential of the sweep.
$E_{WE}$	Potential at the surface of the working electrode.
$E^\circ$	Standard potential.
$F$	Faraday constant.
$f$	Frequency in Hz.
$f_b$	Break frequency.
FG	Function Generator.
$G$	Gain.
$g$	D.c. gain.
$G(i\omega)$	Transfer function in the frequency domain.
$G(s)$	Transfer function in the $s$ domain.
$G(t)$	Transfer function in the time domain.
$H_{(ad)}$	Hydrogen adsorbed to a metal.
$I$	Current.
$I_c$	Electrochemical current.
$I'$	Real part of a sinusoidal current.
$I''$	Imaginary part of a sinusoidal current.
$j$	Current density.
$j_0$	Current density at time $t=0$ .

$k$	Overall rate constant.
$k_s$	Rate constant at starting potential.
$k^\circ$	Standard overall rate constant.
$k^1$	Forward rate constant.
$k^{-1}$	Reverse rate constant.
$k_1^p$	Forward rate constant at peak potential.
$k_1^\circ$	Standard forward rate constant.
$k_{-1}^\circ$	Standard reverse rate constant.
$\mathcal{L}$	Laplace transform operator.
$\mathcal{L}^{-1}$	Inverse Laplace transform operator.
LIA	Lock-in-amplifier.
LP	Luggin probe.
$n$	Number of electrons per adsorbate.
Pt(111)	Single crystal platinum of (111) facet and (111) is (hkl) in miller indices.
$Q_c$	Amount of charge under a portion of the CV.
$Q_d$	Amount of charge under the decay curve.
$r_{(rds)}$	Rate of the rate determining step.
$R$	Gas constant, electrical resistance.
RE	Reference electrode.
$R_f$	Faradaic resistance.
$R_1$	Current measuring resistor, or load resistance.
$R_t$	Solution resistance between the counter and reference electrodes.
$R_u$	Solution resistance between the reference and working electrodes.

s	Laplace s notation.
S	Virtual ground in a circuit network.
SG	Step generator.
T	Temperature in degree Kelvin.
TF	Transfer function.
u(t)	Unit step function.
UHP	Ultra High Purity.
UHV	Ultra High Vacuum.
V	Voltage.
VF	Voltage follower.
$V_i$	Input voltage signal.
$V_{out}$	Output voltage signal.
$V_{rms}$	Root mean squared voltage.
$V_{supply}$	Supply voltage.
$V'$	Real part of a sinusoidal voltage.
$V''$	Imaginary part of a sinusoidal voltage.
WE	Working electrode.
Y	Admittance.
$Y_f$	Faradaic admittance.
$Y_{f-Cd}$	Faradaic and double-layer admittance.
$Y_T$	Total admittance.
$Y'$	Real part of the admittance.
$Y''$	Imaginary part of the admittance.
Z	Impedance.
$ Z $	Magnitude of the impedance.
$Z_{f-Cd}$	Faradaic and double-layer impedance.

$Z_T$	Total impedance.
$\beta$	Symmetry factor.
$\Gamma_m$	Surface concentration of a monolayer of adsorbate.
$\theta$	Surface coverage.
$\nu$	Sweep rate.
$\pi$	Pi=3.1416...
$\sigma$	Charge density.
$\sigma_m$	Charge density of a monolayer of adsorbate.
$\phi$	Phase angle.
$\varphi$	Constant phase element coefficient.
$\omega$	Frequency in $\text{rad s}^{-1}$ .

ACKNOWLEDGEMENTS

I would like to thank my supervisor Dr. David A. Harrington for his help and guidance throughout the course of this work. I would also like to express my thanks to Scott Furman and Sandra Shaub's. I would like to thank all the members of the department, graduate students, and the technical support staff who have contributed to the work presented in this thesis. In particular, I would like to thank Bob Dean and David Searle.

I would also like to pass my regards to Amirosh, Muhamad, Aref, Fathi, Abdul Kadder, Abul Kassem, Naser, and Majed for their kind help and support.

**TO MY PARENTS  
BROTHERS AND SISTERS**

## CHAPTER ONE

INTRODUCTION

Two different electrochemical reactions on polycrystalline platinum were investigated in this project. These are the hydrogen sorption reaction and the iodine oxidation reaction.

1.1) The hydrogen sorption reaction on platinum :

The hydrogen sorption reaction on polycrystalline platinum in acid solution is studied in this work,



The forward reaction is adsorption, where  $H_{(aq)}^{+}$  is an  $H_3O^{+}$  ion in solution that adsorbs on a platinum site  $Pt_{(s)}$  to form an adatom  $PtH_{(ad)}$ . For this reaction, we discuss the design of a fast response potentiostat which is compatible with transient techniques (e.g. Sweep-Hold and Sweep-Step methods). Then thorough analysis is made on the kinetics of this reaction using the Sweep-Step method. We have conveniently discussed the instrumentation in Chapter 3, and analysed the kinetics in Chapter 4.

### 1.1.1) Purpose of designing a fast response potentiostat :

In electrochemistry, there are some electrochemical reactions that are quite fast, for example, the hydrogen sorption reaction. In order to study fast electrochemical reactions, a fast-response potentiostat with the minimum level of noise is required.

Thorough research [1-12] work has been done in this field and the basic theory is well established [13,14]. However, in this area of research experimentalists cannot usually rely on other people's work to apply to their electrochemical system under study. This is because different groups are confronted with different electrochemical problems in their own area of research. For example, there are many papers dealing with transient response in polarographic techniques, yet the theoretical and experimental analyses are different even within this one area [2,5,7]. This difference is simply attributed to different instrumental designs and electrochemical parameters used in various research projects.

In this study, the parameters associated with the electrochemical system used in our research laboratory were considered. These parameters are properly defined in figure 3.3. Response plots which characterise the effect of each of these parameters on the transient response of the combined electrochemical potentiostatic (CEP) system (fig 3.3), will be presented and discussed in Chapter 3. Finally, the optimum design of a fast response potentiostat will be outlined.

1.1.2) Applying the Sweep Step method to study the hydrogen sorption reaction on platinum.

The underpotential deposition (UPD) reaction, of  $H^+$  at potential positive relative to a reference hydrogen electrode (RHE) was originally studied by Will and Knorr [15] in their pioneering work on cyclic voltammetry. Further work was done by Conway's group [16-19]. On polycrystalline platinum surfaces the cyclic voltammogram shows two oxidation peaks for hydrogen desorption in the voltage range 0.0-0.45 V vs RHE, (fig. 1.1). The corresponding reductive adsorption peaks are almost a mirror image of the oxidation peaks, indicating that

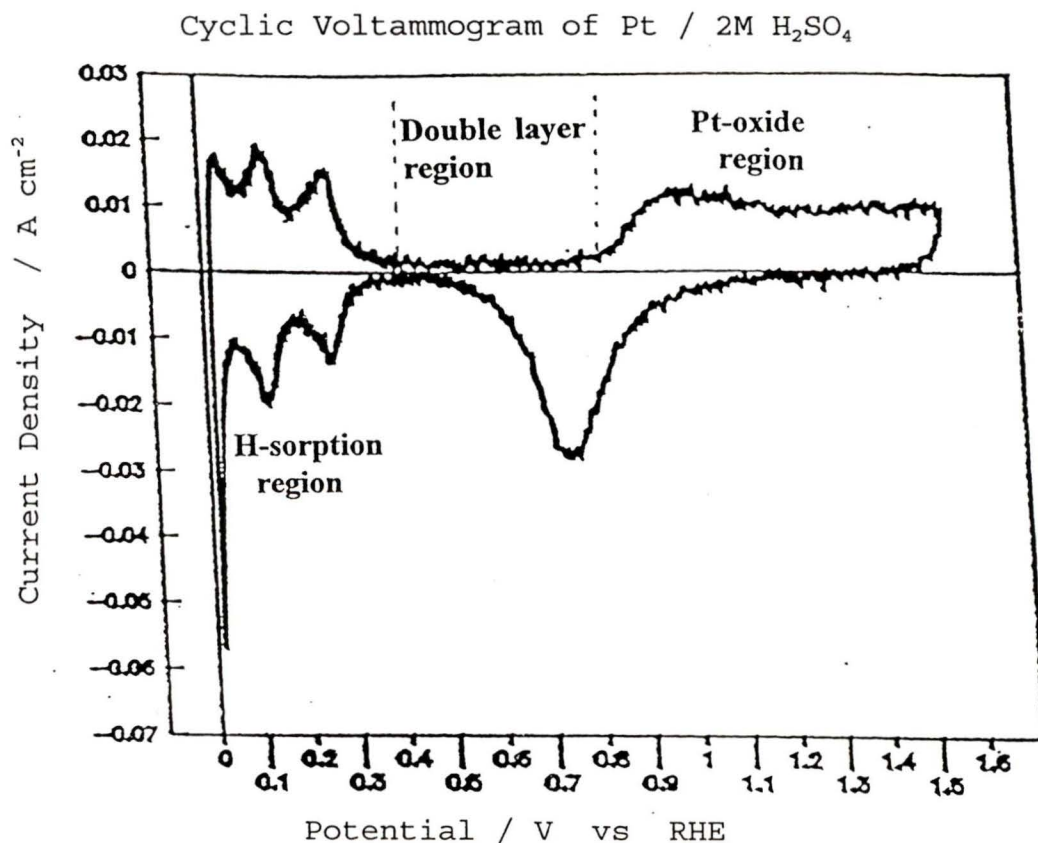


Figure 1.1 Cyclic voltammogram of Pt in 2M  $H_2SO_4$  solution.

the reaction is close to equilibrium under these conditions.

The presence of two peaks shows that there are at least two types of adsorption sites for the hydrogen. The position of the peaks can be related to the bond strength, the more positive peak corresponding to the more strongly adsorbed hydrogens. The free energy of hydrogen adsorption in both the electrochemical and gas phase experiments has been estimated at about  $50 \text{ kJ mol}^{-1}$  [20,21].

The area under the peaks may be converted to a charge density of about  $220 \text{ } \mu\text{C cm}^{-2}$  [22]; this corresponds to one hydrogen per platinum atom [23]. In gas phase work, on many metals, hydrogen shows a preference for sites with a high coordination number [24], and we may expect the same to be true also at the electrochemical interface. It is difficult to find techniques which can examine the environment of hydrogen on Pt in the presence of the electrolyte solution, so that most of the evidence regarding the nature of the adsorbed species is indirect. Ultra-High-Vacuum (UHV) surface science studies of platinum electrodes, after electrochemical treatment [25,26], compared single-crystal with polycrystalline platinum electrodes and concluded that the two peaks on the polycrystalline surface correspond to sites similar to those on Pt(111) (weakly bound  $\text{H}_{(\text{ad})}$ ) and Pt(100) (strongly bound  $\text{H}_{(\text{ad})}$ ). Earlier work had suggested instead that the weakly bound sites were of Pt(110) character [27].

More recent work has involved detailed comparisons of voltammograms for different well-characterised single-crystal surfaces, and has enabled identification of specific peaks with specific step and terrace surface sites [20,22,28-35]. The most detailed analyses have been given by Clavilier [22,36]. The acidic electrolyte solutions provide anions which alter the shapes of the H-peaks substantially. Extensive work has been done to understand the nature of this interaction [23,36,37]. Several survey papers have appeared [24,38-chaps. 3,14,34], which address the nature of the "anomalous" Pt(111) high-energy peak found only in perchlorate solutions.

The adsorbed hydrogen intermediate in the hydrogen evolution reaction has been detected directly by FTIR by Nicholas and Bewick [39], where it appeared to be adsorbed on an atop site. However the hydrogen evolution reaction occurs at more negative potentials where the surface is already covered with UPD hydrogen, and the UPD hydrogen is more likely to be in three-fold or four-fold hollow sites. UPD hydrogen has been detected directly by second-harmonic generation (SHG), but this does not provide details on the type of bond [38-chap20].

Despite much work directed at determining the structure and bonding of adsorbed hydrogen, less work has been done on quantitative determination of the rate parameters for this reaction. Using the sweep rate dependence of the peaks in cyclic voltammetry, Conway [40] has determined the rate

constants at the standard conditions of half coverage (for different type of sites) and  $[H^+] = 1 \text{ mol dm}^{-3}$  to be  $5 \text{ to } 6 \times 10^{-6} \text{ mol cm}^{-2} \text{ s}^{-1}$ . A.C. impedance methods have also been used [41-45] with quantitative analysis yielding rate constants of  $76 \times 10^{-6} \text{ mol cm}^{-2} \text{ s}^{-1}$  [41], and  $4.5 \times 10^{-6} \text{ mol cm}^{-2} \text{ s}^{-1}$  [42]. Coulostatic measurements have also been used giving  $5.8 \times 10^{-6} \text{ mol cm}^{-2} \text{ s}^{-1}$  [46].

Because of the wide range in literature values we chose to use a sweep-step measurement to obtain the rate constant. This method has the advantage of simplifying the analysis since the measurements are done at constant potential, and the coverage region probed is well defined. Because of the simpler mathematical analysis it should also be possible to determine the type of isotherm, which reflects the type of lateral interactions between adsorbed molecules. Of the above kinetic studies, Conway's method [18] is insensitive to the type of isotherm, and the others have assumed the Langmuir isotherm (i.e. no lateral interactions). The only other work concerning the type of isotherm is that of Clavilier [22] where the shapes of the peaks on single crystal surfaces are analysed in terms of the Frumkin-Fowler isotherm.

In this project, the Sweep-Step method was proposed to elucidate the values of all the kinetic parameters that characterise this reaction. These parameters are the overall rate constant, and the symmetry and lateral-interaction factors. Moreover, through this technique the change of the

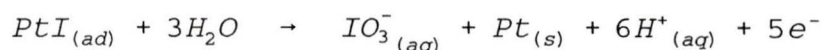
rate constant with electrode potential can be examined.

UHV/Electrochemical studies require an electrochemical method to study reaction kinetics which is simple and fast to operate. Electrochemical methods like a.c. voltammetry, and potentiodynamic techniques are slow to operate, and may fail to produce values of all kinetic parameters.

The hydrogen sorption reaction has also been studied at different concentrations [46] and the dependence of the current density on concentration was determined. In this project, the change of the overall rate constant with concentration was examined. This type of experiment enables us to determine the absolute values of the forward and backward rate constants separately, and confirm the functional dependence of the rate constant with potential at different concentrations.

### 1.2) Applying the a.c. impedance method to study the iodine oxidation reaction on polycrystalline platinum.

The iodine oxidation reaction on polycrystalline platinum studied in this work is :



where  $PtI_{(ad)}$  is an iodine adatom adsorbed on a Pt surface site. It is oxidised to the iodate anion ( $IO_3^-$ ), leaving an

empty  $Pt_{(s)}$ . Coulometric measurements [47-50] have shown that the oxidation of  $I_{(ad)}$  to aqueous  $IO_3^-$  involves  $5e^-$ . The reagent  $PtI_{(ad)}$  is a monolayer of chemisorbed iodine which forms spontaneously when a platinum electrode is immersed in iodide ( $I^-$ ) solution :



The chemisorbed layer can withstand rinsing with aqueous electrolytes [48,49,51,52]. Evidence for strong adsorption of iodine on polycrystalline platinum has been reported, based upon radiotracer [53-55] and volumetric data [47,56-58], and it is known that the bond is of a covalent nature [49]. There is also considerable evidence that upon chemisorption the  $I^-$  is converted to a neutral species of zero valency [48-51,59,60]. The zero valency has been verified by thin layer coulometric measurements [48] and XPS [49]. Later work [61-63] with single crystals showed that exposure of Pt(111) and Pt(110) to any of the reagents  $I_{2(g)}$ ,  $HI_{(g)}$  or  $I^-_{(aq)}$  gave the same zero valent neutral species (i.e.  $I_{(ad)}$ ).

Early work suggested the amount of  $I_{(ad)}$  in a non-electroactive state was  $2 \times 10^{-9}$  mol  $cm^{-2}$ , and an additional  $1 \times 10^{-9}$  mol  $cm^{-2}$  was present in an electroactive state [47]. A later paper, [48], estimated that the surface excess of  $I_{(ad)}$  approaches a limiting value of  $1 \times 10^{-9}$  mol  $cm^{-2}$ , suggesting one  $I_{(ad)}$  for every two platinum surface atoms i.e.  $\theta_I = 0.5$ . These

values have been superseded by more recent work [49,64-66] in which the packing density of iodine on polycrystalline platinum and Pt(111) was determined at potentials between -0.78 to +0.72 V vs RHE where its surface concentration changed from 0.0 nmol cm<sup>-2</sup> to 1.4 nmol cm<sup>-2</sup> respectively. The maximum I<sub>(ad)</sub> packing density in these experiments was  $\theta_I=0.44$ , i.e. 0.44 I atoms per Pt atom. A hexagonal close packed layer of spheres touching at the Van der Waal radius of iodine, 0.215 nm [67], would give  $\theta_I=0.42$  [66], suggesting that the spacing in the real structure is dominated by Van der Waal interactions.

Ordered adsorbed layers of iodine are formed on Pt(111) when it is immersed in iodide solution [66]. Structures and compositions of the iodine atomic layer formed by treatment of Pt(111) or Pt(100) with HI or I<sub>2</sub> in UHV has been studied by Low Energy Electron Diffraction (LEED), Auger Electron Spectroscopy (AES) and Thermal Desorption Mass Spectrometry (TDS) [61,63]. When Pt(111) is immersed in I<sup>-</sup> solution, with no applied potential bias, the ( $\sqrt{7}\times\sqrt{7}$ )R19° structure is formed. It is a hexagonal close packed layer of iodine atoms separated by the Van der Waal diameter. After cycling the potential, the iodine is found in a mixed [(3×3)R30° + ( $\sqrt{7}\times\sqrt{7}$ )R19°] lattice [63,68-70]. On the basis of LEED data [65,66], the I<sub>(ad)</sub> adlattice structure was potential dependent: a (3×3) adlattice ( $\theta_I=4/9$ ) at relatively positive potentials; a ( $\sqrt{7}\times\sqrt{7}$ )R19° adlattice ( $\theta_I=3/7$ ) at potentials in mid-range;

$(\sqrt{3}\times\sqrt{3})R30^\circ$  adlattice ( $\theta_I=1/3$ ) at relatively negative potentials; and virtually halogen-free surface at potentials approaching the negative limit. The pH dependence of iodine adsorption was relatively slight [64,66]. The Pt(111)  $(3\times 3)R30^\circ$  and Pt(111)  $(\sqrt{7}\times\sqrt{7})R19^\circ$  iodine adlattices were remarkably hydrophobic, while the Pt(111)  $(\sqrt{3}\times\sqrt{3})R30^\circ$  iodine adlattice was distinctly hydrophilic [66].

The reductive desorption of  $I_{(ad)}$  to aqueous  $I^-$  in the hydrogen evolution region :



has been discussed in many papers [64,66,71]. The packing density, adlattice structural changes, and the difference in free energies between  $I_{(ad)}$  and  $I_{(ad)}^-$  ( $-150 \text{ kJ mol}^{-1}$  for polycrystalline Pt and  $-140 \text{ kJ mol}^{-1}$  for Pt(111) [64]) have been determined.

Direct *in-situ* measurements (i.e. in the presence of an electrolyte) have been made on the Pt(111)  $(3\times 3)R30^\circ$ , Pt(111)  $(\sqrt{3}\times\sqrt{3})R30^\circ$  and Pt(111)  $(\sqrt{7}\times\sqrt{7})R19^\circ$  I-adlattices by SHG [72], XAS [65], and STM [73-75]. The STM work confirms hexagonal close packed structures for the  $(3\times 3)R30^\circ$  and the  $(\sqrt{7}\times\sqrt{7})R19^\circ$  I-adlattices but there is an additional assymmetric  $(3\times 3)$  structure formed together with the hexagonal  $(3\times 3)$ . A recent letter [76] has given the image of the Pt(100)  $(\sqrt{2}\times\sqrt{2})R45^\circ$  I-adlattice by STM. LEED studies [77] of

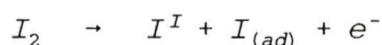
$I_{2(g)}$  adsorption at a stepped surface,  $Pt_{(s)} [6(111) \times (111)]$ , gave no indication of selective adsorption at steps. The iodine monolayer at stepped surfaces is still based on a hexagonal close packed layer, so that the structure of this layer is relatively independent of the Pt surface atom orientation. Therefore, a similar packing arrangement of the I-adlattice structure is expected to be present on a smooth polycrystalline electrode (as in the present work), though with less order present.

Now we consider oxidation reactions of iodine and iodide on platinum surfaces. The morphology of current-potential curves of iodine oxidation obtained when Pt(100), Pt(111), and polycrystalline Pt electrodes were treated with saturated aqueous iodine solution were similar, and consisted of a single peak at 1.32 V vs RHE. However, the ordered adsorbed I-adlattices on Pt(100) and Pt(111), prepared in UHV and then immersed in 1M aqueous  $HClO_4$ , when oxidised to  $IO_3^-$  exhibited different current-potential curves [63,78], hence different kinetic parameters.

Moreover, iodine tends to form thick films on the surface of an electrode. The formation of iodine films on the surface of a rotating disk platinum electrode during the oxidation of the iodide in acid and neutral solutions has been observed [79,81]. The rate of the reaction has been found to depend on the rate of transfer of  $I^-$  to the electrode and the rate of removal of  $I_2$  and  $I_3^-$  from the electrode surface.

Thickness of the iodine films was from hundreds to thousands of Angstroms.

Returning to the reaction studied here, there are few other studies on the mechanism of oxidation of  $I_{(ad)}^-$  to  $IO_3^-$  [59,82,83]. The rate determining step of  $I_2$  oxidation to  $IO_3^-$  on polycrystalline Pt in acetic acid was suggested [82] :



Moreover, the coulometry of the oxidation reaction of  $I_{(ad)}$  to  $IO_3^-$  was studied as noted at the beginning of this section, but no kinetic parameters were elucidated from the experimental data.

The kinetics of the iodine oxidation reaction is thoroughly analysed in this work using the a.c. voltammetry impedance method. Actually, this work is the first study probing the iodine oxidation reaction using the a.c. voltammetry impedance method, in which the electrode potential has a sinusoidal perturbation on top of a slower sweep at a rate of  $10 \text{ mV s}^{-1}$ . This method measures the variation of the impedance (i.e. the resistance to the flow of a.c. current through the cell) as the electrode potential is swept through the potential region of interest where the electrochemical reaction is occurring. From the impedance data and analysis of Bode plots the configuration of the circuit which models the

electrochemical reaction (the so-called equivalent circuit) may be determined. The variation of the faradaic impedance (due to the reaction on the surface of the electrode) and double-layer capacitance (due to charge separation at the interface) with electrode potential can also be examined. A reaction mechanism for the iodine oxidation reaction, involving an iodo-oxide complex, is proposed and compared with experimental results in Chapter 5.

## CHAPTER TWO

## Experimental Setup and Instrumentation

2.1) Introduction:

The hardware used to run the experiments presented in chapters four and five is described in this chapter. The electrochemical cell was used to study the hydrogen sorption reaction and iodine oxidation reaction on polycrystalline platinum. Both of these studies share nearly the same instrumentation. The specifications of each instrument is discussed briefly.

2.2) The electrochemical cell:

The cell was made of pyrex without ground glass joints as these proved to be a source of contamination. The ground glass joints were replaced by standard thermometer ports equipped with teflon o-rings for airtight sealing. The cell was enclosed in a Faraday box to minimise electromagnetic noise.

The working electrode (WE) and counter electrode (CE) were smooth polycrystalline platinum wires (0.5 mm diameter and approximately 2 cm in length). These were spot welded to tinned copper wires, and sealed in a tube of soft glass (5 mm inner diameter, approximately 10 cm in length). The platinum

wire that was fitted inside the relative hydrogen electrode (RHE) was sheathed in thin shrinkable teflon rather than glass.

All glassware was cleaned in saturated chromic acid solution at 65°C and rinsed with ultra-high-purity (UHP) water. The UHP water was delivered by a MILLIPORE MILLI-Q water system, equipped with four cartridges:

- 1) Charcoal filter.
- 2) Two ion-exchange columns.
- 3) Organic filter.
- 4) Residue filter.

The cell was filled with either sulfuric acid,  $\text{H}_2\text{SO}_4$  (BDH Analar) or perchloric acid  $\text{HClO}_4$  (BDH Analar) solutions ( $0.1 \text{ mol dm}^{-3}$ ) made up in UHP water. Dissolved oxygen was removed from the acid solution by sparging with Ar (Linde, UN1006) for 20 to 30 minutes.

The working electrode and the acid solution were tested for cleanliness by sweeping the potential, for one cycle, up to 1.6 V through the oxide region and then holding the potential in the double-layer region, at 0.5 V, for twenty minutes (these regions are indicated in (fig. 1.1 or 4.6)). The area characterising the hydrogen peaks was measured. The potential was then swept in the hydrogen region, to check whether the integral area under the peaks had changed (the conditions were considered acceptable if the area had not decreased by more than 10%). Purity was further checked by

sweeping up to the oxide region for one cycle, and then doing multiple cycles (more than 80 cycles) in the hydrogen region to examine peak distortion. The solution was considered clean if fifty cycles led to no peak distortion.

2.3) The technique used to study the hydrogen sorption reaction is the Sweep-Step technique. The instruments which run the electrochemical cell in this technique are :

1 ) The function generator (FG); type HB-111, HOKTO DENKO Ltd.

Setting accuracy of output potential is 1%

Setting accuracy of sweep rate (10 to 200 mV s<sup>-1</sup>) is 1%

2 ) The step generator (SG); Locally made (Chemistry Electronics shop).

3 ) The potentiostat; type MINISTAT E-401, THOMPSON

ELECTROCHEMISTRY

Maximum output current      1 A ±5%

Output Voltage                    ±40V ±10%

Setting Resolution                0.016%

Maximum External Control    ±10 V

Input

Response Rate                    ±0.1 to 10 V μs<sup>-1</sup>

(depends on the cell characteristics)

Phase Lag (negligible beyond 50 kHz for perturbation

signals 20 mV peak to peak from a 2V source for a

resistive dummy cell with 1 kΩ between WE and RE; 4.7 kΩ between CE and RE)

## 4 ) Digital oscilloscope type NICOLET NIC-310

Stores 4000 data points per sample down to 1  $\mu$ s time per point.

Analog Bandwidth	30 MHz
Rise Time	11 ns
Input Impedance	1 M $\Omega$
A/D resolution	12 bits

The whole instrumental setup is shown schematically in figure 2.1.

2.4) The technique used to study the iodine oxidation reaction is A.C. Voltammetry; this technique measures the A.C. Impedance (ACI) of the interface as the potential is swept :

The instruments which run the electrochemical cell in this experiment are :

- 1 ) Function Generator (FG); (See above).
- 2 ) Potentiostat; (See above).
- 3 ) Lock-in-amplifier (LIA); type SR530 STANFORD RESEARCH SYSTEMS

Signal Channel :

	Voltage	Current
Input Impedance	100 M $\Omega$	1 k $\Omega$
Full Scale	100 nV to 500 mV	
Sensitivity		100 fA to 0.5 $\mu$ A
Noise	7 nV/ $\sqrt{\text{Hz}}$ at 1 kHz	0.13 pA/ $\sqrt{\text{Hz}}$ at 1 kHz
Gain accuracy	1% (2 Hz to 100 kHz)	

Reference channel :

Frequency	0.5 Hz to 100 kHz
Input Impedance	1 M $\Omega$
Phase Control	90° shift, fine shifts in 0.025° steps
Time Constants	1 ms to 100 s (6 db/octave)

The overall experimental setup is shown in figure 2.2.

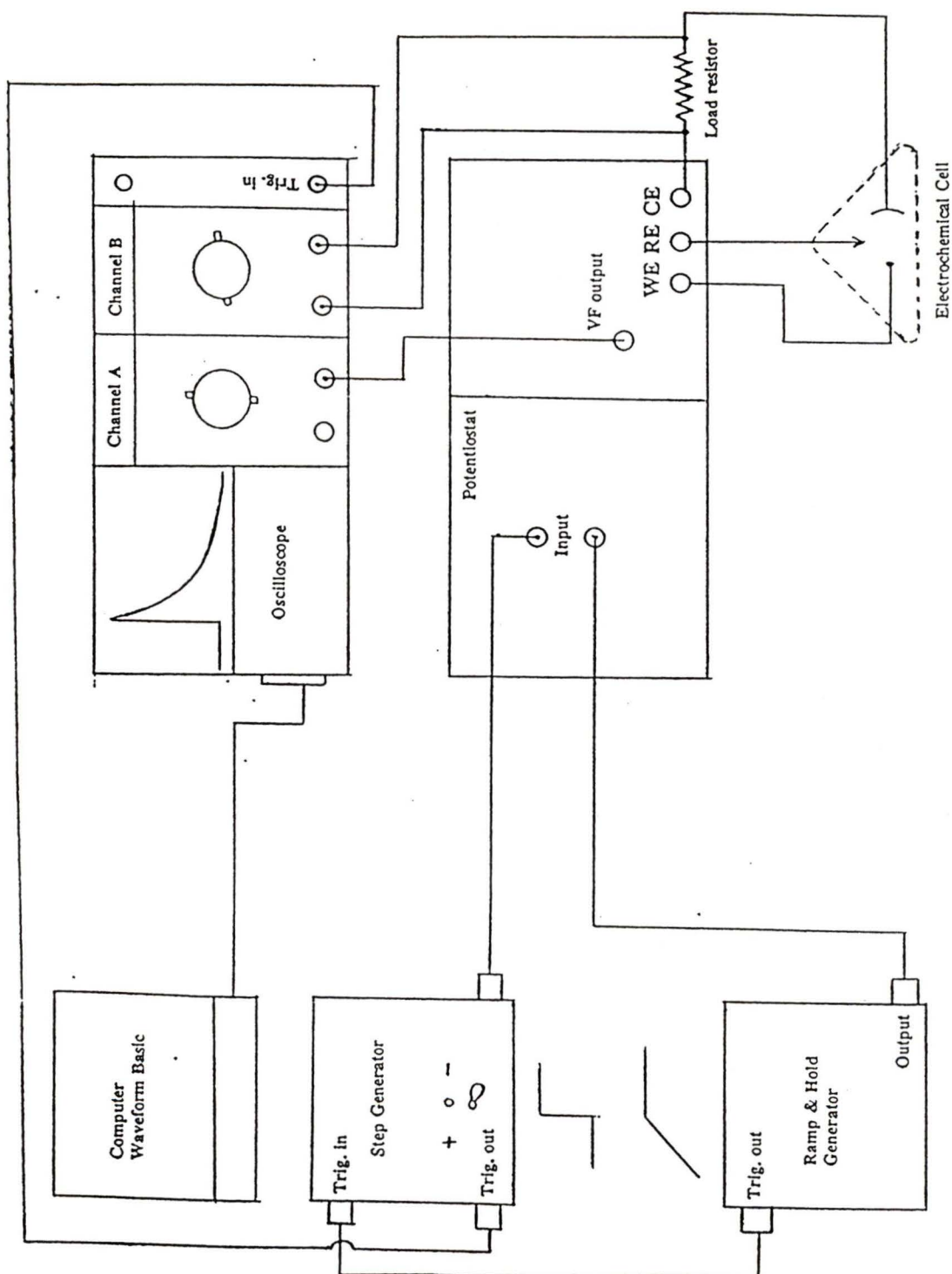


Figure 2.1 Schematic of the instrumental setup used to study the hydrogen sorption reaction on the platinum surface.

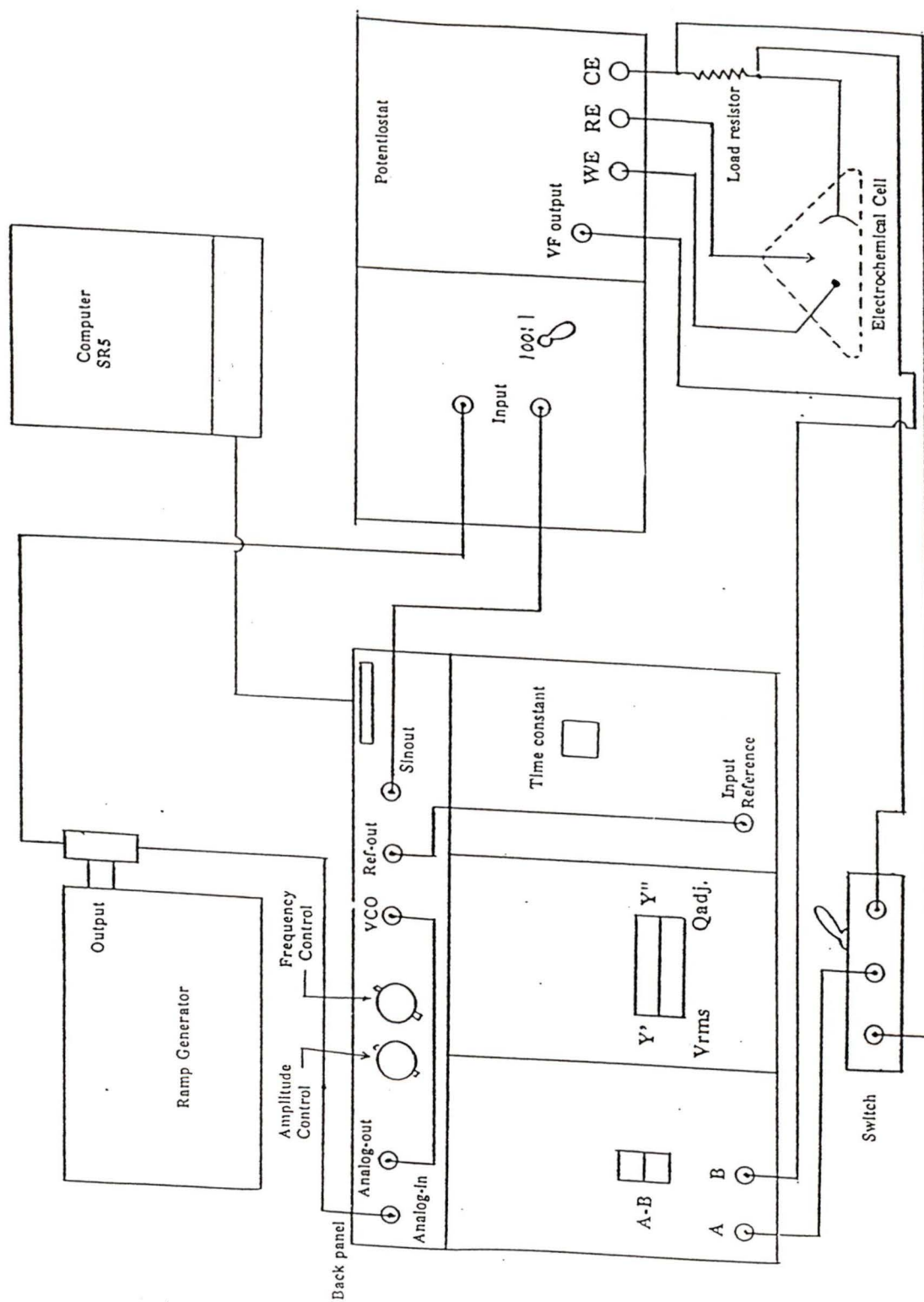


Figure 2.2 Schematic of the instrumental setup used to study the iodine oxidation reaction on the platinum surface.

## CHAPTER THREE

## Potentiostatic Circuit Analysis

3.1) Introduction:

In chapter four of this thesis, the kinetics of the hydrogen sorption reaction are studied. This reaction is quite fast and consequently the instrumentation employed should have a fast response. The instrument which is usually used to study electrochemical reactions is the potentiostat, and it is implemented using operational amplifier (op-amp) circuits. Before describing what a potentiostat does, let us discuss the response operation of an op-amp circuit. The response of an op-amp circuit, with an inverting configuration (fig 3.1), to an applied signal  $V_i$  is always to set  $e^+ = e^-$  in the shortest possible time. In this case, the negative feedback established through the feedback loop acts to force  $e^-$  to virtual ground at point S because  $e^+$  is grounded. For an ideal op-amp this would happen instantaneously. An ideal op-amp is characterised by infinite gain, infinite input impedance, and infinite bandwidth. Additionally, it should have zero response time, zero output when  $e^+ - e^- = 0$ , and zero output impedance, i.e., the amplifier can supply as much current as is necessary to drive the load.

From first principles,

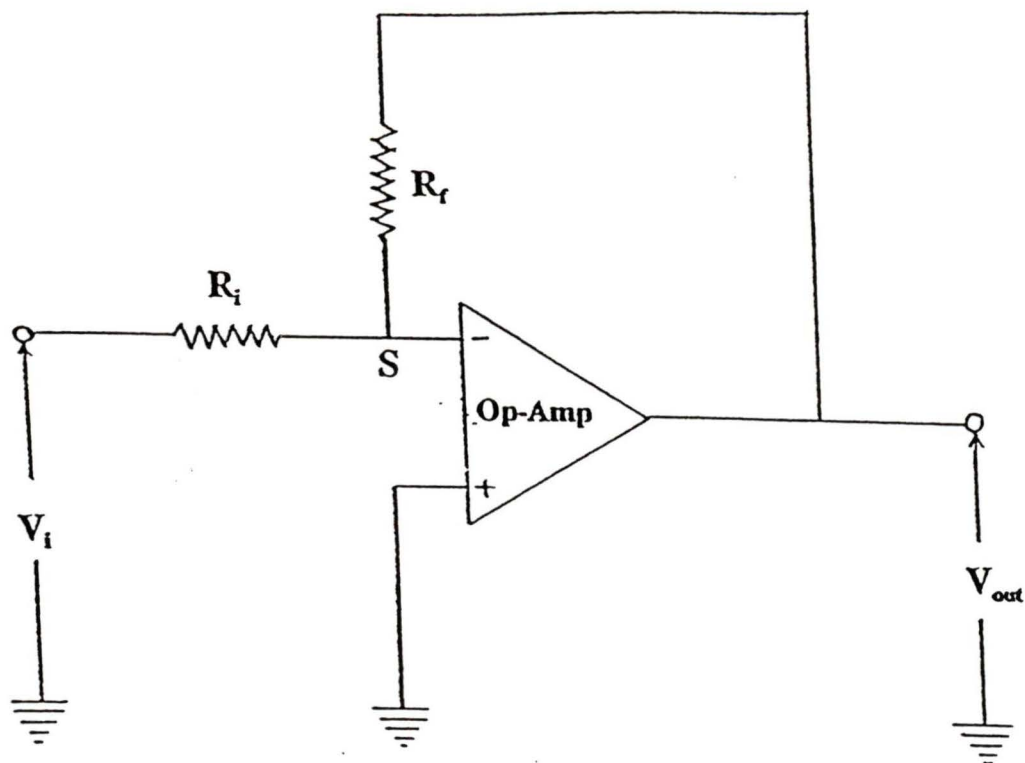


Figure 3.1 Basic op-amp circuit, inverting configuration, with negative feedback.

$$V_{out} = -\frac{R_f}{R_i} V_i \quad (3.1)$$

and therefore the ratio  $R_f/R_i$  controls the magnitude of the amplified signal.

If this op-amp circuit is connected to an electrochemical cell, (fig 3.2), it acts as a control amplifier (CA) and the same theory applies:

$$V_{out} = -V_i \quad \text{for} \quad R_i = R_f$$

The arrow represents the tip of the luggin probe (LP) of the reference electrode (RE). The LP detects the potential close to the surface of the working electrode (WE). Since the

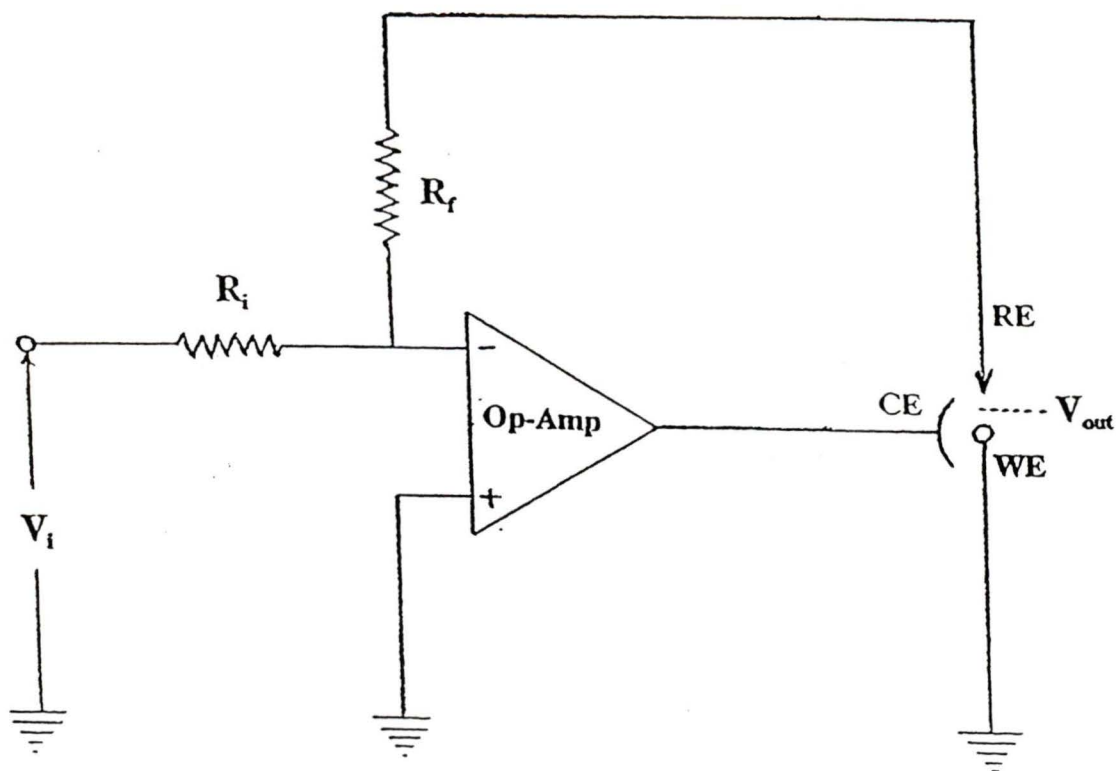


Figure 3.2 Schematic of the circuit for a single op-amp potentiostat. CA, control amplifier; CE, counter electrode; RE, reference electrode; WE, working electrode.  $V_{out}$  is the potential at the tip of the LP.

WE is grounded then the potential between it and a point in the solution near the surface of the WE is:

$$E_{WE} - E_{RE} = 0 - (-V_i) = +V_i$$

and hence the voltage signal that is applied at the input has been applied between the WE and the RE. The circuit in (fig 3.2) is an example of a single op-amp potentiostat. In principle, the potentiostat should be capable of performing two functions.

- 1) Maintaining the required potential at the surface of the WE

by delivering the necessary output current from its control amplifier (CA).

2) Ignoring any voltage changes that occur at the RE due to small electrochemical currents going through the RE. The potentiostat uses another op-amp called the Voltage follower(VF) to eliminate this problem. The Voltage Follower is placed in the feedback loop with its high impedance positive input connected to the RE. Therefore, a negligible fraction of the current flows through the RE because it now possesses a high impedance.

To illustrate, the output potential is established at the RE when the potentiostat drives a transient current from the counter electrode (CE) through the electrochemical cell to complete the feedback loop. Since the RE has a high impedance, virtually all the current from the CE passes through to the WE, and let us refer to this as the electrochemical current  $I_c$ . As a result, a potential drop occurs between the RE and WE, and the VF would output the potential established at the RE. Actually, the potentials at the LP and the surface of the platinum electrode of the RE are slightly different, but does not affect the analysis and will be assumed to be zero. However, there are many factors which determine the magnitude of the  $I_c$  along this path. These factors are either of electrochemical nature (like solution resistance or double-layer capacitance) or instrumental (e.g. particular design of the op-amp). To expand on this, an increase in the former

tends to reduce  $I_c$  and delays the build up of zero potential at point S (fig 3.2). Consequently the response of the circuit is slower. The instrumental factors are associated with the design capability of the op-amp in delivering the required current to the system in order to achieve the fastest response.

The response problem was analysed for a combined electrochemical potentiostatic (CEP) system. The CEP system was theoretically simulated using the circuit configuration shown in fig. 3.3. Note that the following notation will be used in this chapter, and the reader is referred to fig. 3.3 for physical definitions.

CA  $\equiv$  Control Amplifier

VF  $\equiv$  Voltage Follower

$e_s$   $\equiv$  Voltage at the input of control amplifier

$e_{op} - e_c$   $\equiv$  Voltage drop across the current measuring resistor ( $R_1$ )

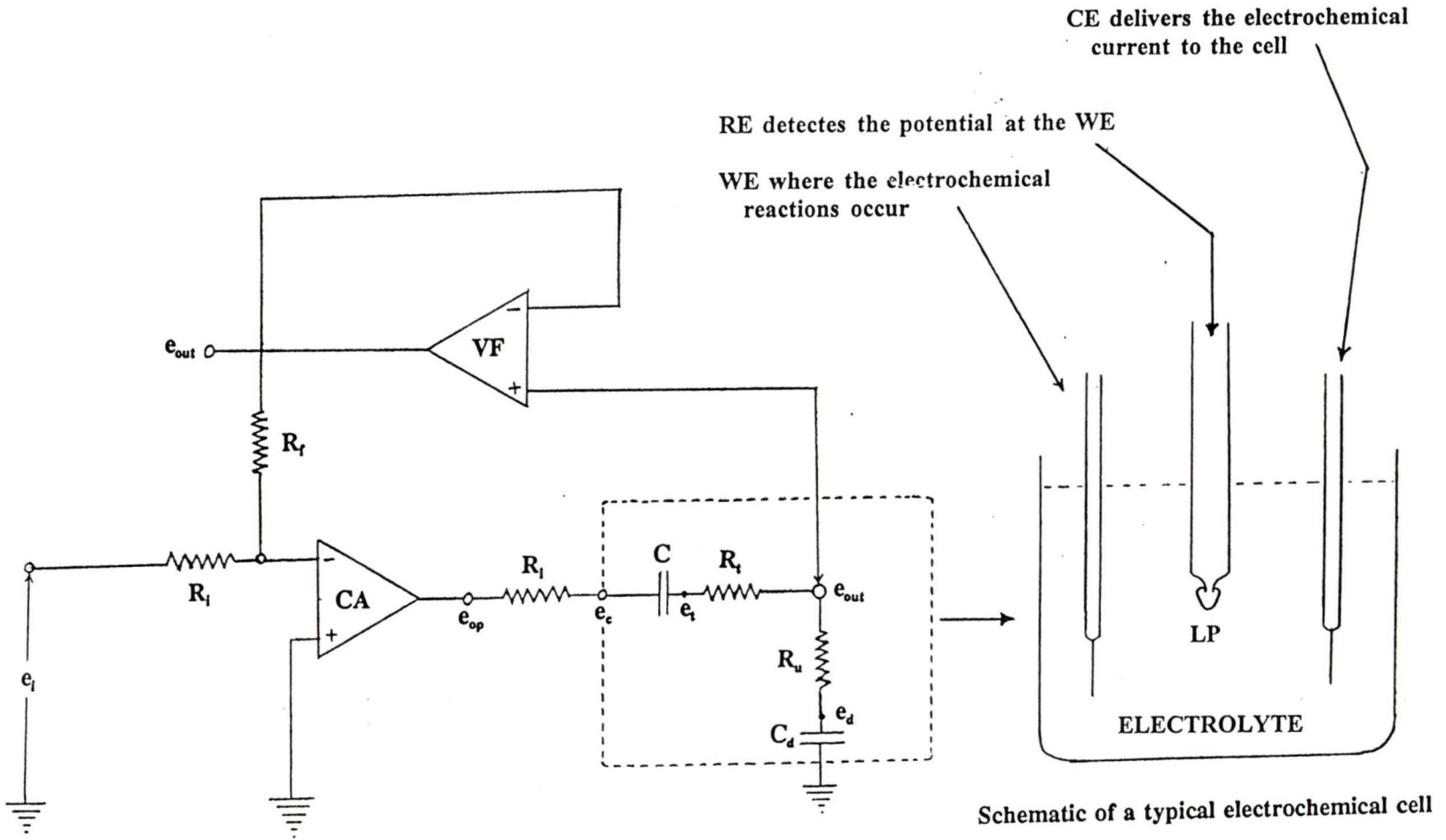
$e_c - e_t$   $\equiv$  Voltage drop due to the double layer capacitance at the counter electrode (CE).

$e_t - e_{out}$   $\equiv$  Voltage drop due to solution resistance ( $R_t$ ) between the CE and the Luggin Probe (LP) of the reference electrode (RE).

$e_{out} - e_d$   $\equiv$  Voltage drop due to the uncompensated resistance ( $R_u$ ) between the LP and the working electrode (WE).

C &  $C_d$  are the double layer capacitances at the surfaces of

Figure 3.3 Circuit of the combined electrochemical cell and potentiostat (CEP). The dotted box encloses the dummy cell which is a circuit representation of the real cell.



the CE and WE respectively.

$e_i$  is the input voltage applied from a step generator , and  $e_{out}$  is the output voltage occurring at the tip of the LP.

The potentiostat is the circuit network associated with the CA and VF, while the electrochemical cell is represented by the network of capacitors and resistors enclosed in the dotted box.

The purpose of this analysis is to improve the response of the CEP system so that the required potential can be established at the surface of the WE long before the hydrogen sorption reaction (or any other fast faradaic process) occurs. These fast faradaic processes necessitate designing a potentiostat and an electrochemical cell of optimum performance in order to achieve the best response time of an output signal  $e_{out}$  relative to an input signal  $e_i$ .

In this theoretical treatment a potential step of one volt, which we refer to as a unit step function  $u(t)$ , is applied at  $e_i$  and the response of the CEP system is studied in both the frequency and the time domain.

In the time domain, the transient response of the CEP system will be studied by applying a unit step function signal at the input of the CEP system, and monitoring the output signal obtained between the RE and WE. If the CEP system is driven by an ideal CA op-amp, then the output signal should have the same form as the input unit step signal (fig. 3.4). However the CEP system is a real system, and the signal

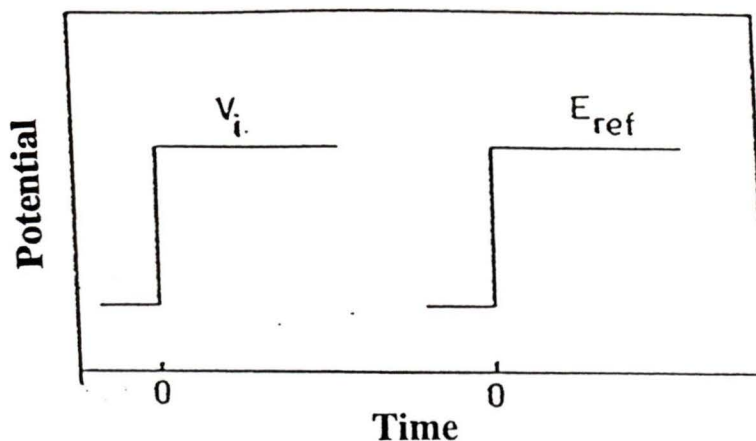


Figure 3.4 Schematic of the potentiostatic response function to a step input signal of voltage ( $V_i$ ) for a perfect electrochemical system. ( $E_{ref} \equiv$  potential at the RE). Input on left, output on right.

obtained between the RE and WE in response to a perfect step input function normally has the form similar to that shown in fig. 3.5. Thus the potential has a finite rise time followed

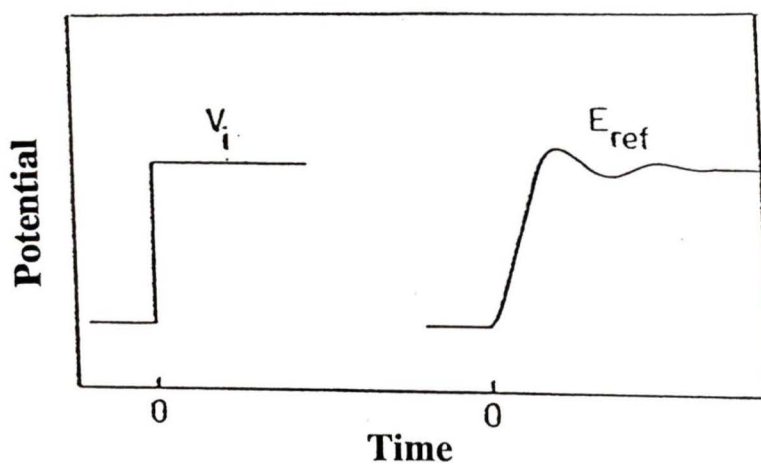


Figure 3.5 Schematic of the potentiostatic response function to a step input signal of voltage ( $V_i$ ) for a real electrochemical system. Input on left, output on right.

by damped oscillation about the steady state value. It is only after these oscillations have decayed to zero that the system is strictly under potentiostatic control. The interval during which these events occur is called the lower time limit [a9]. This lower time limit is not only a function of the characteristics of the CA, but also depends upon external parameters such as load resistance, and cell impedance (which is due to solution resistance and double-layer capacitances).

In the frequency domain,  $u(t)$  can be expressed as an integral of a linear combination of single-frequency components where the frequency is considered to be continuous over an infinite range. Each frequency component is associated with a complex number which describes the magnitude and the phase of the component. If the CEP system is using an ideal op-amp the magnitude and the phase of all the frequency components will not change and the output will look the same as the input (fig. 3.4). As already stated, the CEP system is a real system, and consequently acts to reduce the magnitude and introduces phase shifts to the high frequency components of  $u(t)$ . As a result, the output signal has the form shown in (fig. 3.5). The objective of studying the frequency response characteristics of the CEP system, as the instrumental and electrochemical parameters are varied, is to predict the response of the CEP system to an applied transient signal (e.g.  $u(t)$ ).

In this simulation, there are seven circuit parameters

characterising the CEP system. The response, in the time and frequency domain, was analysed by considering one standard set of parameters. In every calculation, six of these parameters are kept fixed, while the value of one of them is changed.

Finally, there is no point in studying the transient response of the CEP system if the latter is not stable. Stability means that the output does not become infinite but converges to a steady state value. In this analysis, we have confirmed the stability of the CEP system, before studying the response characteristics.

### 3.2) Theory:

This section is divided into four sections. In the first, the transfer function (TF) of the CEP system will be defined and derived. The TF will then be used to derive the values of the system stability and response in subsequent sections. In the second section, the relationship between the system stability and the TF will be discussed. The third section will discuss the response of the CEP system in the frequency domain in order to examine the change in the CEP system's bandwidth when varying the instrumental and electrochemical parameters.

Finally, the fourth section will discuss the response of the CEP system in the time domain in order to determine how fast the output signal is established at the LP of the RE, and the corresponding output currents needed. Again the transient response is studied as a function of the instrumental and

electrochemical parameters. In all cases a simple RC series circuit (fig 3.6) will be used to illustrate the concepts, before studying the more complex CEP system.

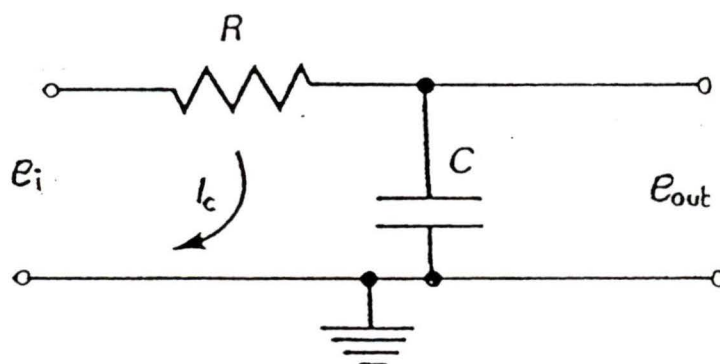


Figure 3.6 The RC circuit.

### 3.2.1) Transfer Function:

#### Definition:

Any system is characterised by a unique property called the Transfer Function of the system. A transfer function (TF) is defined as the ratio of the Laplace transformed output signal to the Laplace transformed input signal, where the output and input signals are real variables in the time domain and should be Laplace transformed to the complex s-domain. We can transform a function  $f(t)$  in the time domain to the complex s-domain by applying Laplace transforms:

$$\overline{f(s)} = \int_0^{\infty} f(t) \cdot \exp(-st) dt \quad (3.2)$$

where  $f(t) = 0$  when  $t < 0$  for any physical system, and  $s$  may be written as:

$$s = \sigma + i \omega$$

$\sigma \equiv$  is a real number (greater than zero for system stability)

$i \equiv$  is the square root of  $-1$

$\omega \equiv$  is the angular frequency in  $\text{rad s}^{-1}$  representing the imaginary part of the complex  $s$ -variable.

As a shorthand we can write the Laplace integral as:

$$\overline{f(s)} = \mathcal{L}\{f(t)\} \quad \text{and} \quad f(t) = \mathcal{L}^{-1}\{\overline{f(s)}\} \quad (3.3)$$

where,  $\mathcal{L}$  and  $\mathcal{L}^{-1}$  indicates the Laplace and inverse Laplace transform operators.

In this calculation, for simplicity the argument  $s$  will often be omitted, and the bar used to denote a transformed quantity. Hence, the TF is:

$$G(s) = \frac{\mathcal{L}\{e_{out}\}}{\mathcal{L}\{e_i\}} = \frac{\overline{e_{out}}}{\overline{e_i}} \quad (3.4)$$

The TF can be defined at any point in a linear circuit, which is a network of resistors, inductors and capacitors, by taking  $e_{out}$  at the chosen point in the circuit ( $e_{out}$  should not be confused with the  $e_{out}$  term of the CEP system, fig. 3.3). In the CEP system, the dummy cell is an example of a linear

circuit where its TF can be defined at each junction (e.g.  $e_{out}$ ,  $e_{op}$ ,  $e_t$  etc. junctions). To illustrate, the TF at the LP of the dummy cell in fig. 3.3 is simply  $e_{out}/e_i$ .

#### Derivation:

In order to derive the TF of the CEP system, current-voltage relations in the time domain are first determined for the various circuit parameters. Mathematically, these relations are linear differential equations which can be solved using Laplace transforms. Applying Laplace transforms to these differential equations transforms them to the complex s-domain. The new complex equations can be solved simultaneously to determine the TF at the various junctions. To illustrate, a good example is to derive the TF of a simple RC circuit.

#### Derivation of the TF of a simple RC circuit:

For a simple RC circuit (fig. 3.6), if any signal  $e_i$  is applied at the input a current  $I_c$  flows through the RC circuit, assuming no current flows through the voltmeter at  $e_{out}$ , causing a voltage drop across R and C respectively.

From first principles, the current through the resistor is,

$$I_R = \frac{e_i - e_{out}}{R} \quad (3.5)$$

and through the capacitor is ,

$$I_C = \frac{dq}{dt} = C \frac{d(e_{out} - 0)}{dt} \quad (3.6)$$

Equating eq. (3.5) to eq.(3.6) :

$$I_C = C \frac{de_{out}}{dt} = I_R = \frac{e_i - e_{out}}{R} \quad (3.7)$$

By rearranging, we get the differential equation:

$$\frac{de_{out}}{dt} + \frac{e_{out}}{RC} = \frac{e_i}{RC} \quad (3.8)$$

At this stage, we can apply Laplace transforms to solve the differential equation and determine the TF of the RC circuit in the s-domain. In general, if  $y(t)$  is the output of a system and  $y(0) = 0$  at  $t=0$ , (appendix I.1), then:

$$\mathcal{L}\left\{\frac{dy(t)}{dt}\right\} = s \mathcal{L}\{y(t)\} \quad (3.9)$$

Applying Laplace transformation to eq.(3.8) we get:

$$\mathcal{L}\left\{\frac{de_{out}}{dt}\right\} = \mathcal{L}\left\{\frac{e_i - e_{out}}{R C}\right\} \quad (3.10)$$

$$\Rightarrow s \mathcal{L}\{e_{out}\} = \mathcal{L}\left\{\frac{e_i - e_{out}}{R C}\right\} \quad (3.11)$$

$$\Rightarrow s \overline{e_{out}} = \frac{\overline{e_i} - \overline{e_{out}}}{RC} \quad (3.12)$$

$$\therefore TF = \frac{\overline{e_{out}}}{\overline{e_i}} = \frac{1}{1+sRC} \quad (3.13)$$

Derivation of the TF of the CEP system:

We can utilize the same mathematical treatment, discussed in the previous section to find the TF of the CEP system. Applying an input signal  $e_i$  causes a current  $I_c$  to flow through  $R_1, C, R_t, R_u$  and  $C_d$  (fig. 3.3). This causes voltage drops across each component in the network such that:

$$I_c = \frac{e_{op} - e_c}{R_1} = C \frac{d(e_c - e_t)}{dt} = \frac{e_t - e_{out}}{R_t} \quad (3.14)$$

$$I_c = \frac{e_{out} - e_d}{R_u} = C_d \frac{de_d}{dt} \quad (3.15)$$

Another current  $I_R$  passes through  $R_i$  and  $R_f$  causing a voltage drop across these two resistors:

$$I_R = \frac{e_i - e_s}{R_i} = \frac{e_s - e_{out}}{R_f} \quad (3.16)$$

Again, we can use Laplace transforms to solve these differential equations and transform them to the complex  $s$ -domain:

$$\overline{I_c} = \frac{\overline{e_{op}} - \overline{e_c}}{R_1} = sC(\overline{e_c} - \overline{e_t}) \quad (3.17)$$

$$sC(\overline{e_c} - \overline{e_t}) = \frac{\overline{e_t} - \overline{e_{out}}}{R_t} \quad (3.18)$$

$$\frac{\overline{e_t} - \overline{e_{out}}}{R_t} = sC_d \overline{e_d} \quad (3.19)$$

$$sC_d \overline{e_d} = \frac{\overline{e_{out}} - \overline{e_d}}{R_u} \quad (3.20)$$

$$\overline{e_i} + \overline{e_{out}} = 2\overline{e_s} \quad (3.21)$$

The TF of the CA op-amp is given by the manufacturer in the s-domain. Since the  $e_s$  signal is established at its input while the  $e_{op}$  signal at its output then we can write:

$$\overline{e_{op}} = -\frac{g \overline{e_s}}{1 + \frac{s}{f_b}} \quad (3.22)$$

$$\text{where, } G(s) = \frac{g}{1 + \frac{s}{f_b}}$$

and  $G(s)$  (or  $G(i\omega)$ ) is the TF of the CA op-amp.

The negative sign refers to the negative output of the op-amp with the positive output being grounded. The parameter  $g$  is the d.c. gain of the CA op-amp. An op-amp is

characterised by another property and this is the break frequency ( $f_b$ ) indicated in fig. 3.8, section(3.2.3). This is assigned by the manufacturer to maintain the unity gain (i.e.  $V_{out}/V_i=1$ ) of the op-amp up to a certain frequency after which the gain starts to decrease quickly. This strategy prevents the op-amp from running into positive feedback, and hence instability. An op-amp could have one or more break frequencies and these are determined by extrapolation at the turning points on the gain characteristics (dotted line in fig. 3.8). The op-amp used in this treatment is assumed to have one break frequency somewhat similar to that of the RC circuit (fig. 3.8), and hence equation (3.22) which we have parameterised as an approximation of the real behaviour.

There are six equations with six unknowns all of which are expressed in Laplacian space. In order to get expressions for the TF's at each junction (i.e.  $e_{op}/e_i$  at  $e_{op}$ ,  $e_{out}/e_i$  at  $e_{out}$  etc.), these six equations should be solved simultaneously to obtain values of  $e_{op}, e_{out} \dots$  etc. in terms of  $e_i$  and then divide both sides by  $e_i$  to get the TF. Equations showing the transfer function at all junctions are presented in appendix I.2.

Also we can check on the validity of our expressions by defining the TF at junction  $e_{out}$  of the dummy cell as B such that:

$$B = \frac{e_{out}}{e_{op}} \quad (3.23)$$

and considering equations (3.21), (3.22) and (3.23), we can equate:

$$\overline{e_s} = \frac{\overline{e_i + e_{out}}}{2} = -\frac{\overline{e_{op}}}{G(s)} = -\frac{\overline{e_{out}}}{B G(s)} \quad (3.24)$$

and rearrange to get,

$$\frac{\overline{e_{out}}}{\overline{e_i}} = -\frac{B G(s)}{B G(s) + 2} \quad (3.25)$$

In order to define B in terms of R and C we simply solve simultaneously equations (3.17), (3.18), (3.19), and (3.20). Substituting for B and G produces the same expression of  $e_{out}/e_i$  as calculated before (appendix I.2).

In this analysis, the TF at the  $e_{out}$  junction (i.e. the LP of the RE) was used to determine the CEP system's stability, assign the bandwidth of response in the frequency domain, and characterise the transient voltage output signal at the LP in the time domain. On the other hand, the transfer functions at the  $e_{op}$  and  $e_c$  junctions were used to determine the output current delivered by the CA.

### 3.2.2) System Stability:

An essential condition when studying the response characteristics of circuit networks is to confirm the system stability for any applied input signal. To illustrate, feeding

any input signal  $V_i$  to a system of TF  $G$  would produce an output signal  $V_{out}$  equal to the product  $\mathcal{L}^{-1}\{G V_i\}$ . This is an example of a stable system, if  $G$  is always finite, because  $V_{out}$  is always assigned a predictable value and converges to a steady state. However, if  $V_{out}$  shoots out to any unpredictable value (e.g.  $\pm V_{supply}$ ) independent of the input signal and the TF, then the system is considered unstable. Circuit networks may be classified as stable or unstable depending on the nature of their TF and the parameters of their circuit components (e.g. Resistors, capacitors, d.c. gain...etc.). This is clarified following this derivation.

The stability of the CEP system is calculated by applying a standard procedure associated with the complex  $s$ -plane (fig. 3.7). This is simply done by referring to the TF's calculated

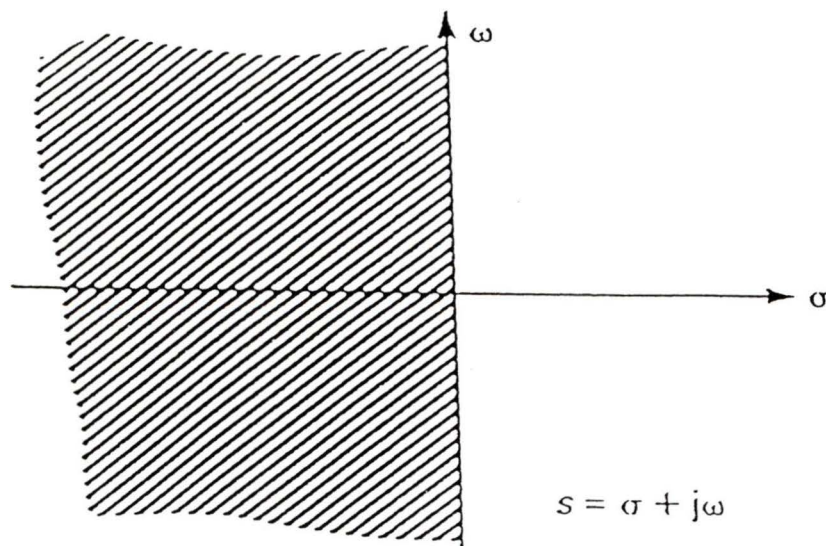


Figure 3.7 Complex  $s$ -plane. Poles of the TF must be in the shaded region for a stable system.

in section(3.2.1) and considering their denominator  $D$ , which is the same for all of them (See appendix I.2). Here, it is necessary to introduce a few terms before providing direct analysis on whether the CEP system is stable or not.

A stable system is one for which:

$$G(t) = \mathcal{L}^{-1}\{G(s)\} \rightarrow 0 \text{ as } t \rightarrow \infty \quad (3.26)$$

where  $G(s)$  is the TF in the frequency domain and  $G(t)$  is the corresponding time domain quantity. To clarify the idea of system stability a simple RC series circuit is discussed first.

#### Stability of the RC circuit:

The TF of the RC circuit in the  $s$ -domain (equation 3.13) can be expressed as:

$$G(s) = \frac{\frac{1}{RC}}{\frac{1}{RC} + s} \quad (3.27)$$

and this is a stable system because:

$$G(t) = \frac{1}{RC} \exp^{-\frac{t}{RC}} \rightarrow 0 \text{ as } t \rightarrow \infty \quad (3.28)$$

This means for a particular value of  $s$  (i.e.  $s = -1/RC$ ),  $G(s)$  goes to infinity and in this case  $s$  is called a pole of

$G(s)$ . To illustrate,  $G(s)$  will tend to infinity when the denominator tends to zero,

$$\begin{aligned} \text{if } G(s) &= \frac{1}{s-\sigma} \\ \text{then } G(t) &= \exp[\sigma t] \rightarrow 0 \text{ as } t \rightarrow \infty \\ &\text{only if } \sigma < 0 \end{aligned} \quad (3.29)$$

Therefore, a stable condition is achieved only when the poles of the TF lie in the LHS of the complex  $s$ -plane, (shaded area of fig. 3.7). Sometimes, poles of  $G(s)$  are complex conjugates in the  $s$ -plane. Only the real part  $\sigma$  needs to be considered as it determines whether the pole lies in the right hand side or the left hand side of the complex plane.

#### Stability of the CEP system:

The denominator  $D$  of the TF may be rearranged in the quadratic form:

$$D = as^2 + bs + c \quad (3.30)$$

which has the roots:

$$s', s'' = -\frac{b}{2a} \pm \frac{\sqrt{b^2 - 4ac}}{2a} \quad (3.31)$$

and these are the poles of the TF.

Consequently, the stability of this system may be considered in two cases:

1)  $b^2 > 4ac$ , the poles are real numbers, always negative and lying on the LHS of the complex s-plane because:

$$\left| \frac{b}{2a} \right| > \left| \frac{\sqrt{b^2 - 4ac}}{2a} \right|$$

where  $a, b$  and  $c$  are always real and positive (since the parameters of the circuit network are positive; see appendix I.2).

2)  $b^2 < 4ac$ , the poles are complex numbers, but only the real part  $\sigma$  need be considered which from eq.(3.31) and appendix I.2 is:

$$\sigma = -\frac{b}{2a} = -\left\{ \frac{f_b}{2} + \frac{\frac{2}{C} + \frac{2}{C_d} + R_u g}{4(R_u + R_t + R_l)} \right\} \quad (3.32)$$

Again the poles always have negative real parts and hence lie on the LHS of the complex s-plane. Therefore, the system never runs into instability at all given parameters of the circuit components. Now, we can step forward and study the gain and response characteristics of the system.

### 3.2.3) Frequency domain response analysis on the TF of the CEP system:

As already noted, the frequency response characteristics of the CEP system are a useful guide to predict the response performance of this system to general input signals. In a subsequent section, we will deal specifically with step input

signals. The TF is expressed as a function of the complex variable  $s$ , and it can be expressed as a function of frequency by choosing to work along the imaginary axis of the complex  $s$ -plane (fig 3.7). That is, replace  $s$  by  $i\omega$  and set  $\sigma$  equal to zero. The TF is a complex function of  $\omega$  characterised by its magnitude (the gain) and phase  $\phi$ . For a start, let us derive the gain and phase of a simple RC series circuit.

The gain and phase of a simple RC series circuit:

The TF of an RC series circuit can be expressed in terms of frequency  $\omega$  ( $\text{rad s}^{-1}$ ) by substituting  $i\omega$  for  $s$  in eq.(3.13) which gives:

$$\therefore TF = \frac{e_{out}}{e_i} = \frac{1}{1 + i\omega RC} \quad (3.33)$$

The magnitude of the TF is the Gain  $|G|$ :

$$|G| = \frac{1}{\sqrt{1 + (\omega RC)^2}} \quad (3.34)$$

and the phase is:

$$\phi = \arctan(\omega RC) \quad (3.35)$$

The change in  $|G|$  with  $\log(\omega)$  is illustrated schematically in fig. 3.8. Above a characteristic frequency the gain decreases rapidly, that is, the circuit acts like a low pass filter. The characteristic frequency is called the

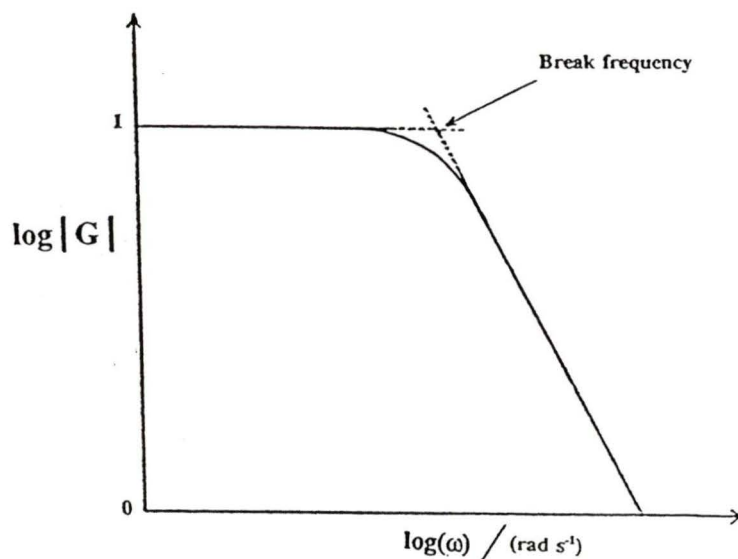


Figure 3.8 Bode plot of the frequency dependence of the gain of the RC circuit on (fig. 3.7).

break frequency of the RC circuit (indicated by an arrow). The change in  $\log|G|$  and  $\phi$  with  $\log(\omega)$  yield plots called Bode plots.

In the same way, the values of the gain and phase of the TF at the LP of the RE were determined for the CEP system. Please refer to appendix I.3.

An essential condition here is to maintain a very slow decrease in gain and minimum phase shift as the frequency of the input signal rises. A high gain and a minimum phase shift are essential criteria in designing a system characterised by a fast response time and a large bandwidth. The bandwidth is assigned as the frequency range covered when the gain drops to  $1/\sqrt{2}$  its original value. The standard set of parameters used

in this calculation is:

$$\begin{array}{ll} g = 10^5 & C_d = C = 30 \mu\text{F} \\ f_b = 62.8 \text{ rad s}^{-1} & R_u = 1 \Omega \\ R_1 = 10 \Omega & R_t = 5 \Omega \end{array}$$

These are chosen as typical values for our real system. Thirteen different sets of circuit parameters are shown in table 3.1 page 50.

#### 3.2.4) Time domain analysis on the response of the CEP system to a step signal:

In this analysis, the effect of the CA op-amp and the electrochemical cell parameters on the lower time limit were studied. That is, we examined the overall response of the CEP system through theoretical simulation of the physical system.

So, how can this physical system be simulated?

In a linear system the TF determines the form of the output signal for any given input signal. The difference in the profile of the output signal with respect to the profile of the input signal (e.g. fig. 3.5) is a direct consequence of the nature of the system characterised by its TF. To illustrate, if an input signal  $x(t)$  in the time domain is applied to a circuit of a TF  $G(s)$ , it should be Laplace transformed to the s-domain as  $x(s)$ . The output signal in the s-domain  $y(s)$  is simply represented by the product  $G(s) \cdot x(s)$ . The output signal in the time domain is calculated by finding the inverse Laplace transform of  $y(s)$ , and a flow diagram for

this mathematical analysis is shown schematically in fig. 3.9.

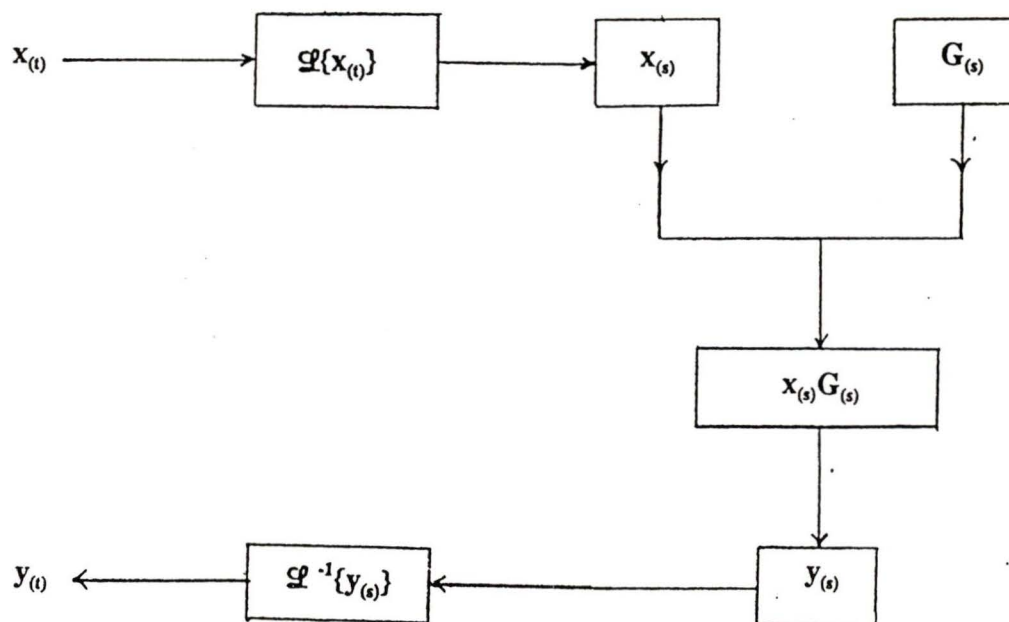


Figure 3.9 Flow diagram showing the sequence of steps in the transform analysis of an electrical circuit.

As we have done in the previous sections, the TF of a simple RC series circuit is used to explain how the response of the CEP system was simulated. Applying a unit step signal,  $u(t) = 1$  for  $t > 0$ , the Laplace transform of  $u(t)$  and hence the resultant output signal in the s-domain are:

$$x(s) = \frac{1}{s}$$

$$y(s) = \frac{1}{s(1+sRC)}$$
(3.36)

Solving  $y(s)$  by partial fractions and then applying inverse Laplace transform to  $y(s)$ , the resultant output signal in the time domain  $y(t)$  is obtained as:

$$y(t) = 1 - \exp\left(-\frac{t}{RC}\right) \quad (3.37)$$

It clearly appears that  $y(t)$  possesses a steady state component equal to one, and a transient component which is affected by the time constant  $RC$ . For example, if  $RC$  is high it will take a longer time to achieve a steady state, and the reverse is also true.

#### Simulating the experiment:

An input signal of a unit step function in the time domain which has a magnitude of +1 volt was used in this simulation. The method of calculation is the same as discussed in the previous section. The response characteristics of the voltage step detected at the LP of the RE is obtained by multiplying the corresponding TF (eq. 4, appendix I.2) with  $1/s$  to produce an output signal in the frequency domain,  $y(s)$ :

$$y(s) = \frac{1}{s} \frac{-gCf_b(C_dR_u s + 1)}{D} \quad (3.38)$$

The inverse Laplace transform of  $y(s)$  yields the required output in the time domain  $y(t)$ , and the complicated output formula is presented in appendix I.4. It should be noted that

the voltage step is negative which agrees with the theory stated earlier in section 3.1.

Similarly, we can repeat this process to find the values of the output signals at the  $e_{op}$  and  $e_c$  junctions. The difference of these two signals represents the voltage drop across  $R_1$  and is therefore proportional to the current. The formula for the output signal in the time domain is presented in appendix I.5.

### 3.3) Results, Discussion and conclusions:

The simulated results characterising the response of the CEP system in the frequency and the time domain are presented and discussed in separate sections.

#### 3.3.1) Bode plots:

The characteristics of the gain and phase, of the TF at the LP of the RE, for thirteen different circuit parameters are shown in figures 3.10 to 3.17. The corresponding bandwidths determined from these plots are tabulated in Table 3.1. From the Bode plots the following observations were drawn that are directly related to the CEP system response performance:

The bandwidth got wider when the following were made higher:

- 1) The d.c. gain ( $g$ ), (fig. 3.10).
- 2) The break frequency ( $f_b$ ), (fig. 3.11).

- 3) The solution resistance between the RE and WE (referred to as the uncompensated resistance  $R_u$ ) (fig. 3.12).
- 4) The double-layer capacitance at the CE (C) (fig. 3.13).

The bandwidth got narrower when the following were made higher:

- 1) The solution resistance between the CE and RE ( $R_t$ ) (fig. 3.14).
- 2) The double-layer capacitance at the WE ( $C_d$ ) (fig. 3.15).
- 3) The load resistance ( $R_l$ ) (fig. 3.16).

Table 3.1 and figures 3.10-3.16 will follow on in the next consecutive pages. An example is given at the bottom of table 3.1 to illustrate how to use the table. In figures 3.10-3.16 plots of gain and phase against angular frequency for a particular parameter are presented on the same page. Later, the voltage and the current response plots will be presented on the same page.

Table 3.1 :

Bode parameters, output current and response time of the CEP system				
Circuit Components	Values of circuit components	Bandwidth of GAIN/ $10^5$ ( $\text{rad s}^{-1}$ )	Maximum Output Current (A)	Response Time ( $\mu\text{s}$ )
Double-Layer Capacitance at WE	1.0 $\mu\text{F}$	7.06	0.30	3.18
	15.0 $\mu\text{F}$	2.56	0.68	8.60
	30.0 $\mu\text{F}$	2.27	0.77	10.4
Uncompensated Resistance	0.5 $\Omega$	1.59	0.44	6.80
	1.0 $\Omega$	2.27	0.77	10.4
	2.0 $\Omega$	3.83	1.18	13.2
Solution Resistance	0.5 $\Omega$	3.02	0.81	7.50
	2.0 $\Omega$	2.70	0.79	8.40
	5.0 $\Omega$	2.27	0.77	10.4
Double-Layer Capacitance at CE	10.0 $\mu\text{F}$	2.22	0.76	10.5
	30.0 $\mu\text{F}$	2.27	0.77	10.4
Break Freq. of Op-amp ( $\text{rad s}^{-1}$ )	62.8	2.27	0.77	10.4
	628.0	20.0	0.94	1.36
	4000	>100	0.98	0.21
Current (Load) measuring resistance	5.0 $\Omega$	3.13	0.80	7.70
	10.0 $\Omega$	2.27	0.77	10.4
	20.0 $\Omega$	1.52	0.70	14.5
D.C. Gain of Op-amp	$10^5$	2.27	0.77	10.4
	$10^6$	20.0	0.93	1.43
	$10^7$	>100	0.98	0.14

For example, for the standard set of parameters shown on page 45, three different values of  $R_u$  (i.e. 0.5, 1 and 2  $\Omega$ ) produced bandwidths of  $1.59 \times 10^5$ ,  $2.27 \times 10^5$  and  $3.83 \times 10^5$   $\text{rad s}^{-1}$  respectively.

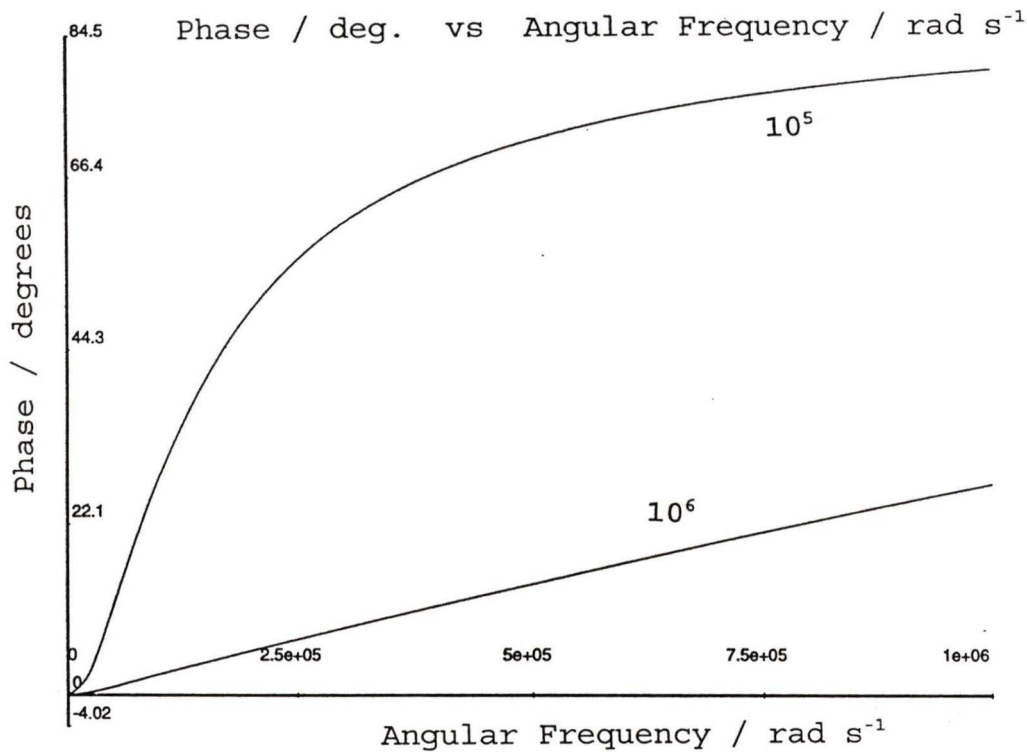
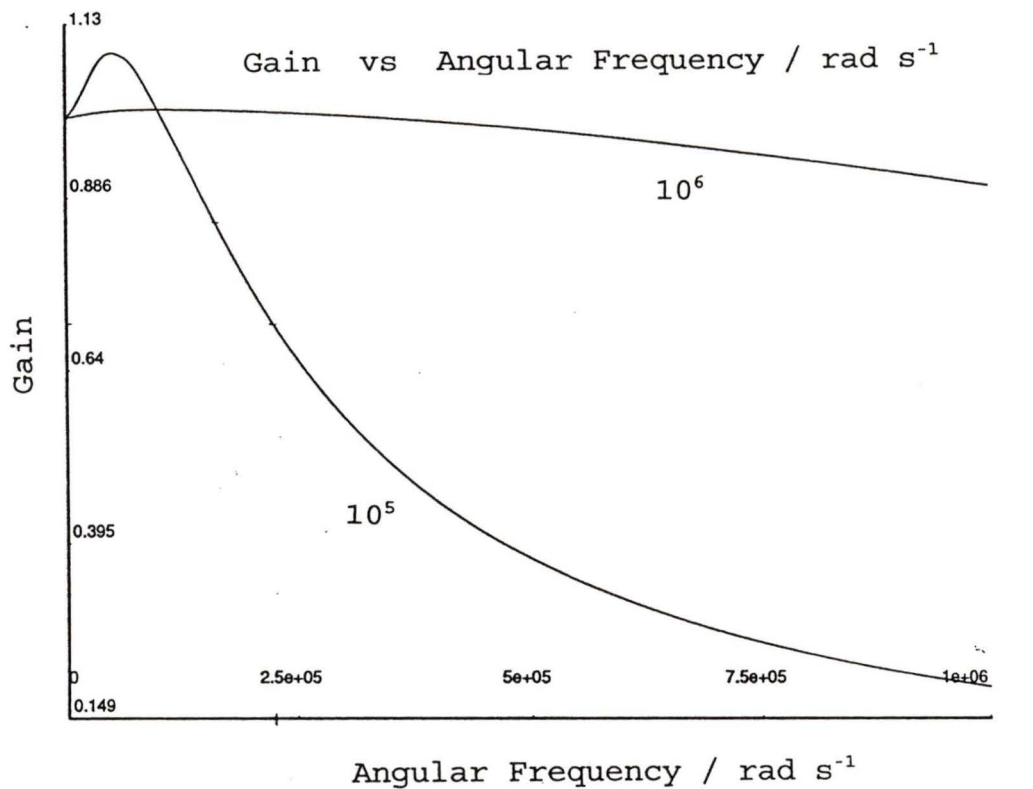


Figure 3.10 Frequency dispersion of the transfer function at the RE. Variation with the d.c. gain of the op-amp. Graphs of (a) gain and (b) phase(deg.) vs angular frequency ( $\text{rad s}^{-1}$ ).

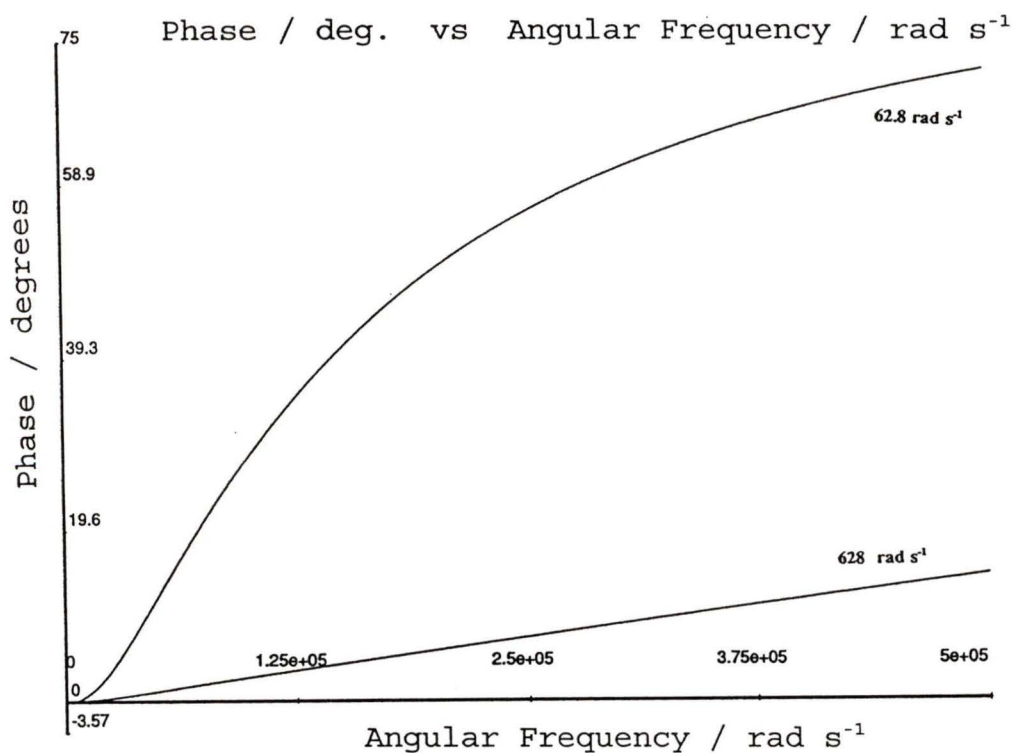
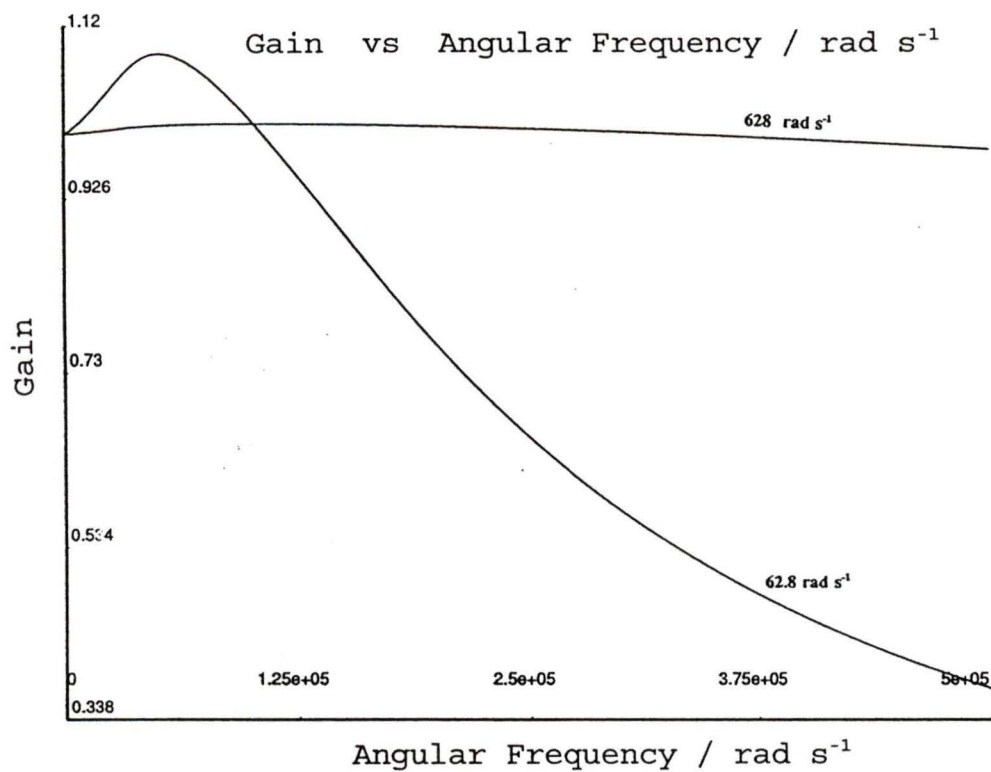


Figure 3.11 Frequency dispersion of the transfer function at the RE. Variation with the break freq. of the op-amp. Graphs of (a) gain and (b) phase(deg.) vs angular frequency ( $\text{rad s}^{-1}$ ).

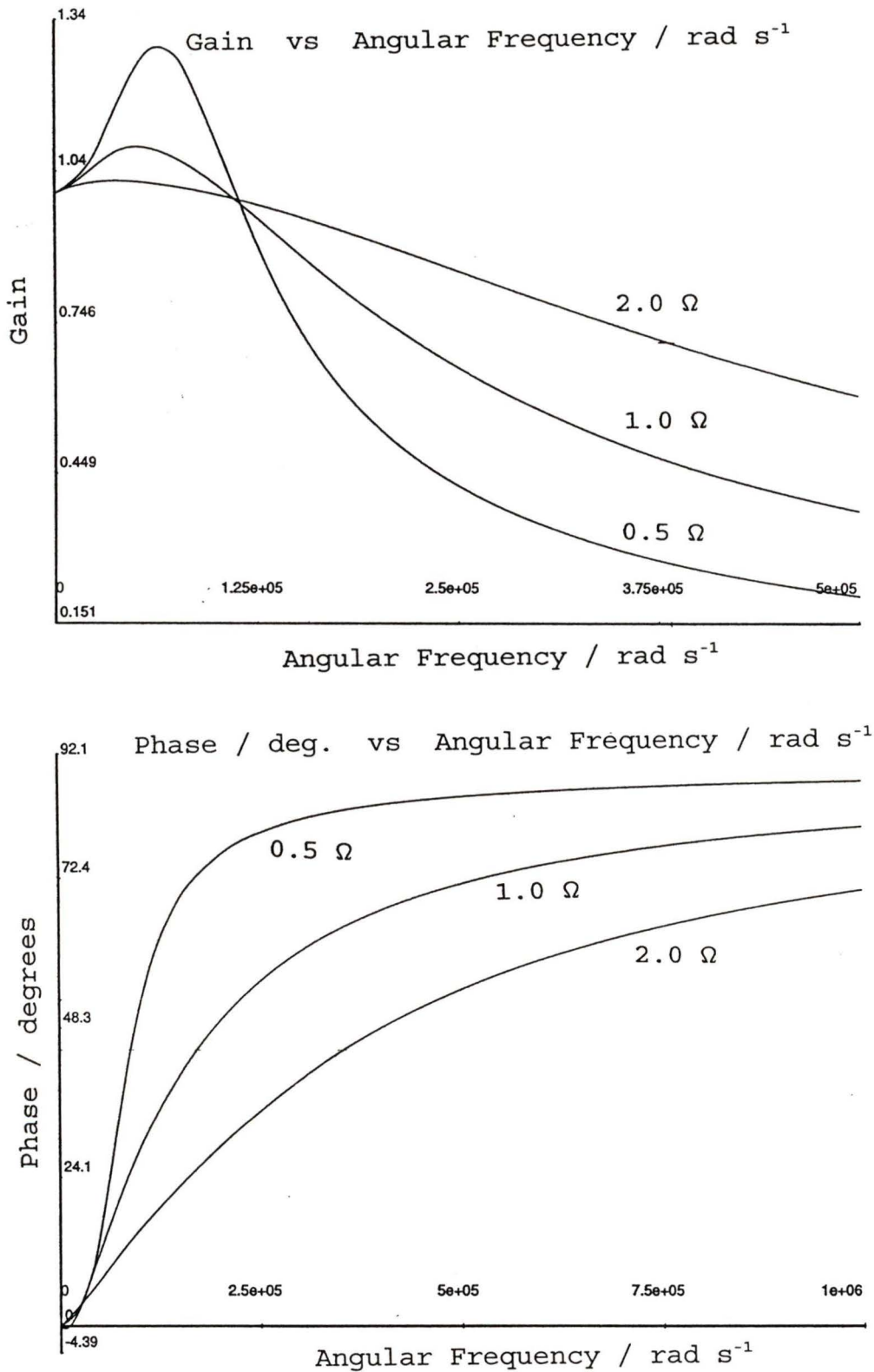


Figure 3.12 Frequency dispersion of the transfer function at the RE. Variation with the uncompensated resistance. Graphs of (a) gain and (b) phase (deg.) vs angular frequency ( $\text{rad s}^{-1}$ ).

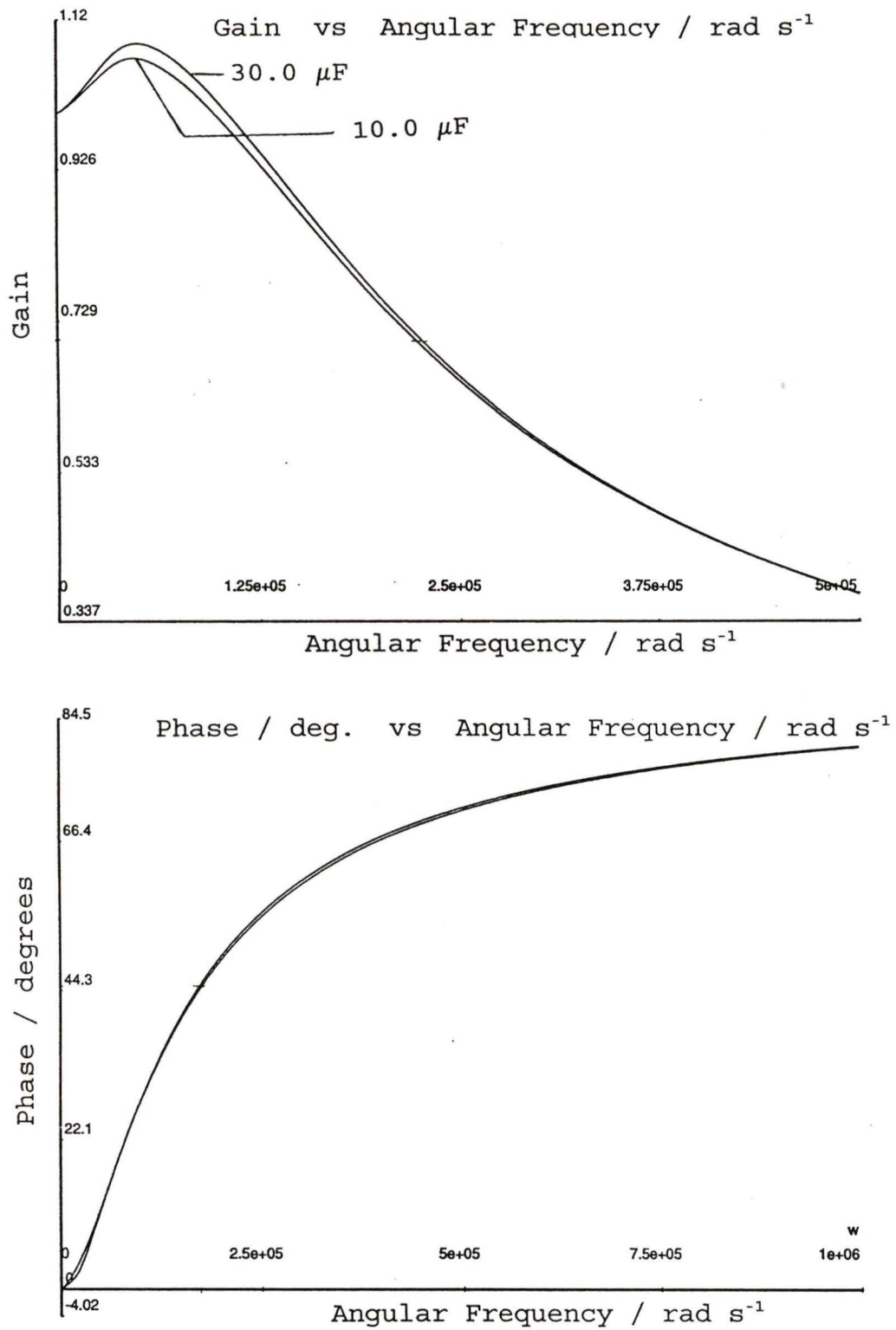


Figure 3.13 Frequency dispersion of the transfer function at the RE. Variation with the double-layer capacitance at the CE. Graphs of (a) gain and (b) phase (deg.) vs angular frequency ( $\text{rad s}^{-1}$ ).

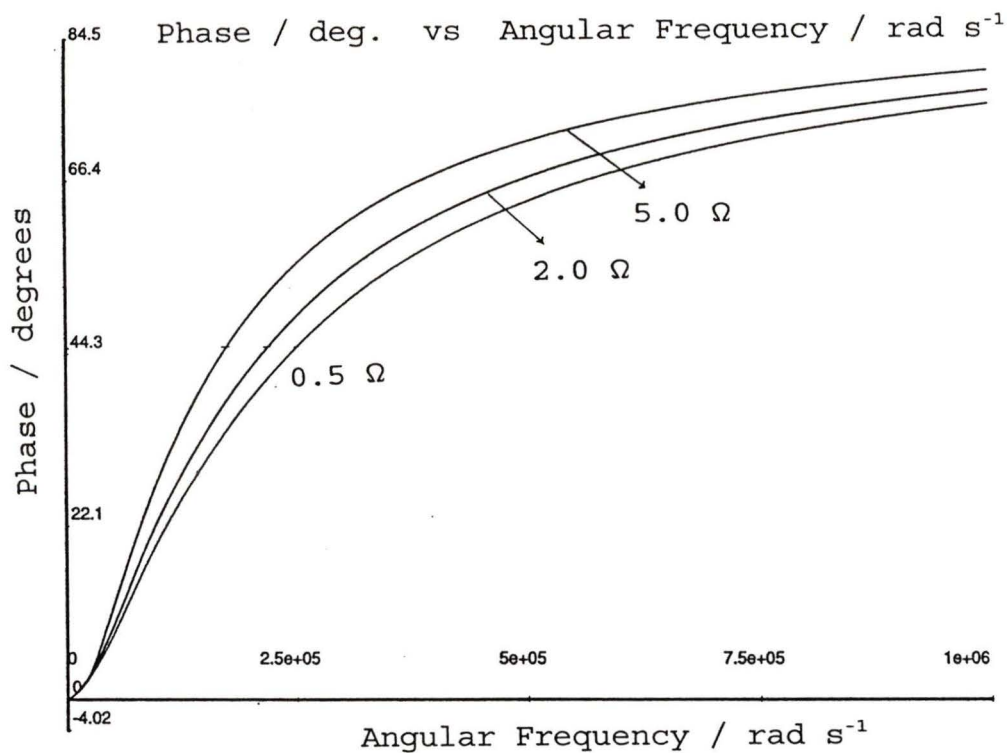
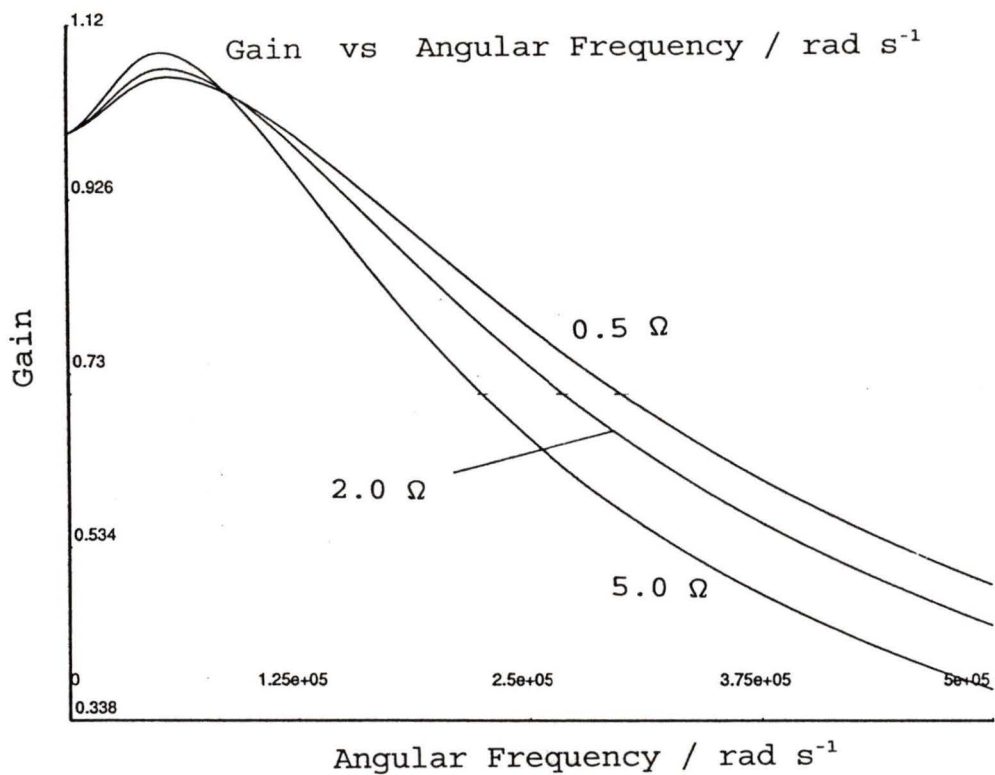


Figure 3.14 Frequency dispersion of the transfer function at the RE. Variation with the solution resistance. Graphs of (a) gain and (b) phase (deg.) vs angular frequency ( $\text{rad s}^{-1}$ ).

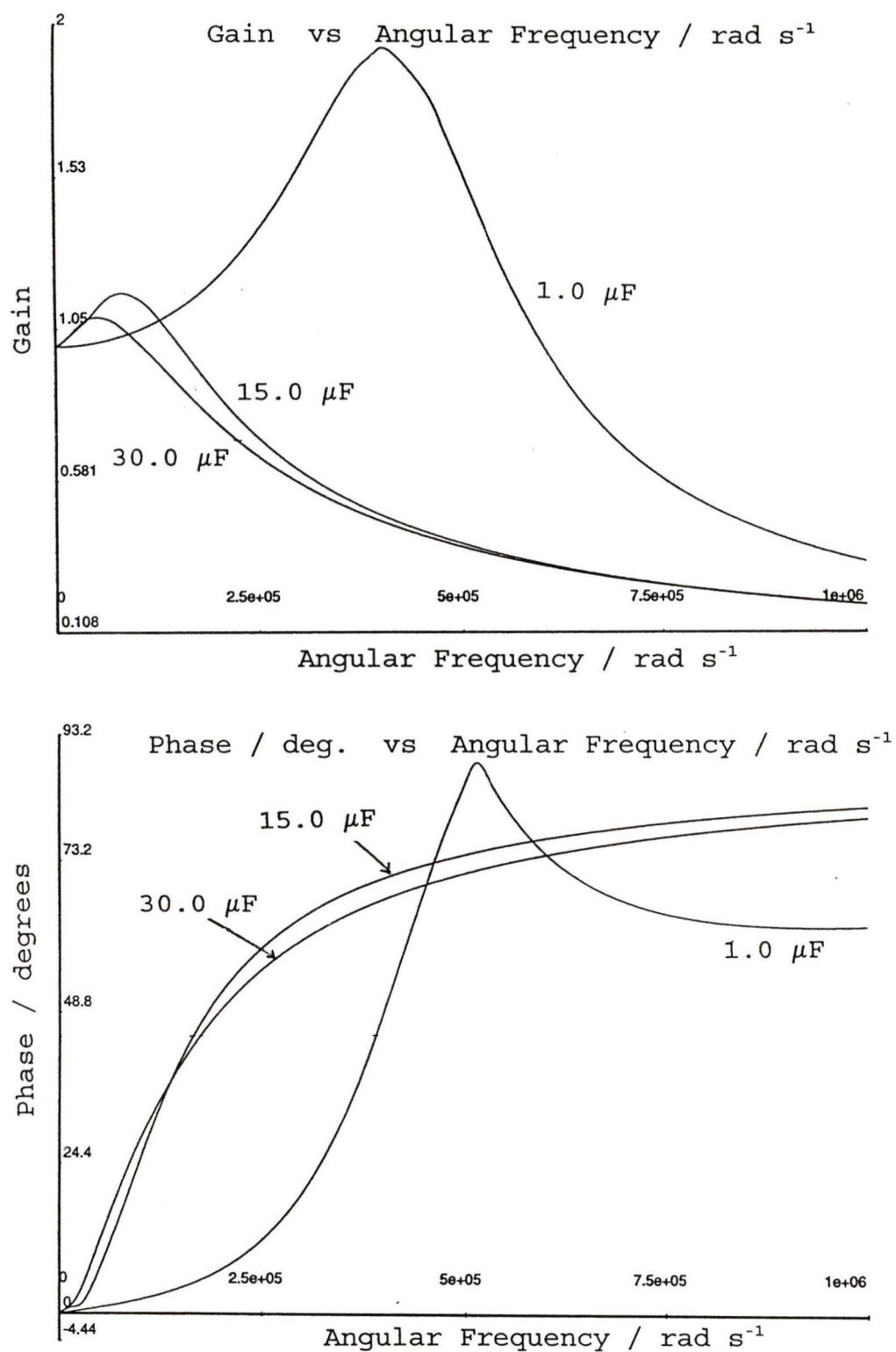


Figure 3.15 Frequency dispersion of the transfer function at the RE. Variation with the double-layer capacitance at the WE. Graphs of (a) gain and (b) phase (deg.) vs angular frequency ( $\text{rad s}^{-1}$ )

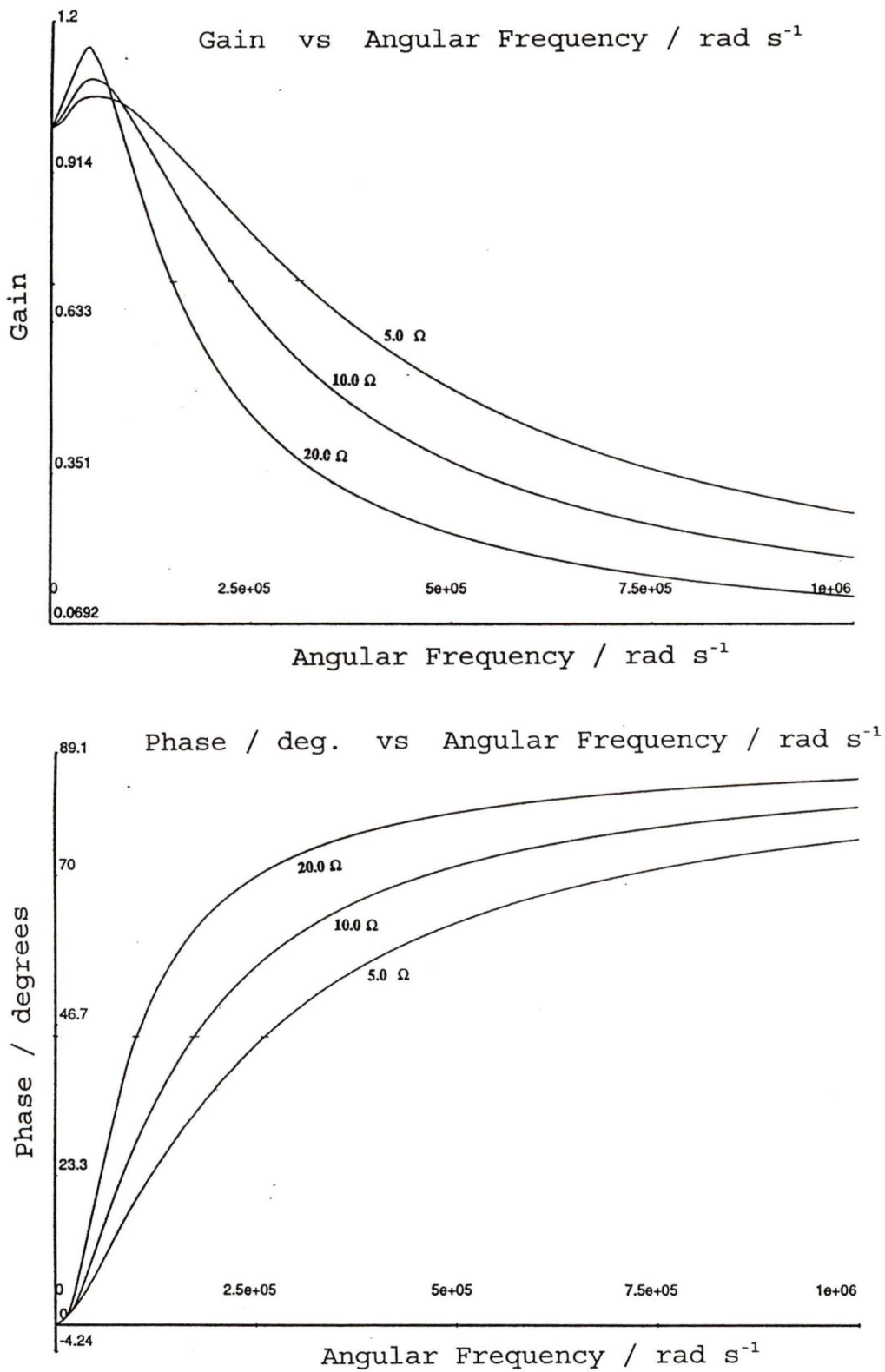


Figure 3.16 Frequency dispersion of the transfer function at the RE. Variation with the load resistance. Graphs of (a) gain and (b) phase (deg.) vs angular frequency ( $\text{rad s}^{-1}$ ).

From the above observations the following measures should be taken to improve the bandwidth of the system under study:

- 1) The control amplifier should possess a high d.c. gain and break frequency to enlarge the bandwidth.
- 2) The LP should be placed away from the WE to increase the uncompensated resistance and close to the CE to lower the solution resistance  $R_t$ .
- 3) The surface area of the WE should be reduced to lower the double-layer capacitance, which is proportional to the surface area. It is better to keep the surface area of the CE large because the effect of the double-layer capacitance at the CE on the gain and phase is negligible anyway. Large surface area at the CE allows higher transient current flow and better response.

### 3.3.2) Voltage and current responses due to an input step signal:

In the CEP system, there is essentially one general trend observed for all combinations of circuit parameters. The wider the bandwidth the faster is the response. Since a step function represents a large number of sinusoidal signals of low to high frequencies, by extending the bandwidth of the gain to higher frequencies we can have a steeper waveform earlier along the time axis. The response is defined as the time to achieve 90 to 95 % of the required voltage, preferably with the minimum level of oscillation. This nearly corresponds

to the time when a maximum current is driven into the circuit before it decays down to zero.

The response time and the maximum current output of the control amplifier obtained from the voltage and current response plots, figures 3.17 to 3.23, are tabulated beside the corresponding gain and phase characteristics in table 3.1. The results are in agreement with the observations of section 3.3.1; The overall response of the CEP system became faster when the following were made higher:

- 1) The d.c. gain ( $g$ ), (fig. 3.17).
- 2) The break frequency ( $f_b$ ), (fig. 3.18).
- 3) The solution resistance between the RE and WE referred to as the uncompensated resistance ( $R_u$ ) (fig. 3.19).

The response became slower when the following were made higher:

- 1) The solution resistance between the CE and RE ( $R_t$ ) (fig. 3.21).
- 2) The double-layer capacitance at the WE ( $C_d$ ) (fig. 3.22).
- 3) The load resistance ( $R_l$ ) (fig. 3.23).

The double-layer capacitance at the CE ( $C$ ) (fig. 3.20) showed a minor effect.

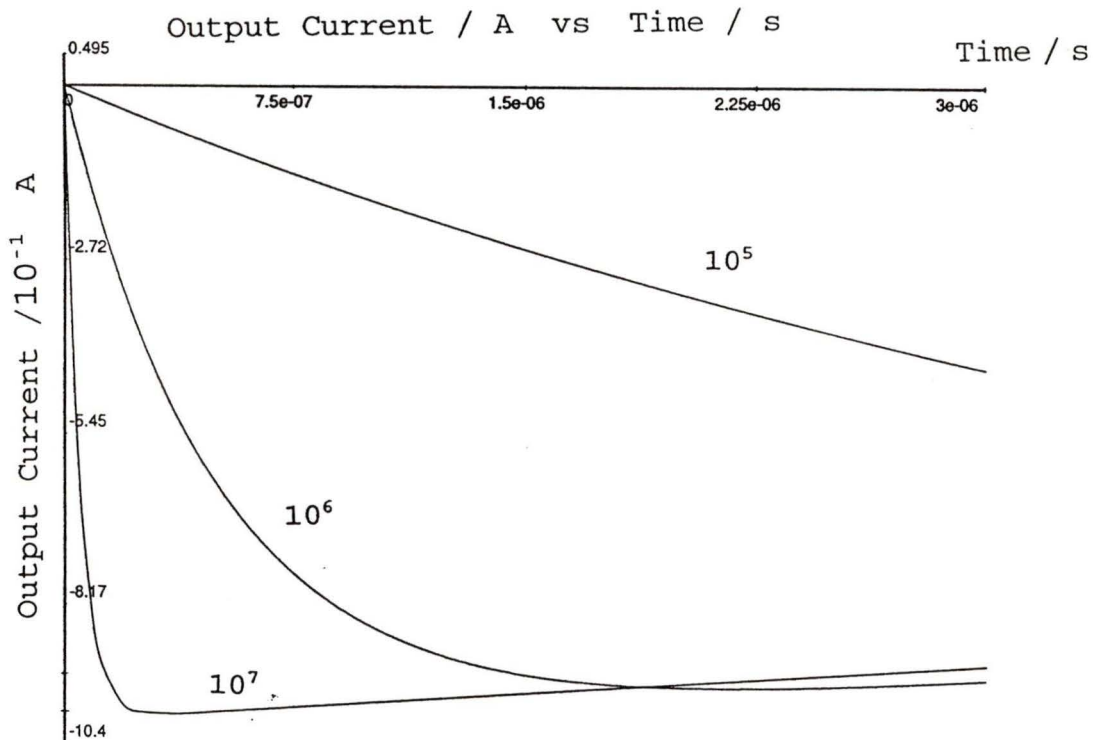
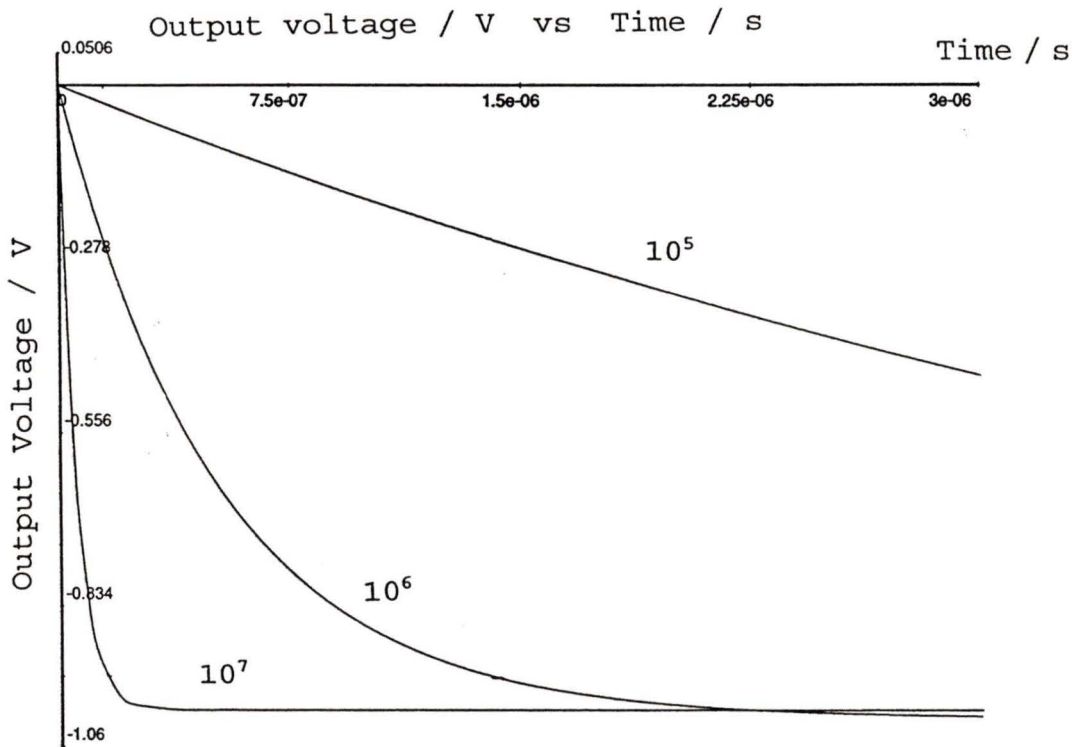


Figure 3.17 Response plots of the (a) voltage output at the RE / V, and (b) current output of the CA / A. Variation with the d.c. gain of the op-amp.

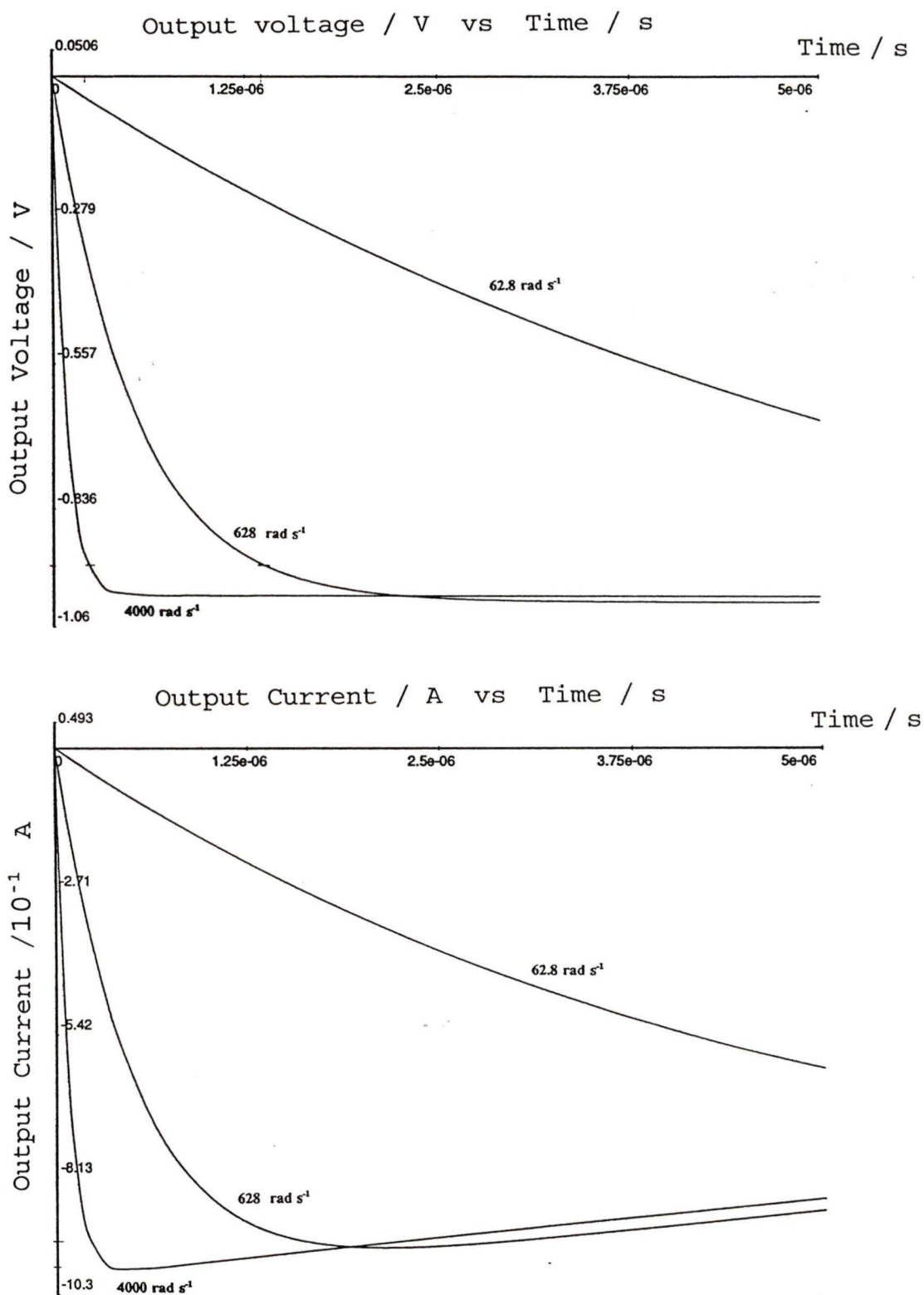


Figure 3.18 Response plots of the (a) voltage output at the RE / V, and (b) current output of the CA / A. Variation with the break frequency of the op-amp.

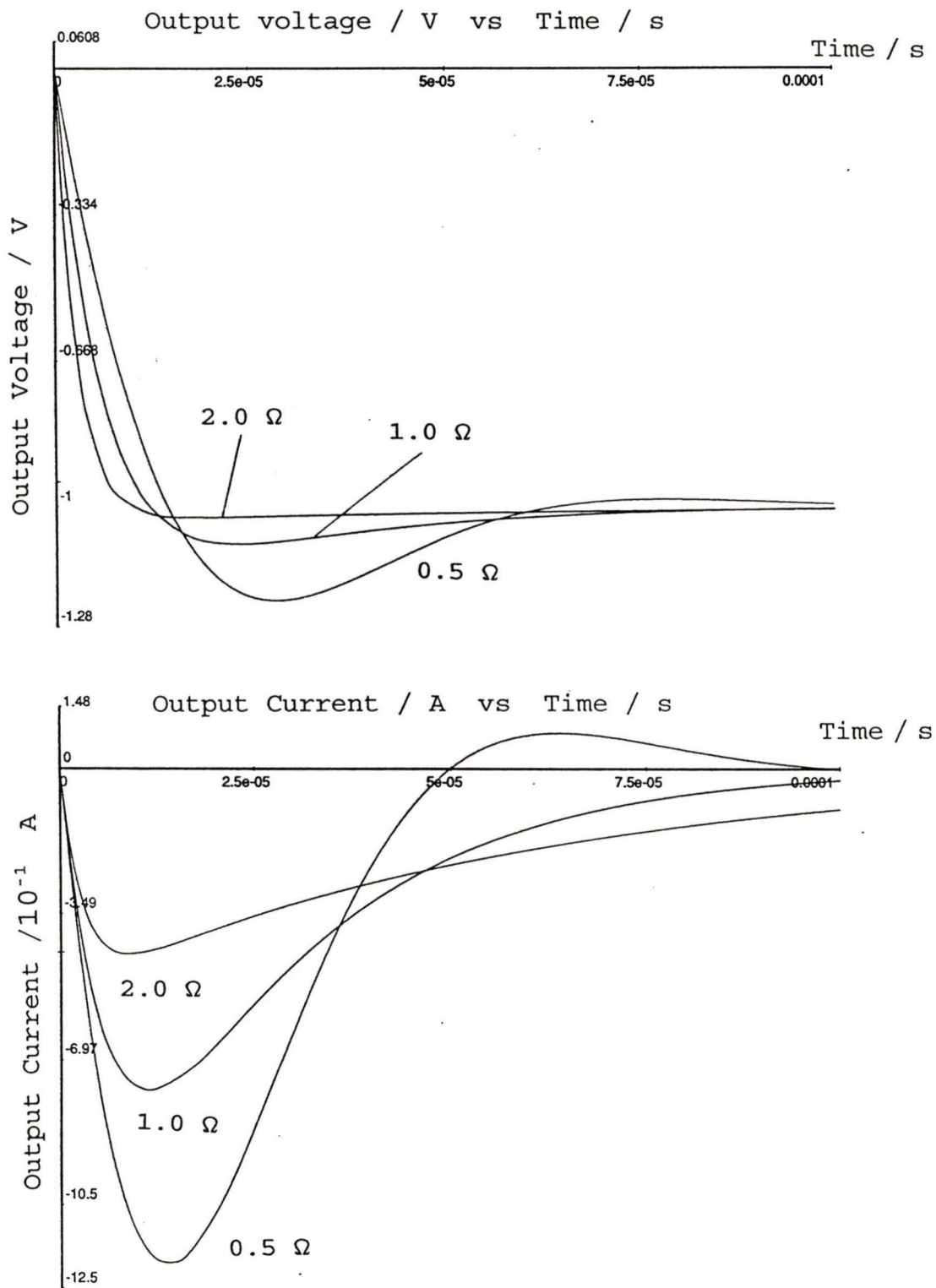


Figure 3.19 Response plots of the (a) voltage output at the RE / V, and (b) current output of the CA / A. Variation with the uncompensated resistance.

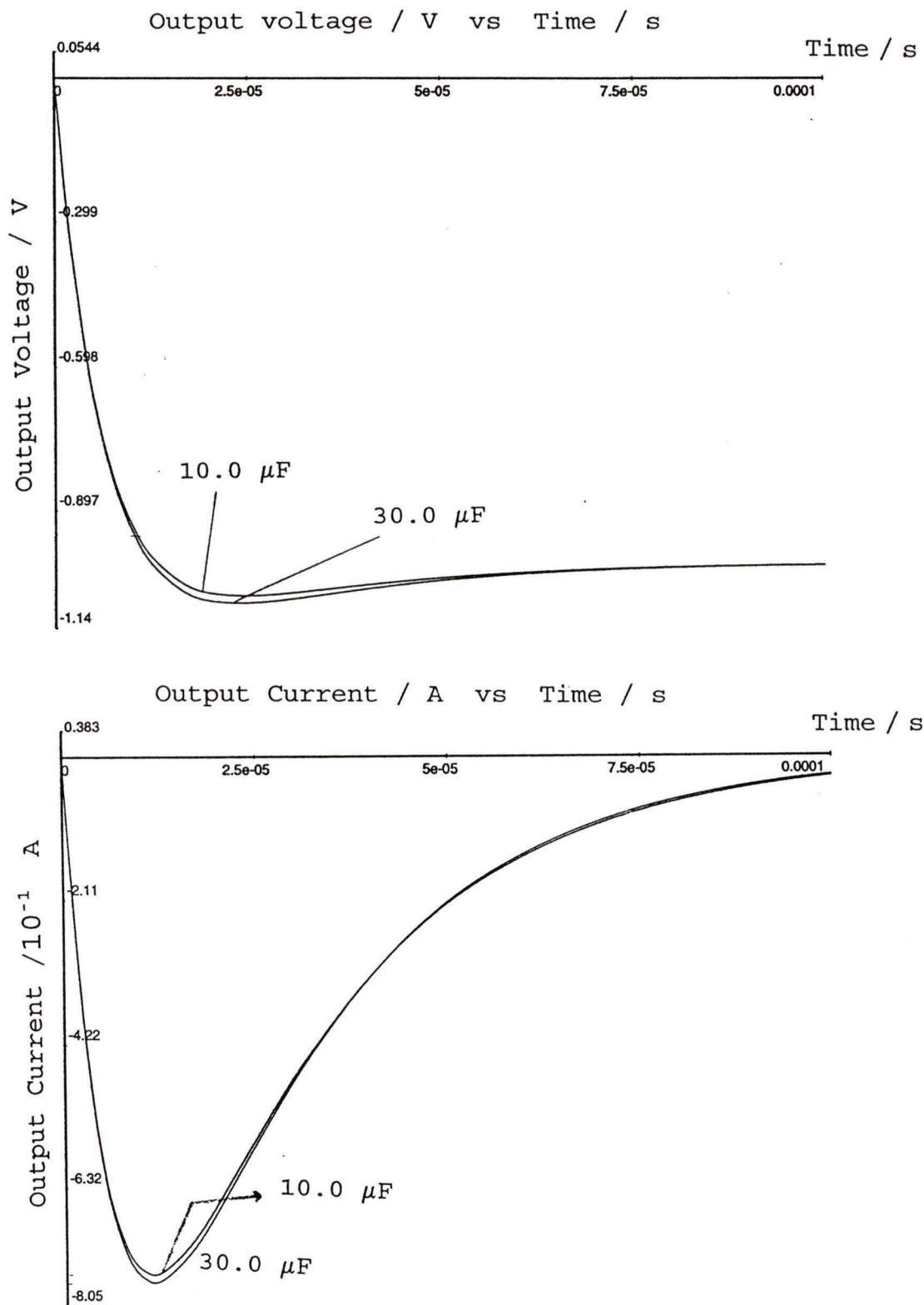


Figure 3.20 Response plots of the (a) voltage output at the RE / V, and (b) current output of the CA / A. Variation with the double layer capacitance at the CE.

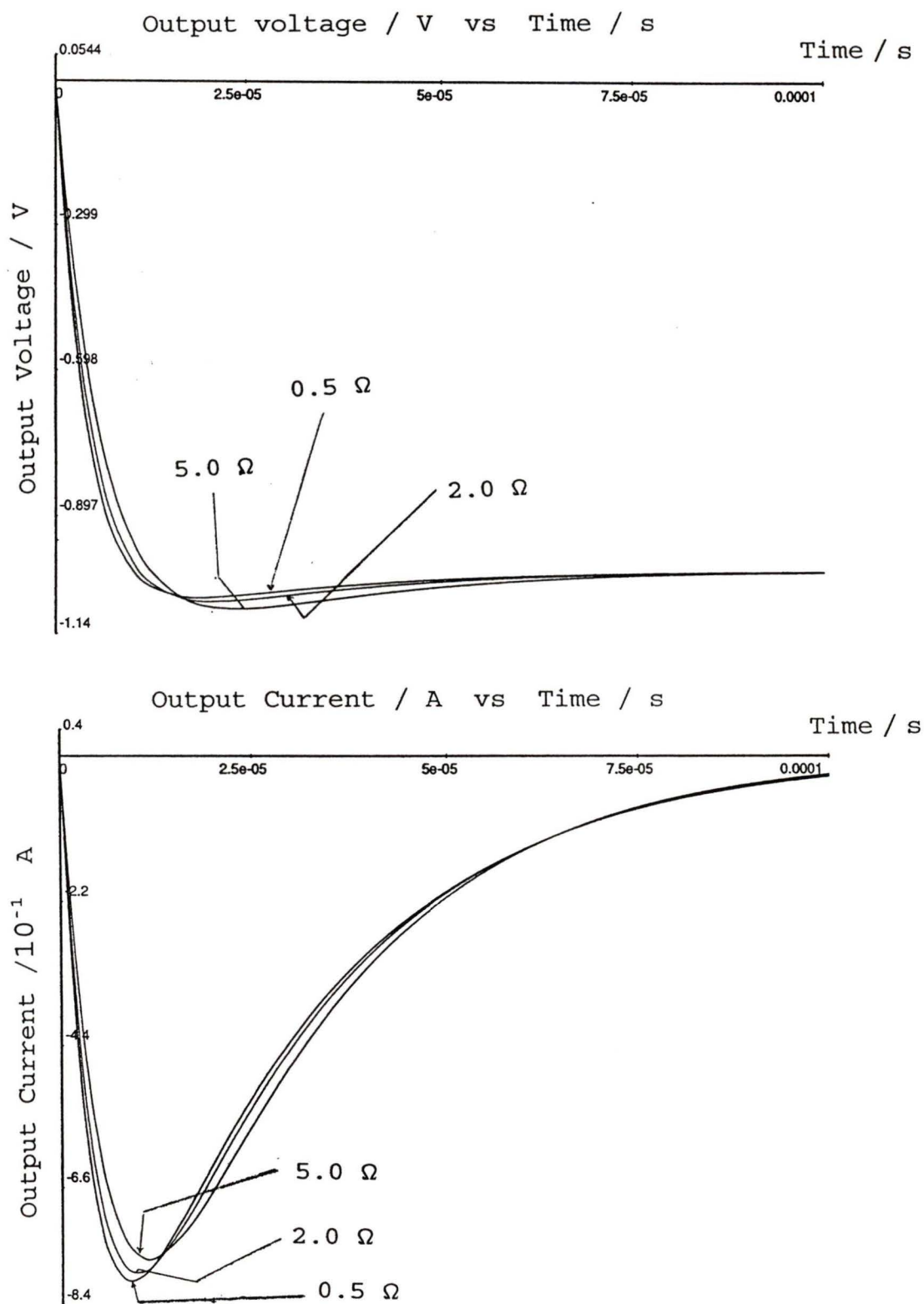


Figure 3.21 Response plots of the (a) voltage output at the RE / V, and (b) current output of the CA / A. Variation with the solution resistance.

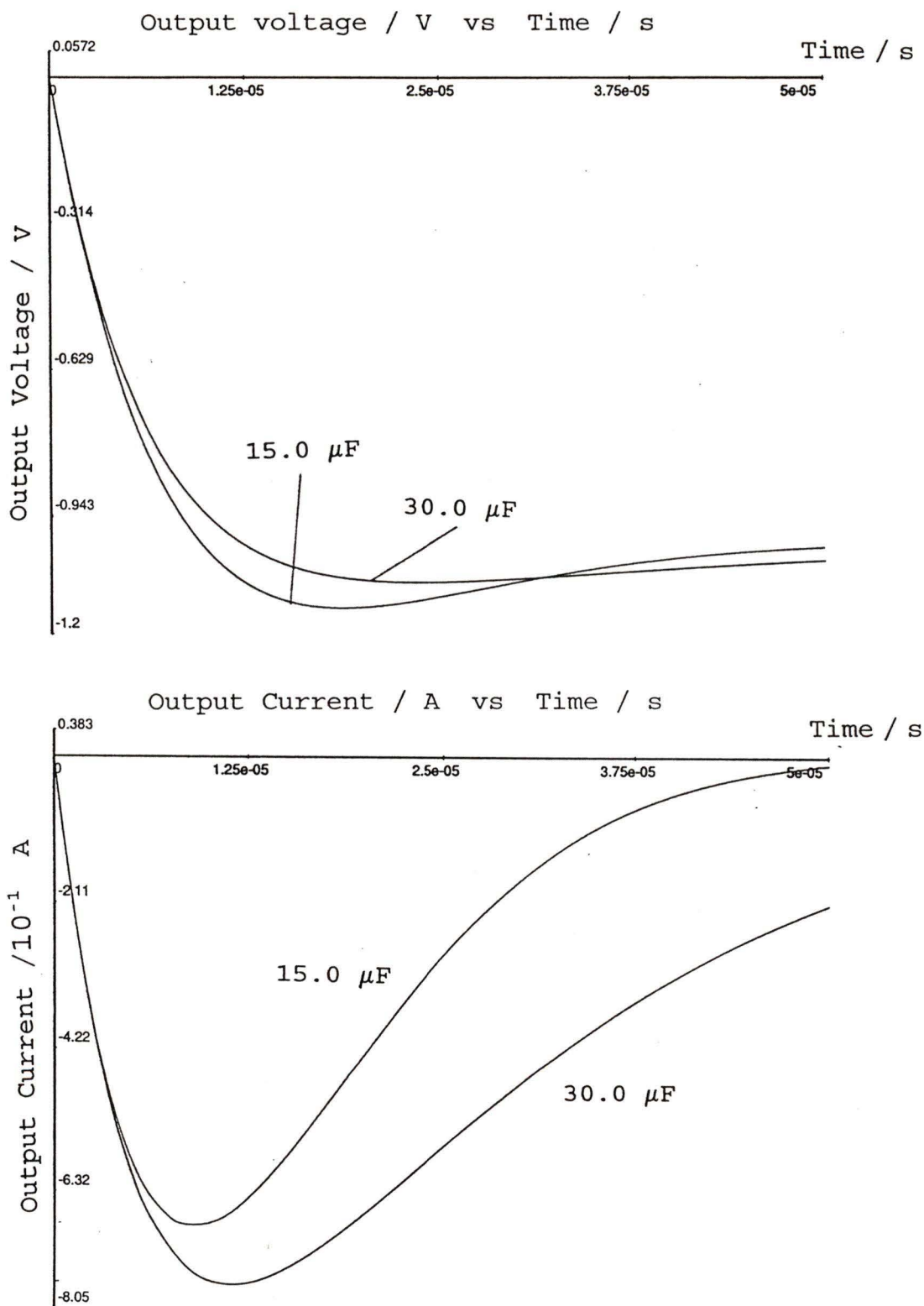


Figure 3.22 Response plots of the (a) voltage output at the RE / V, and (b) current output of the CA / A. Variation with the double layer capacitance at the WE.

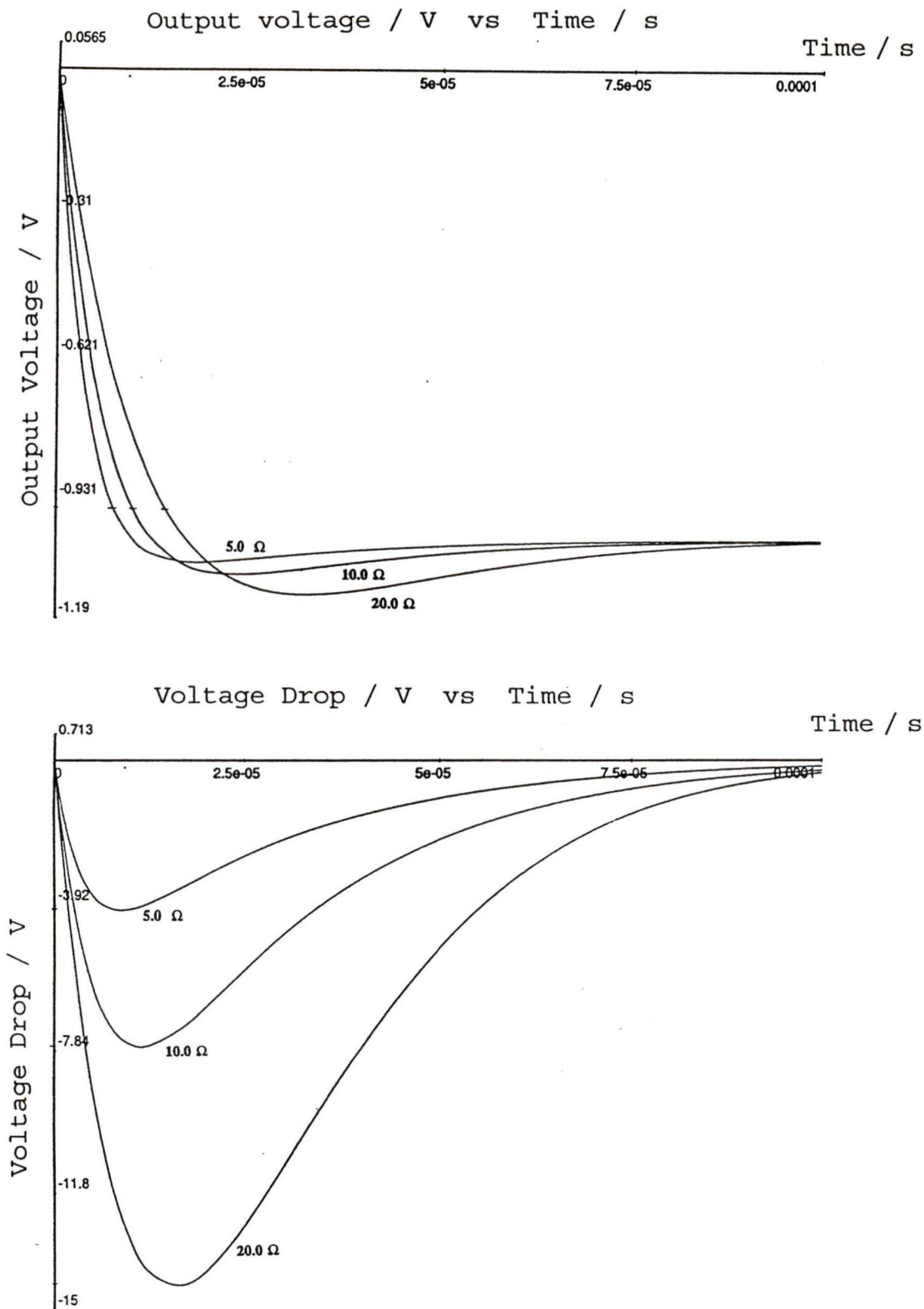


Figure 3.23 Response plots of the (a) voltage output at the RE / V, and (b) Voltage drop across  $R_1$  / V. Variation with the load resistance.

From these plots the following observations were recorded about the system's response performance:

1- *Effect of changing the  $C_d$  at the WE (i.e. by changing the surface area of the WE):*

As the  $C_d$  was made higher, the response became slower, and greater output currents were needed for charging up, (fig. 3.22).

The huge hump shown by the  $1 \mu\text{F } C_d$  (fig. 3.15) was due to the resonance in the circuit at a frequency of nearly 450 kHz. The current response plot in the time domain (fig. 3.22) showed oscillations at approximately the same frequency. Larger capacitances imposed damping to this hump.

2- *Effect of minimising  $R_u$  by advancing the LP of the RE towards the WE:*

When the  $R_u$  was too low the system was driven into oscillation. The frequency of oscillation was around 10 kHz when  $R_u = 0.5 \Omega$  (fig. 3.19). So, the response is less oscillatory when  $R_u$  was made higher. In fact, the LP is placed close to the WE to reflect accurately the potential at the surface of the WE. If the concentration of the solution is high then the voltage drop between the RE and WE is low and it is acceptable to place the LP away from the WE to improve the response.

3- *Effect of changing the solution resistance  $R_t$  by changing the following:*

- 1) Concentration of the electrolyte.
- 2) Distance between the CE and RE as well as the surface area of the electrodes.

$R_t$  was studied down to 0.01  $\Omega$  and its effect on the response of the system between 1  $\Omega$  to 0.01  $\Omega$  is approximately the same (fig. 3.21). Increasing  $R_t$  above 5  $\Omega$  will start slowing down the response, so the conductance at low concentrations should be considered as a major contributor to higher impedance through the feedback loop.

4- *Effect of changing the surface area of the CE:*

This is nearly negligible, (fig 3.20). It is not good to have the counter electrode of smaller surface area than the WE which causes inhomogenities in the distribution of the equipotential lines, hence distortion of the current paths, between the two electrodes.

5- *Effect of using a control amplifier op-amp of high  $f_b$  and  $g$ :*

The plots in fig. 3.17 and fig. 3.18 clearly show the marked improvement in response as  $f_b$  and  $g$  were made higher (table 3.1). It is easily observed that the magnitude of  $f_b$  and  $g$  characterising an op-amp plays a major part in improving the response performance when it is required to drive large

capacitive loads with the control amplifier.

6- The current-measuring resistance (or load resistance  $R_1$ ) can be easily controlled manually. It is up to the electrochemist to compromise between choosing a low  $R_1$  to achieve lower impedance, hence faster response time, or use high  $R_1$  to get a higher voltage drop across it, in order to detect weak transient current signals. Using an amplifier instead of a high load resistance introduces considerable noise. The effect of  $R_1$  on the response of the CEP system is clearly demonstrated in fig. 3.23.

However  $R_1$  should not be set to high values (greater than 100  $\Omega$ ) which could drive the system into oscillation as shown in fig. 3.24.

### 3.4 ) Circuit Design:

A practical potentiostat is now discussed. A potentiostat designed to detect fast electrode surface reactions should fulfil two criteria:

- 1 ) Fast response.
- 2 ) Good signal-to-noise ratio.

Criterion(1) was thoroughly investigated through computer simulation in order to predict the response of the CEP system, (See previous sections).

For criterion(2), the general consensus in most papers in the literature [1,7,8] is to use the minimum number of

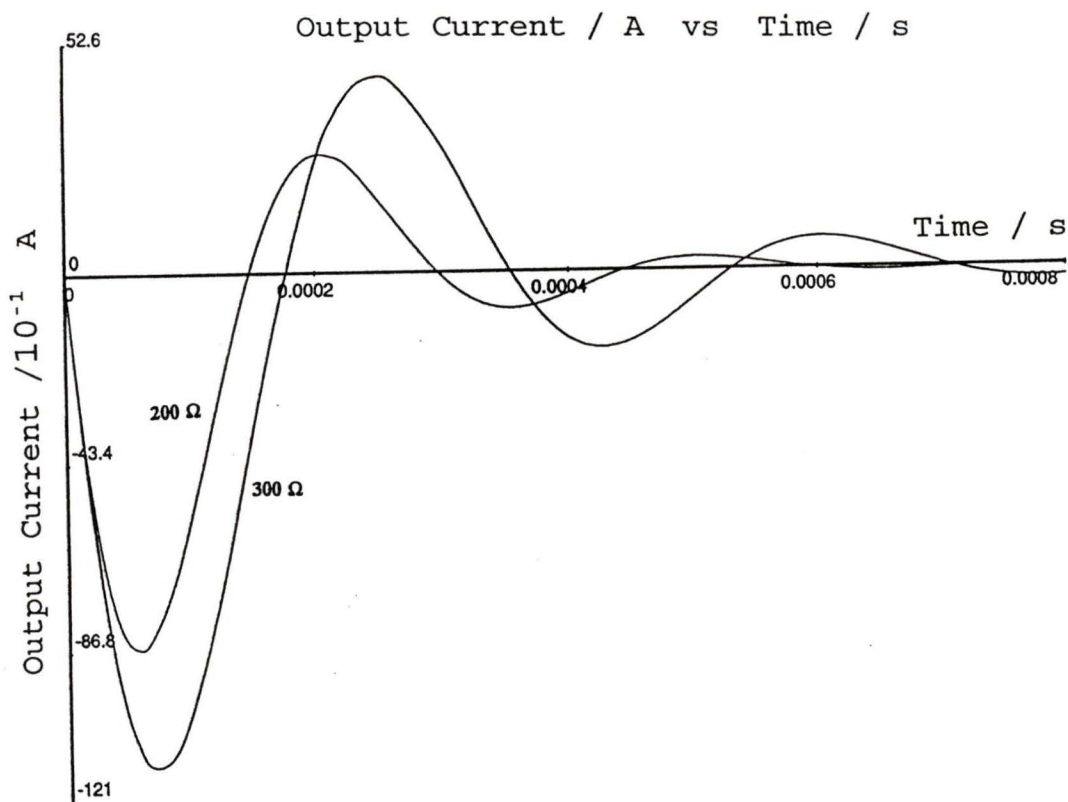


Figure 3.24 Response plots of the current output of the CA / A using high load resistance,  $R_1=200$  and  $300 \Omega$ . Note how the system is driven into oscillation.

electronic components to improve S/N ratio, and where possible, to choose components designed specifically by the manufacturer for low noise.

#### 3.4.1) Brief review on potentiostat design:

Other publications mostly concerned circuits designed for polarographic techniques. These have discussed noise, stability, and response [1-12], for electrochemical systems with micro-working electrodes (i.e. the  $C_d$  never exceeds  $2\mu\text{F}$ ). In our work, large capacitances were considered ( $30\mu\text{F}$ ), and

this changes the overall performance of the system. That is, the higher the  $C_d$  the greater is the charging current needed to be delivered by the control amplifier. The advantage gained from working with high capacitance is that the system exhibits a lower level of oscillation and the output signal settles rapidly to the required value. The main drawback to most previous publications is their failure to show response plots which would allow the experimentalist to examine the degree of stability of their circuit networks.

#### 3.4.2) Design requirements and circuit layout:

A simple two-chip potentiostat with an inverting configuration, and the WE directly grounded, is shown in fig. 3.3. This configuration was chosen because it simplifies the theory, and reduces the number of antennas that can pick up electromagnetic noise. Antennas mean here more capacitors, resistors, and electronic chips (op-amps, diodes etc.). We have also taken the precaution of running the potentiostat on d.c. (i.e. batteries), to further cut down any 60 Hz a.c. noise.

The design requirements for the VF and CA are:

##### 1 ) Voltage Follower (VF):

- rapid settling.
- moderate response.
- ultra-low noise.
- characterised by low offset voltage, and low bias current.

-high slew rate is also desirable.

Selected op-amps for the VF are LM 11, OPA 111B, OPA 60, OP 27, AD 544L, and LT 1055A.

## 2 ) Control Amplifier (CA):

-rapid settling.

-large internal input impedance.

-high slew rate.

-characterised by large bandwidth, and very low noise density.

-output current should be high enough to drive the required capacitive loads (or else a booster amplifier with sufficient output current is also used).

Selected op-amps for CA are LT 1028A,S, LF 457B, AD 744C, LF 457B, AD 843B, AD 845, LF 455B,6B, and OP 27.

Only the LF 457B and the LF 455 output 100mA currents, while the rest have maximum current outputs of 20mA. Consequently, current boosters could be a necessity to furnish the required load current.

According to theoretical simulation a step of one volt applied to a circuit of the following parameters:

$$\begin{array}{ll}
 g = 10^5 & C_d = C = 30 \mu\text{F} \\
 f_b = 62.8 \text{ rad s}^{-1} & R_u = 1 \Omega \\
 R_1 = 10 \Omega & R_t = 5 \Omega
 \end{array}$$

requires an output current of 0.8 A to achieve a response time

of 15  $\mu$ s. Higher  $g$  or  $f_b$  means shorter response times (1 to 2  $\mu$ s) at the expense of greater output currents (around 1 A). Using the ministat-potentiostat THOMPSON E-401 in our lab, a step of 20 mV applied to the cell, containing sulfuric acid solution, with the potential set at 500mV (i.e. in the double-layer region of the cyclic voltamogram, (fig. 4.6-chapter 4, where nearly no surface reactions occur) furnished a transient current signal not greater than 20 mA during a period of 10  $\mu$ s. Therefore, for potential steps less than 20 mV we may run a potentiostat without using a current booster.

The schematic of this potentiostat is shown in fig. 3.25, and the layout of the circuit board is shown in fig. 3.26. The potentiostat is designed to operate with or without a current booster depending on the user requirement. The control amplifier OP 27 is stabilised by a stabilising network (the 100 k $\Omega$  resistor, and the 33 pF capacitor in the feedback loop). The current booster LM 6321 may be severely damaged if the absolute maximum rating of 7 V between input and output pins is exceeded. The LM 6321 is best protected by the insertion of the voltage divider network (the two 100 k $\Omega$  resistors, and the 100 pF capacitor). This network has no effect on the booster output. This protection network should protect the LM 6321 from the output of the OP 27 which is operated on supply voltages of  $\pm 15$  V. Brief notes on the specifications of both op-amps are presented in appendix I.7.

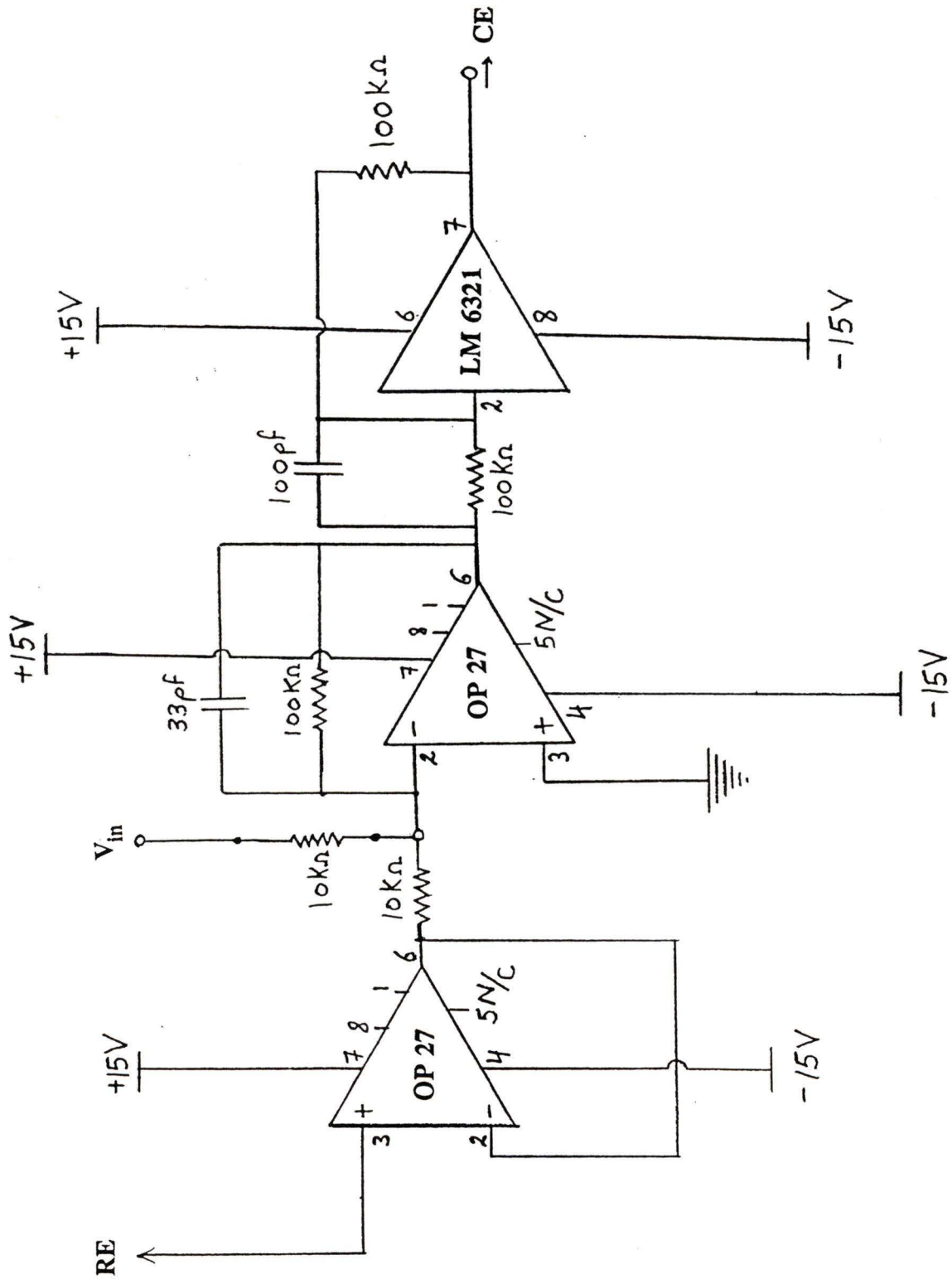


Figure 3.25 Fast response, Low noise potentiostat [Schematic]

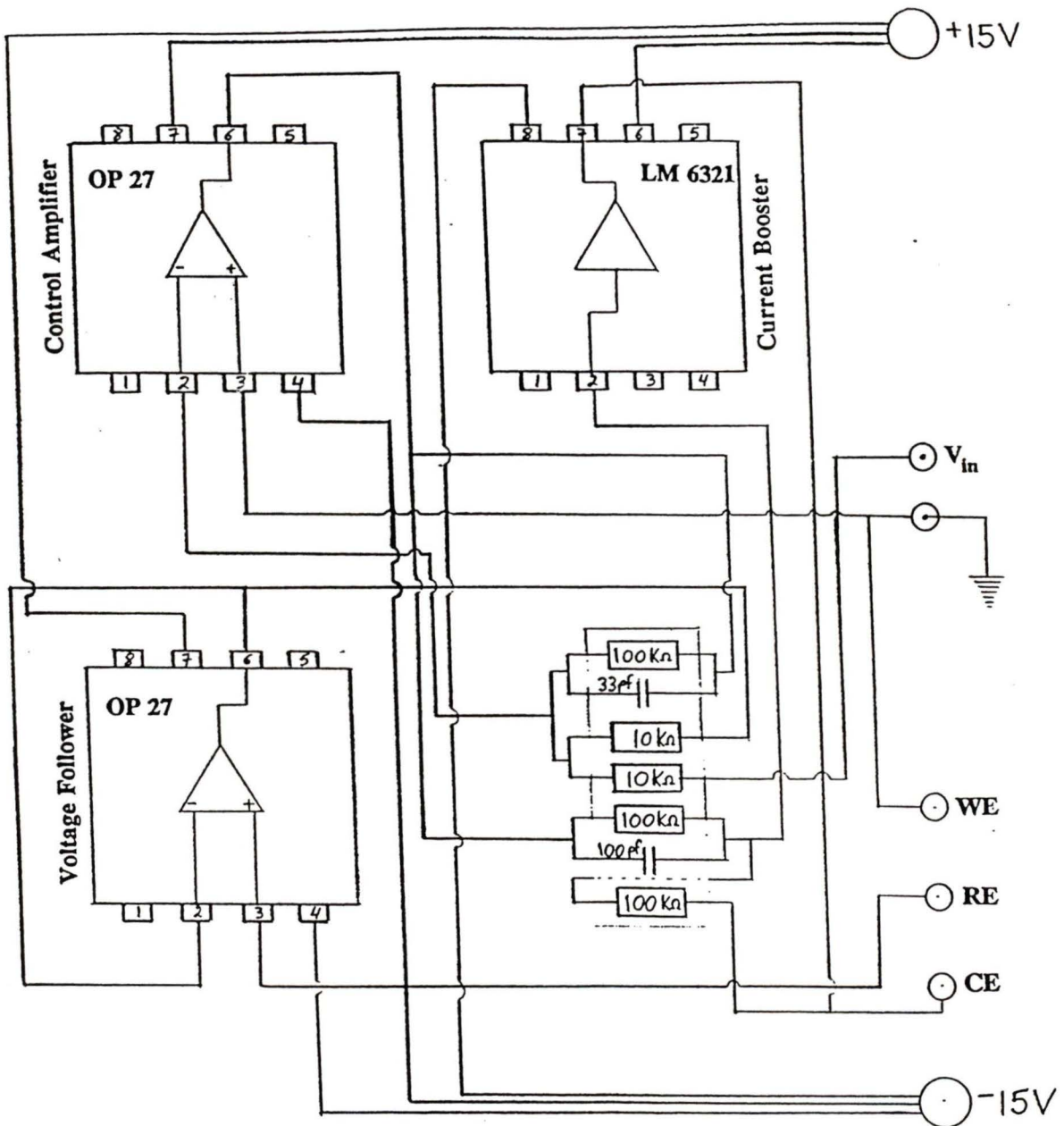


Figure 3.26 Fast response, Low noise potentiostat [Circuit Board Layout]

Chapter Four  
Studying the Hydrogen Sorption Reaction on  
Polycrystalline Platinum

4.1) Introduction:

In this chapter we discuss the analysis of the hydrogen sorption reaction using the Sweep-Step technique. Thorough experimental and theoretical work has been done on this reaction using Linear Sweep Voltammetry, Cyclic Voltametry, and the A.C. Impedance technique, [15-18,40-46]. However, the advantage of using the Sweep-Step technique is that it simplifies the mathematics, is experimentally more robust (i.e. takes less time and is simpler to operate), and allows the user to learn more about the shape of sorption isotherms, interaction parameters, and symmetry factors. The meaning of these terms will be discussed later.

In the Sweep Step method the potential is linearly swept from nearly zero up to a desired value ( $E_b$ ) where a potential step of a few millivolts (positive or negative) is applied, and the potential is then held constant at  $E_h$  (fig 4.1). It follows that the hydrogen sorption reaction is studied at a constant potential. The current generated at a constant potential is a decaying transient (fig. 4.2). The integral of the decay current with time measures the net amount of the hydrogen adatoms that have either desorbed or adsorbed in the constant potential part of the experiment.

**A schematic of the Sweep-Step signal used in the  
Sweep-Step method.**

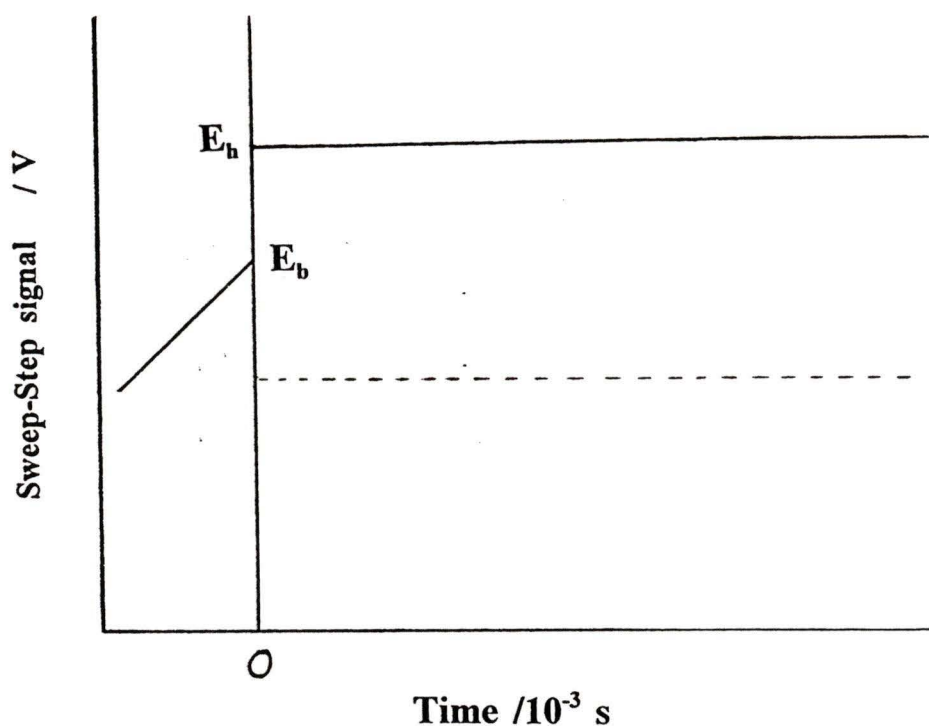


Figure 4.1 Schematic of the Sweep-Step signal used in the Sweep-Step method. Positive (solid line) and negative (dotted line) potential steps are shown.

4.2) Experimental Procedure:

The function generator (FG) and the step generator (SG) were synchronized to provide the Sweep-Step signal, (Instrumentation and hardware are presented in detail in chapter 2, fig. 2.1). The FG was used to sweep up to the required potential and send a trigger pulse to the SG. The latter immediately output a potential step of the required magnitude and sign( $\pm$ ) set already by the user (e.g. +5 mV or -10 mV). The two outputs from the FG and SG were summed by the potentiostat.

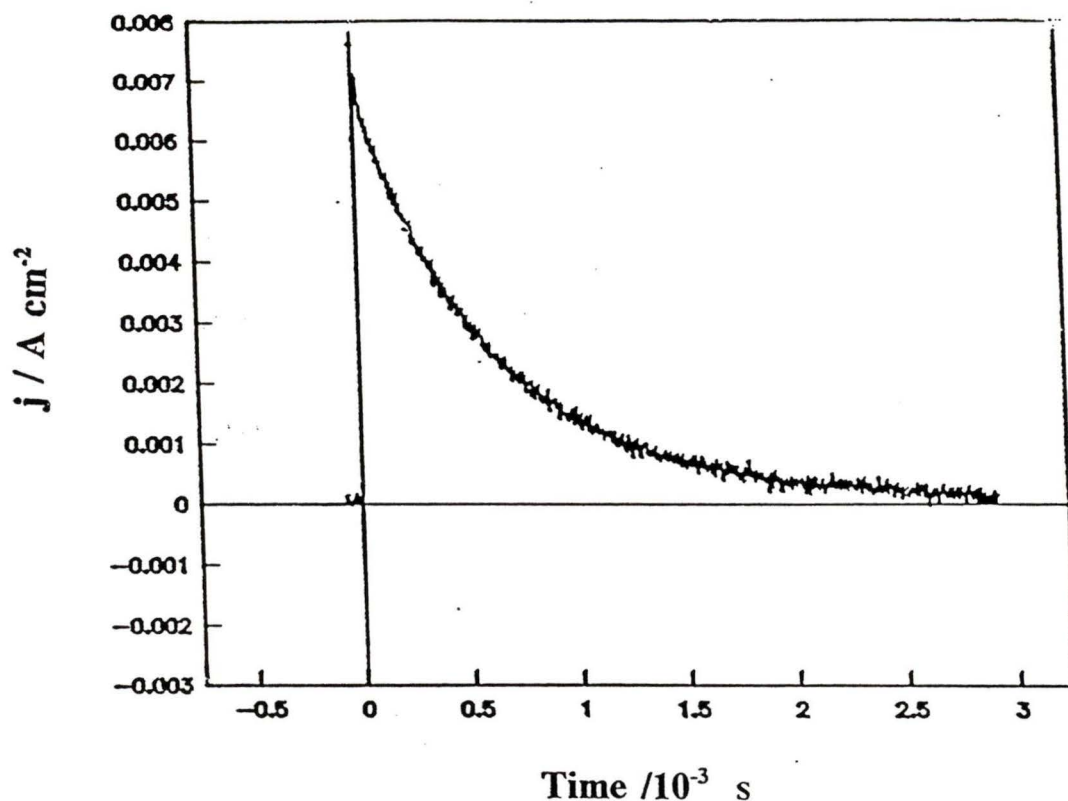


Figure 4.2 A plot of the decay current due to H-desorption on platinum in 2M H<sub>2</sub>SO<sub>4</sub> solution. The current is generated by a +10 mV potential step at  $E_b = .24$  V where the potential is held constant at  $E_h = 0.25$  V.  $\nu = 0.2$  V s<sup>-1</sup>.

Before running the experiment the SG was set to zero in order to check on the background signal, which was the sum of the two voltage signals coming from the FG and SG. A slight glitch usually appeared at the point where the potential step was applied. In our experiment this glitch was observed to decay to zero within 4 to 5  $\mu$ s and the amount of charge generated by it was less than 0.02  $\mu$ C, corresponding to a charge of less than 10<sup>-4</sup> monolayers of coverage and a transient current of approximately 0.01  $\mu$ A.

The SG outputs a trigger signal to the oscilloscope in

order to synchronize the data acquisition. Digital pretriggering was used to capture the signal beginning a few milliseconds before the potential step.

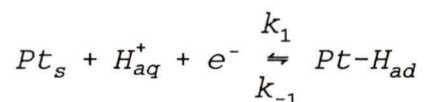
In order to measure the current through the CE, a current measuring resistor  $R_1$  was connected between the CE terminal of the potentiostat and the electrode itself. The voltage drop across  $R_1$  was measured by the differential amplifier of the oscilloscope. So, the current signal was sampled in volts, and was divided by  $R_1$  which was set to  $6 \Omega$  in the Sweep-Step experiments. Care was taken not to use too large an  $R_1$  as this would slow down the response of the potentiostat and drive the potentiostat-electrochemical system into oscillation as discussed in chapter three (section 3.3). The potential difference between the WE and RE was also measured using the potentiostat's internal voltage follower. The signals collected by the oscilloscope were passed to the computer using 'Waveform Basic' software.

#### 4.3) Theory:

As noted above, decaying current signals are produced when the potential is held constant. In this section, an equation is derived for the decay current as a function of the electrode potential  $E$  and the overall rate constant  $k$  ( $\text{mol cm}^{-2} \text{s}^{-1}$ ), ( $k = k_1[\text{H}^+] + k_{-1}$ , where  $k_1$  is the forward rate constant of adsorption and  $k_{-1}$  is the reverse rate constant of desorption). By comparison with experimental results, the

decay equation was used to determine the values of  $k$ , symmetry factor  $\beta$ , and to check whether the interaction parameters were significant or not.

The reaction which describes H-sorption on a platinum surface is:



where,

$Pt_s$  is an uncovered site on the platinum surface.

$H_{aq}^+$  is an aqueous hydroxonium ion.

$Pt-H_{ad}$  is hydrogen adsorbed on a platinum site.

Assuming the Langmuir isotherm, where the interactions between the adsorbed hydrogens are negligible, the rate equation which describes this reaction is [15-18]:

$$\Gamma_m \frac{d\theta}{dt} = k_1 [H^+] (1-\theta) - k_{-1}\theta \quad (4.1)$$

where  $\Gamma_m$  ( $\text{mol cm}^{-2}$ ) is the surface concentration associated with a full monolayer coverage,  $[H^+]$  is the concentration of the hydroxonium ions in solution, and  $\theta$  is the fraction of the covered sites (which varies with electrode potential  $E$ , fig. 4.3). Coverage is defined in terms of charge density:

$$\theta = \frac{\sigma}{\sigma_m} \quad (4.2)$$

where  $\sigma$  is the charge density associated with a

fractional coverage  $\theta$ , and  $\sigma_m$  is the charge density associated with a full monolayer coverage. The charge density is related to surface concentration by:

$$\sigma = nF\Gamma \quad (4.3)$$

where  $n$  refers to the number of electrons per adsorbate ( $n=1$  for the H-sorption reaction), and  $F$  is the Faraday constant. For polycrystalline platinum in acidic solution  $\sigma_m = 220 \mu\text{C cm}^{-2}$ .

Change of coverage  $\theta$  with Potential during desorption (Langmuir isotherm)

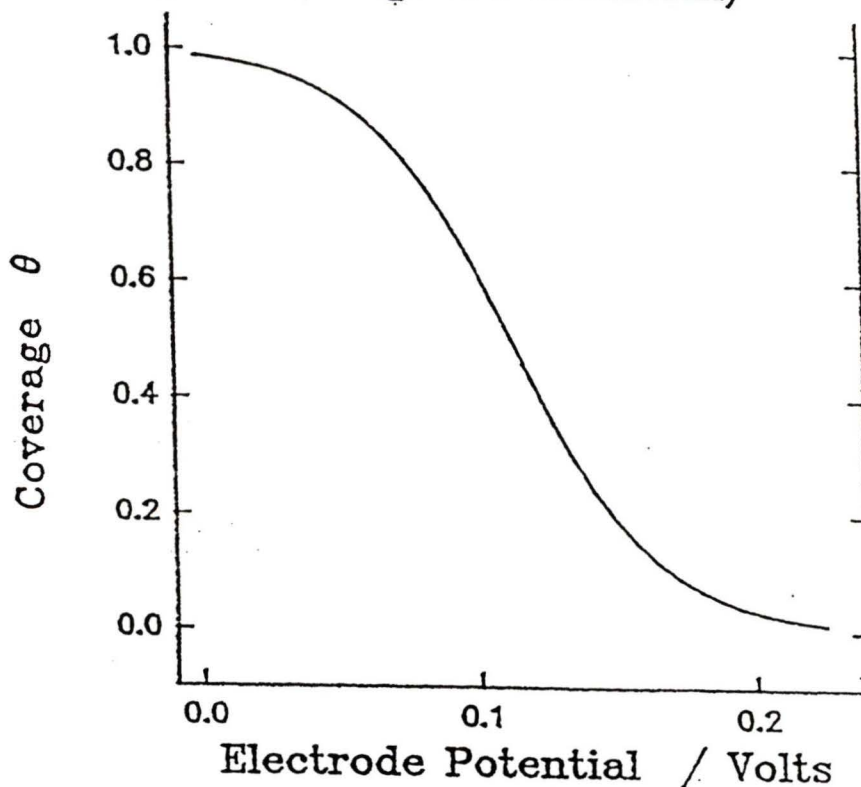


Figure 4.3 Schematic showing the change of  $\theta$  with  $E$  for the Langmuir isotherm. (Strictly applicable only under equilibrium conditions)

As in any electron transfer step, the rate constants are functions of  $E$  such that:

$$k_1 = k_1^\circ \exp\left[\frac{-\beta F(E-E^\circ)}{RT}\right] \quad (4.4)$$

$$k_{-1} = k_{-1}^\circ \exp\left[\frac{(1-\beta) F(E-E^\circ)}{RT}\right] \quad (4.5)$$

where  $\beta$  is a symmetry factor which has values between 0 and 1, and the  $k^\circ$  values are the rate constants at standard potential  $E^\circ$ .

### Change of Rate Constants with Potential showing the resultant minimum at $\beta=0.5$

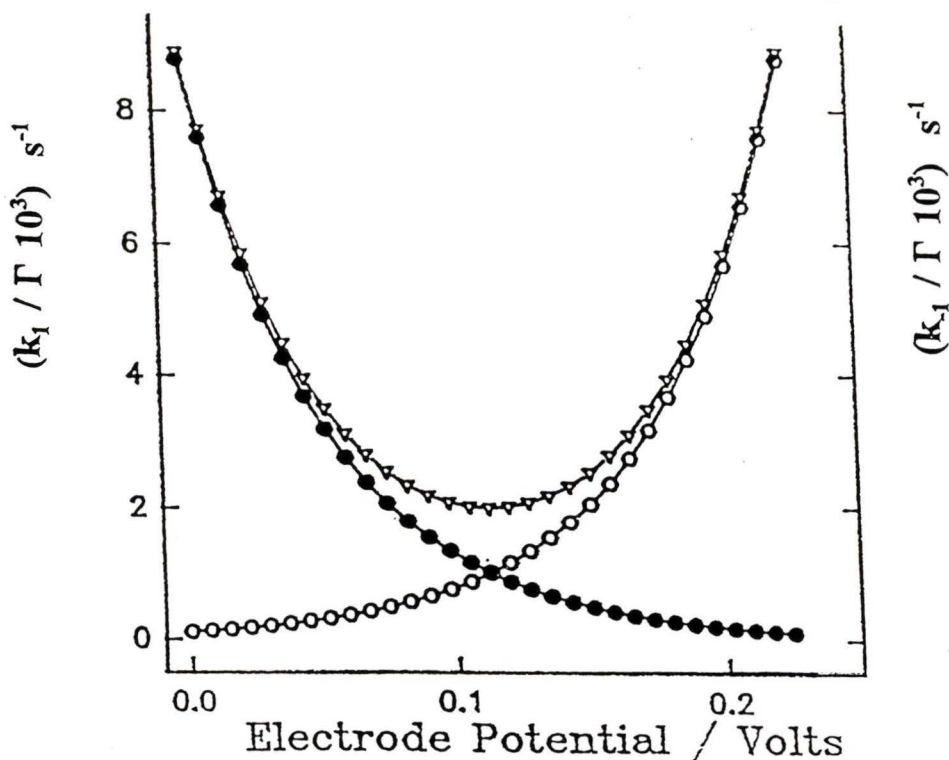


Figure 4.4 Schematic showing the change of  $k(v)$  with  $E$  for  $\beta = 0.5$ . The other two curves show the change of  $k_1(\bullet)$  and  $k_{-1}(o)$  with  $E$ .

The change of the rate constants with E (this is the  $E_h$  potential in our experiments) is shown in fig. 4.4. The resultant minimum (dotted curve) expressing the change of k with E, is symmetric for a value of  $\beta$  equal to one half. The potential where k is minimum is the standard potential  $E^\circ$  and the standard state is chosen as half coverage, i.e.  $\theta^\circ = 1/2$ .

Referring back to fig. 4.3, it is seen that a plot of  $d\theta/dE$  versus E yields a maximum. However, during a Sweep experiment, the sweep rate ( $\nu = dE/dt$ ) stays constant, hence plotting  $d\theta/dt$  versus t also yields a maximum. Using eq. (4.2), differentiating  $\theta$  and  $\sigma$  with respect to time and then rearranging we get:

$$j = \frac{d\sigma}{dt} = \sigma_m \frac{d\theta}{dt} \quad (4.6)$$

where j is the current density ( $A\ cm^{-2}$ )

Therefore, as the potential (or time) changes j should yield a maximum. The peaks present in the hydrogen region of the cyclic voltamogram, shown in fig. 4.5, are good examples of the above phenomenon. Actually, the two H-sorption peaks are due to the current density generated by hydrogens chemisorbing at two different crystallographic platinum sites. These are the Pt(110) for the unshaded peak, and Pt(100) for the shaded one [22]. The shaded peak is the main focus of this study.

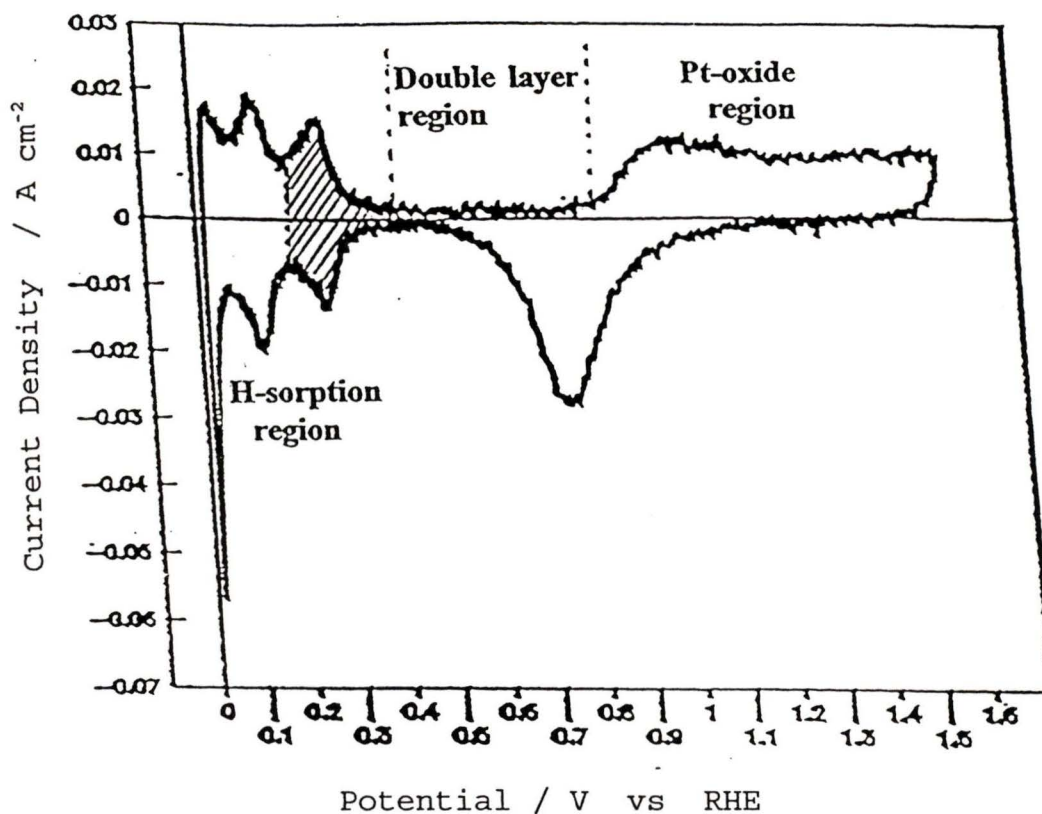
Cyclic Voltammogram of Pt / 2M H<sub>2</sub>SO<sub>4</sub>

Figure 4.5 Cyclic voltammogram of polycrystalline platinum in 2M H<sub>2</sub>SO<sub>4</sub> solution. Area of WE=0.6 cm<sup>2</sup>,  $\nu = 0.2 \text{ V s}^{-1}$

We conclude that, as the potential is increased,  $k$  changes and yields a minimum while the current density yields a maximum. However, when the potential is held constant  $k$  stays constant (from eqs. 4.4 and 4.5), and then the problem to solve is to prove theoretically that the current density decays exponentially to zero with time, as presented experimentally (fig. 4.2). This is done by solving the differential equation eq.(4.1) which is relatively simple since  $k$  stays the same as the potential is held constant.

We solve the differential equation by rearranging and

integrating, taking  $\theta = \theta_0$  at  $t = 0$  ( $\theta_0$  is the state of coverage at  $E_b$ ), to get:

$$\theta(t) = \theta_0 \exp\left[-\frac{(k_1[H^+] + k_{-1})}{\Gamma_m} t\right] \quad (4.7)$$

If this equation is differentiated with respect to time:

$$\frac{d\theta}{dt} = -\theta_0 \frac{(k_1[H^+] + k_{-1})}{\Gamma_m} \exp\left[-\frac{(k_1[H^+] + k_{-1})}{\Gamma_m} t\right] \quad (4.8)$$

Substituting for  $d\theta/dt$  in eq. (4.6):

$$\frac{d\sigma}{dt} = \sigma_m \theta_0 \frac{(k_1[H^+] + k_{-1})}{\Gamma_m} \exp\left[-\frac{(k_1[H^+] + k_{-1})}{\Gamma_m} t\right] \quad (4.9)$$

$$\Rightarrow j(t) = j_0 \exp\left[-\frac{(k_1[H^+] + k_{-1})}{\Gamma_m} t\right] \quad (4.10)$$

Therefore, a plot of  $\ln(j)$  vs  $t$  should be linear with a slope equal to  $-(k_1[H^+] + k_{-1})/\Gamma_m$  i.e. the slope is equal to the time constant of the decay. This is clearly illustrated in fig. 4.6 which uses the data for the decay curve shown in fig. 4.2.

We have tested this differential equation using the Sweep-Step method for platinum in sulfuric acid solutions (1, 2, 4 and 6 mol  $\text{dm}^{-3}$ ) and in perchloric acid solution (1 mol  $\text{dm}^{-3}$ ).

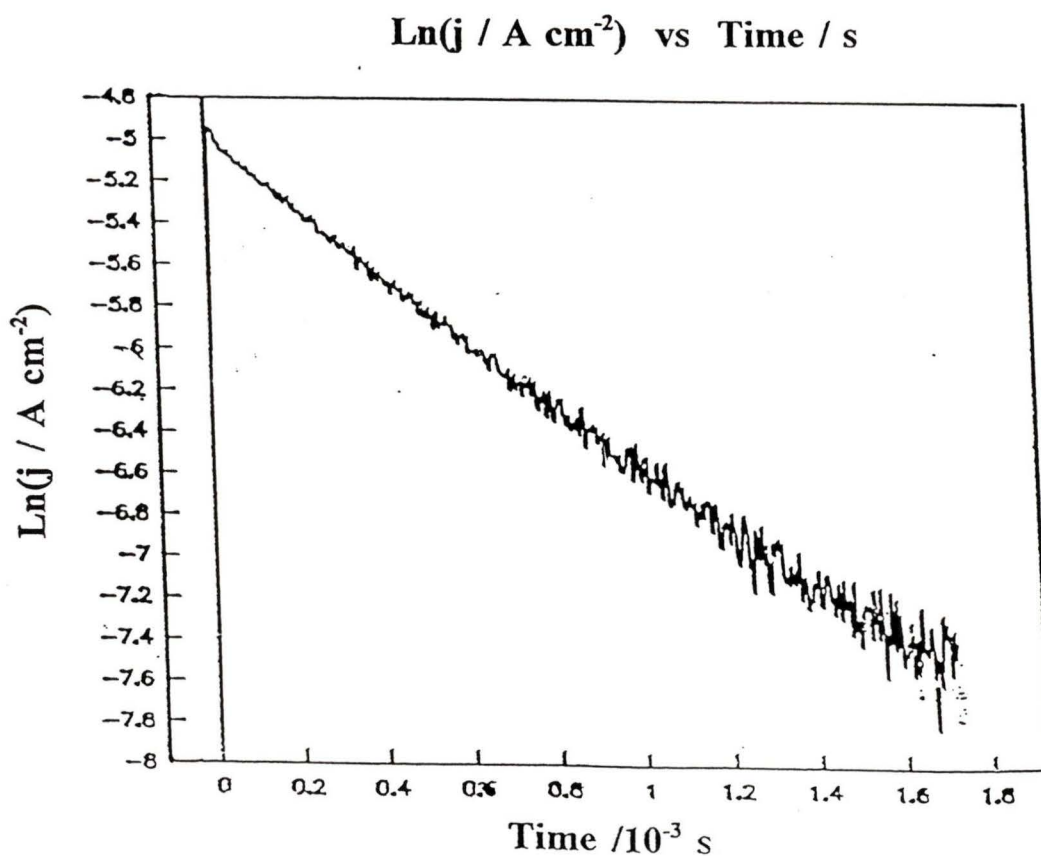


Figure 4.6 A plot of  $\ln(j / \text{A cm}^{-2})$  vs Time / s. This corresponds to the decay plot of figure 4.2.

#### 4.4) Results and Discussion:

The experimental results obtained for the hydrogen sorption reaction using the Sweep-Step technique were as follows:

- 1) *Freedom from artifacts:* It is important to show that the decay current signal was due to hydrogen adatoms adsorbing or

desorbing and not to instrumental artifacts. This was proved by first determining the total amount of charge ( $Q_d$ ) under the decay current curve in a Sweep-Step experiment (e.g. fig. 4.2). Note that the reaction is close to equilibrium before the step at  $E_b$  and is again close to equilibrium at  $E_h$  a long time after applying the potential step. The change in coverage should therefore equal that between  $E_b$  and  $E_h$  in the equilibrium isotherm (fig. 4.3). The same change in coverage should occur in the cyclic voltammogram (CV) experiment between  $E_b$  and  $E_h$  because the reaction is always close to equilibrium in this experiment. Therefore,  $Q_d$  was compared to the corresponding amount of charge  $Q_c$  determined from the CV (fig. 4.5), for the same potential range.

The  $Q_d$  values for a fixed  $E_b$  and a variety of different  $E_h$  values are shown in table 4.1. The corresponding  $Q_c$  changes are given in table 4.2. Good agreement was found. The percentage difference was well within experimental limits (less than 10 %), and this showed that the results, and hence the decay current signals, were reflecting genuine electrochemical processes and not an instrumental artifact.

2) *Effect of step direction*: Positive and negative potential steps were applied at a variety of  $E_b$  potentials in order to investigate the kinetics of the hydrogen adsorption and desorption reactions at different coverages. The graph of the decay current signal due to a positive potential step, (fig.

4.2), is typical of a large number of graphs (more than a hundred) that were used to study the kinetics of the H-sorption reaction.

In these experiments, the potential was swept in the

Table 4.1 :

Total charge under the decay current signal using the Sweep Step method.  $E_b=0.22$  V,  $\nu=0.2$  V s<sup>-1</sup>, 4M H<sub>2</sub>SO<sub>4</sub> solution. Last column is the difference between these charges and those of table 4.2

POT. STEP/ mV	INT.AREA /V ms	CHARGE/ $\mu$ C	% Discrepancy
+5	0.0124	2.06	10.0
+10	0.0241	4.03	7.0
+15	0.0378	6.30	1.3
+20	0.0525	8.75	2.7

Table 4.2 :

Total Charge between  $E_b= 0.22$  V and  $E_h$  measured from the cyclic voltamogram of Pt / 4M H<sub>2</sub>SO<sub>4</sub> solution

POT. STEP/ mV	INT.AREA/V ms	CHARGE/ $\mu$ C
+5	0.1054	2.29
+10	0.1998	4.34
+15	0.2937	6.38
+20	0.3920	8.51

positive direction at a rate of  $0.2 \text{ V s}^{-1}$  to a potential  $E_b$  (say,  $0.18 \text{ V}$ ) and a potential step of ( $\pm 10 \text{ mV}$ ) was then applied. Consequently, the rate of desorption was studied at a constant potential of  $0.19 \text{ V}$ , while the rate of adsorption was studied at a constant potential of  $0.17 \text{ V}$ . The experiment was then repeated at different  $E_b$  potentials (say,  $0.2, 0.22, \dots, 0.5 \text{ V}$ ), for potential step heights of  $\pm 10 \text{ mV}$ , to obtain new values of  $k$  from the corresponding decay curves. As noted in section 4.3, using the decay current signal we can determine  $k$  from a plot of  $\ln(j)$  vs  $t$ . Plotting  $k$  against  $E_h$  yields two minima, indicated by different symbols, that correspond to potential steps of different signs ( $\pm$ ) (figs. 4.7, 4.8, 4.9 and 4.10).

Considering the plots of  $k$  vs  $E_h$  for the  $\text{H}_2\text{SO}_4$  solutions, note how the falling edges of the minima are coinciding (for positive and negative steps), while the rising edges split apart violating eqs. 4.4 and 4.5. Therefore, the rate constant is not only a function of potential but depends to a small extent on other variables which are yet to be characterised and determined. The rate equation (eq. 4.1) may be modified to account for the interaction effects between the hydrogen adatoms. Modification to eq.(4.1) is usually done by multiplying  $\theta$  and  $(1 - \theta)$  terms by  $\exp(-h \theta)$  and  $\exp(-g \theta)$  respectively, where  $h$  and  $g$  are interaction parameters that cause departures from the shape of the Langmuir isotherm [16,18].

In this case, the rate becomes a more complex function of coverage, and hence more difficult to manipulate.

The differential equation which would then express the overall process is:

$$\Gamma_m \frac{d\theta}{dt} = k_1 [H^+] (1-\theta) \exp[-g\theta] \exp\left[\frac{-\beta F(E-E^0)}{RT}\right] - k_{-1} \theta \exp[-h\theta] \exp\left[\frac{(1-\beta) F(E-E^0)}{RT}\right] \quad (4.11)$$

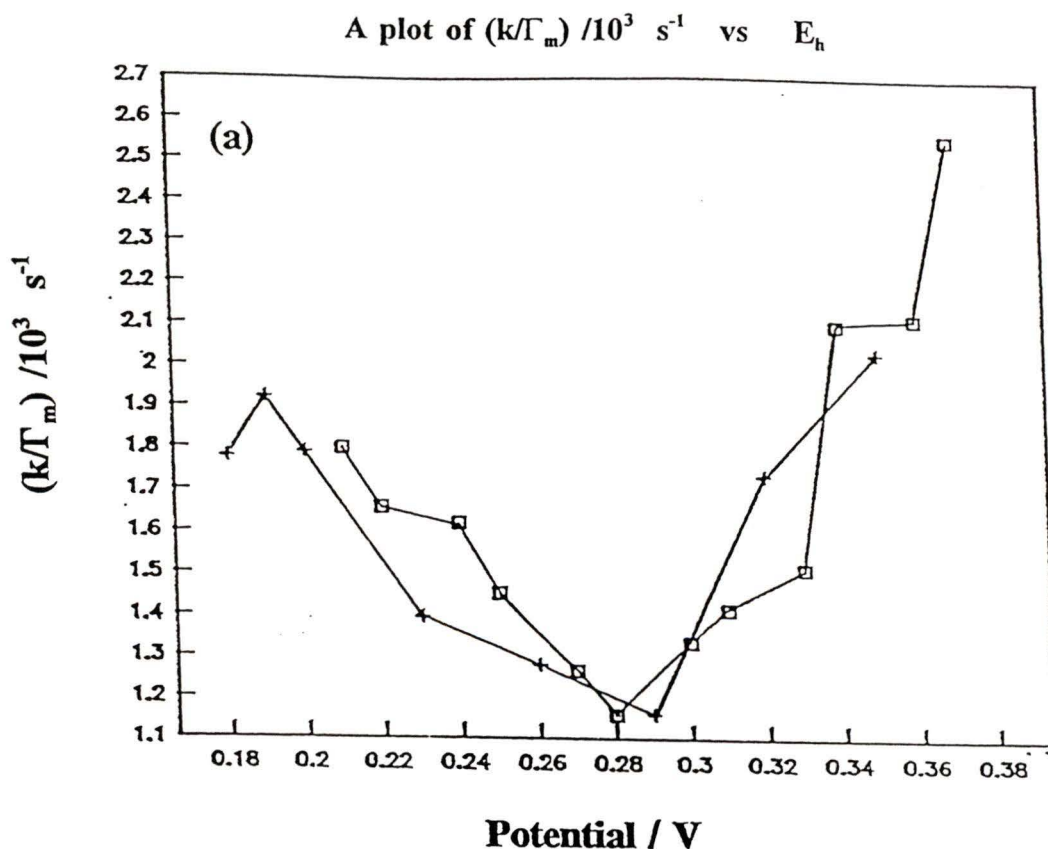


Figure 4.7 A plot of  $(k/\Gamma_m) / \text{s}^{-1}$  against  $E_h / \text{V}$  vs RHE during H-desorption on Pt between 0.18 and 0.4 V in 1M HClO<sub>4</sub> for (+10 mV) □ and (-10 mV) + steps. Area of WE=0.6 cm<sup>2</sup>,  $\nu = 0.2 \text{ V s}^{-1}$ .

No attempt was made to obtain values of  $g$  and  $h$  since fitting procedures are unreliable for such a large number of parameters.

3) *Effect of step magnitude:* Potential steps of different magnitudes were applied, at a fixed  $E_b$  potential to investigate the effect of the magnitude of the step on the rate of the decay of the current. For example, an  $E_b$  potential

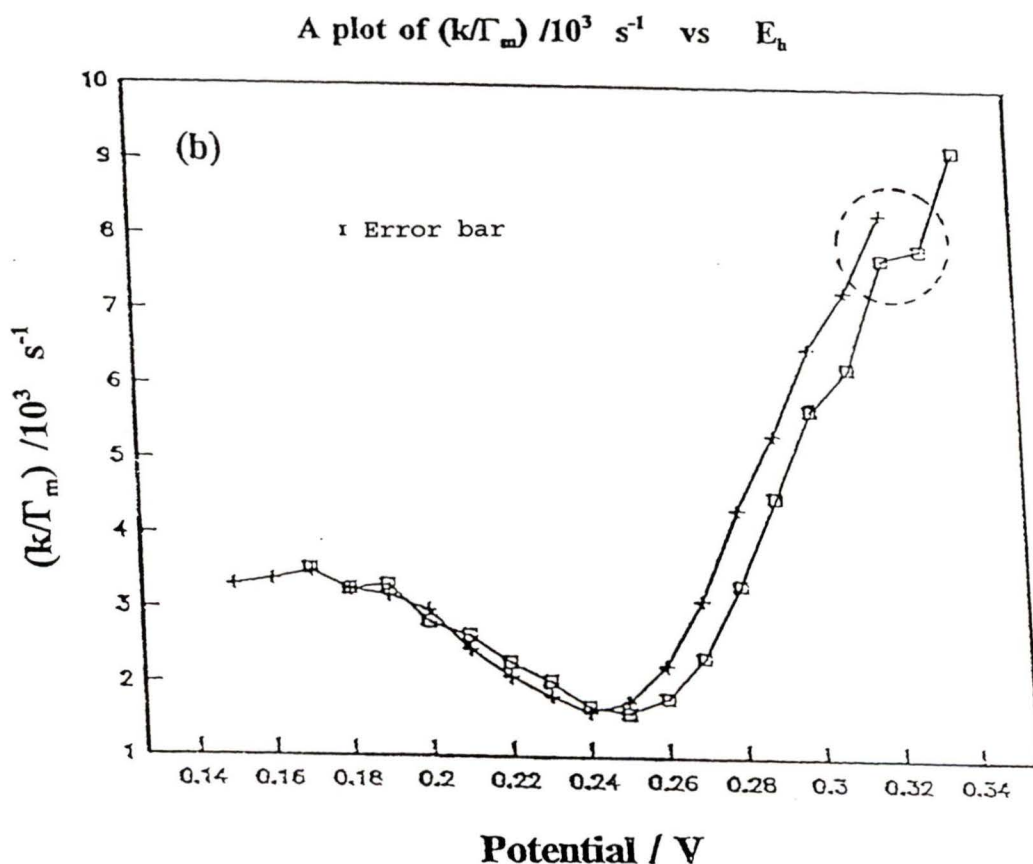


Figure 4.8 A plot of  $(k/\Gamma_m) / \text{s}^{-1}$  against  $E_b / \text{V}$  vs RHE during H-desorption on Pt between 0.18 and 0.4 V in 2M  $\text{H}_2\text{SO}_4$  for (+10 mV)  $\square$  and (-10 mV)  $+$  steps. Area of  $\text{WE} = 0.6 \text{ cm}^2$ ,  $\nu = 0.2 \text{ V s}^{-1}$ . Error bar indicates the standard error of deviation of the slope of the regression line.

of 0.2 V was selected and potential steps of +5mV or +10mV were applied. Consequently, the rate of desorption was studied at constant  $E_h$  potentials of 0.205 V, 0.210 V.

This procedure is illustrated with a plot (fig 4.11), showing the change of  $k$  with  $E_h$  in a sulfuric acid solution at a concentration of 4 mol dm<sup>-3</sup>. Data points corresponding to different step heights are given different symbols.

It appears that the behaviour of the composite rate constant  $k$  as a function of potential is independent of the

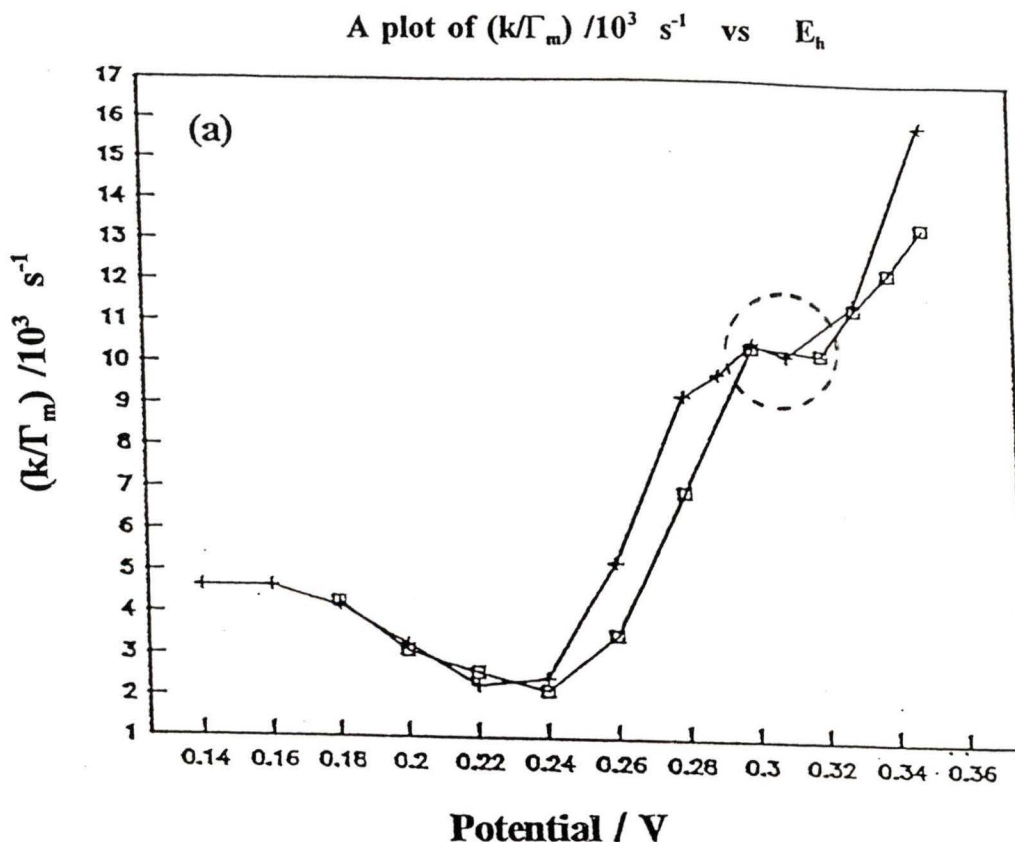


Figure 4.9 A plot of  $(k/\Gamma_m) / \text{s}^{-1}$  against  $E_h / \text{V}$  vs RHE during H-desorption on Pt between 0.18 and 0.4 V in 4M H<sub>2</sub>SO<sub>4</sub> for (+10 mV) □ and (-10 mV) + steps. Area of WE=0.6 cm<sup>2</sup>,  $\nu = 0.2 \text{ V s}^{-1}$ .

magnitude of the potential step at least up to  $\pm 20$  mV. This suggests that the rate of desorption of hydrogen from the surface is not affected by the changes in potential between  $E_b$  and  $E_h$ , i.e. by the prior history. This is in agreement with theory where the  $k$  value at  $E_h$  is the only determinant of the decay constant in eq. 4.10. Factors such as surface diffusion could lead to memory effects, where mathematically the rate is not only a function of  $E$  and  $\theta$ . However, such complexities do not appear to be operative here.

A plot of  $(k/\Gamma_m) / 10^3 \text{ s}^{-1}$  vs  $E_h$

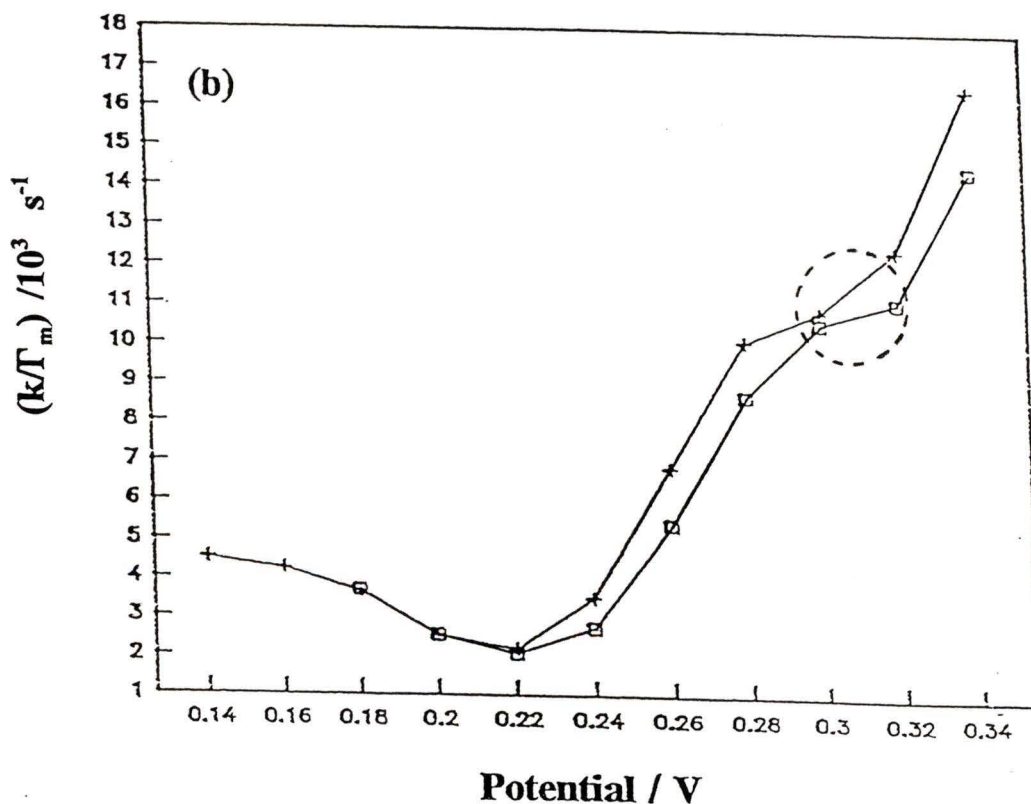


Figure 4.10 A plot of  $(k/\Gamma_m) / \text{s}^{-1}$  against  $E_h / \text{V}$  vs RHE during H-desorption on Pt between 0.18 and 0.4 V in 6M  $\text{H}_2\text{SO}_4$  for (+10 mV)  $\square$  and (-10 mV)  $+$  steps. Area of WE=0.6  $\text{cm}^2$ ,  $\nu = 0.2 \text{ V s}^{-1}$ .

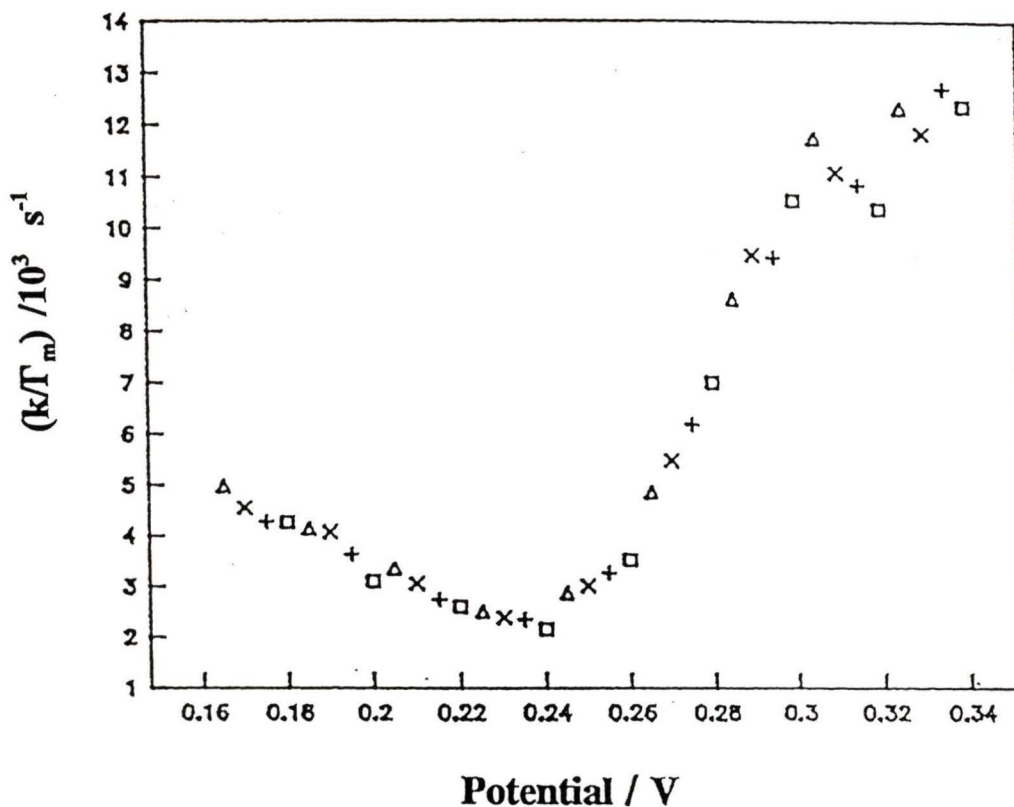
A plot of  $(k/\Gamma_m) / 10^3 \text{ s}^{-1}$  vs  $E_h$ 

Figure 4.11 A plot of  $(k/\Gamma_m) / \text{s}^{-1}$  against  $E / \text{V}$  vs RHE during H-desorption on polycrystalline platinum between 0.18 and 0.4 V in 4M  $\text{H}_2\text{SO}_4$ , for potential steps of +5 (+), +10 (x), +15 ( $\Delta$ ), and +20 ( $\square$ ) mV. Area of WE=0.6  $\text{cm}^2$ ,  $\nu=0.2 \text{ V s}^{-1}$ .

4) *Effect of concentration:* The reaction was studied at different  $\text{H}_2\text{SO}_4$  concentrations, and the change in the overall rate constant  $k$  with concentration was examined, (figs. 4.7 and 4.8). From these plots the absolute values of the rate constants of adsorption ( $k_1$ ) and desorption ( $k_{-1}$ ) can then be determined in the following way. The relation  $k=(k_1[\text{H}^+] + k_{-1})$  predicts a linear rise of the overall rate constant  $k$  with concentration. But the values of  $k$  obtained in this experiment

at standard conditions of half coverage for concentrations of 4 and 6 mol dm<sup>-3</sup> are very similar. This may indicate that the concentration of the H<sup>+</sup> is no longer simply equal to the concentration of H<sub>2</sub>SO<sub>4</sub>. In this treatment, H<sub>2</sub>SO<sub>4</sub> was considered a 1:1 electrolyte since the range of concentrations used was relatively high ( 1 mol dm<sup>-3</sup> to 6 mol dm<sup>-3</sup>). The values of the concentrations of H<sup>+</sup> rather than concentrations of H<sub>2</sub>SO<sub>4</sub> were calculated by determining the values of the dissociation constants at each concentration and then multiplying by the corresponding molality. The values of the standard rate constants at peak potential  $k_1^\circ$  and  $k_{-1}^\circ$  were then determined using the following equations:

$k_1^\circ [1.0] + k_{-1}^\circ = 2.5 \times 10^{-6} \text{ mol cm}^{-2} \text{ s}^{-1}$  obtained in a separate measurement by measuring the decay time constant at the peak potential using 1 M sulfuric acid solution. Similarly, using other concentrations,

$$k_1^\circ [1.84] + k_{-1}^\circ = 3.47 \times 10^{-6} \text{ mol cm}^{-2} \text{ s}^{-1}$$

$$k_1^\circ [3.28] + k_{-1}^\circ = 4.69 \times 10^{-6} \text{ mol cm}^{-2} \text{ s}^{-1}$$

Solving pairs of equations at a time, yields the following absolute values of  $k_1^\circ$  and  $k_{-1}^\circ$ :

Concentrations used	$k_1^\circ/10^{-6}$	$k_1^\circ[\text{H}^+]/10^{-6}$	$k_{-1}^\circ/10^{-6}$
[H <sub>2</sub> SO <sub>4</sub> ]/ mol dm <sup>-3</sup>	(cm s <sup>-1</sup> )	(mol cm <sup>-2</sup> s <sup>-1</sup> )	(mol cm <sup>-2</sup> s <sup>-1</sup> )
1 and 2 M	1.13	1.13	1.4
1 and 4 M	0.95	1.75	1.57
2 and 4 M	0.84	2.75	1.91
Average	0.97	1.87	1.62

Theoretically, at standard conditions, the values of  $k_1^\circ[\text{H}^+]$  and  $k_{-1}^\circ$  should be nearly equal and the results indicate that the discrepancy is approximately 14% between the average values. Moreover, the values  $k_1^\circ$  and  $k_{-1}^\circ$  should be independent of concentration but our results show a percentage discrepancy of approximately 17% as the concentration range changes. The reason for this discrepancy, in both cases, may be attributed to activity effects which are significant at these high concentrations (i.e. from 1M to 4M). Note that the value of  $k^\circ$  of the H-sorption reaction on platinum in  $\text{HClO}_4$  solution (1.0 mol  $\text{dm}^{-3}$ ) is  $2.52 \times 10^{-6}$  mol  $\text{cm}^{-2}$   $\text{s}^{-1}$ . As expected, this is the same as for 1.0 mol  $\text{dm}^{-3}$   $\text{H}_2\text{SO}_4$  solution. Of course, more reliable results of  $k_1^\circ$  and  $k_{-1}^\circ$  could be obtained if more solutions with narrower intervals of  $[\text{H}^+]$  (say, 0.6, 1.0, 1.4, 1.8, 2.2, 2.6M) were prepared. In this way, a standard plot could be obtained showing the change of the overall rate constant with  $[\text{H}^+]$ .

5) *Symmetry Factor*: As a first approximation, the positions of the minima in the plots of  $k$  vs  $E$  at all concentrations and for both acids was constant. However, the minimum does not look symmetric in all graphs suggesting that  $\beta$  is not always equal to a half. Regression analysis was done on the plots of figures 4.7, 4.8, 4.9 and 4.10 utilizing the following equations,

$$\ln(k_1[H^+]) = \ln(k_1^0) - \frac{\beta F}{RT} (E - E^0)$$

*for*  $k_1[H^+] \gg k_{-1}$

$$\ln(k_{-1}) = \ln(k_1^0) + \frac{(1-\beta) F}{RT} (E - E^0)$$

*for*  $k_1[H^+] \ll k_{-1}$

(4.12)

A value of  $\beta$  of approximately 0.32 was obtained in this way.

In general, the rising edges of the minima exhibited a shoulder (shown as a dotted circle in figs. 4.7-4.10) which is not accounted for in eq. (4.5), where the increase of  $k$  with  $E$  is simply exponential. In fact, between 0.3 V and 0.33 V the change of  $k$  appears to be independent of  $E$ . The experimental results could be suggesting a transition in the chemisorption of the  $H^+$  from Pt(100) to Pt(111) facets [22] where the rates of chemisorption of  $H^+$  will become different.

#### 4.5) Conclusion:

The Sweep-Step technique has presented enough evidence to be a good candidate for studying surface reactions like the hydrogen sorption reaction. The technique showed to a good approximation that the hydrogen sorption reaction on polycrystalline platinum obeys the Langmuir isotherm, and the basic rate equation (eq. 4.1). On the other hand, the plots of  $k$  vs  $E$  (figs. 4.7-4.10) showed that the reverse rate (i.e. the rising edge of the minima) deviates from eq. 4.1. Further

experimental work should be done in order to decide whether the results can be better accounted for by including interaction parameters as in eq. 4.11.

Values of the standard overall rate constants were obtained at different concentrations of  $\text{H}_2\text{SO}_4$  solutions,  $2.50 \times 10^{-6} \text{ mol cm}^{-2} \text{ s}^{-1}$  at 1M,  $3.47 \times 10^{-6} \text{ mol cm}^{-2} \text{ s}^{-1}$  at 2M,  $4.69 \times 10^{-6} \text{ mol cm}^{-2} \text{ s}^{-1}$  at 4M and  $4.65 \times 10^{-6} \text{ mol cm}^{-2} \text{ s}^{-1}$  at 6M, and for the  $\text{HClO}_4$  solution ( $1.0 \text{ mol dm}^{-3}$ ),  $2.52 \times 10^{-6} \text{ mol cm}^{-2} \text{ s}^{-1}$ . Our results are lower than other values in the literature where three other techniques were used to determine  $k^\circ$ . Values of  $k$  in the literature corrected to standard conditions of 1.0 M  $[\text{H}^+]$  solution are ( $6 \times 10^{-6} \text{ mol cm}^{-2} \text{ s}^{-1}$  from experiments at  $[\text{H}^+] = 0.5 \text{ M}$  [40],  $4.5 \times 10^{-6} \text{ mol cm}^{-2} \text{ s}^{-1}$  from  $[\text{H}^+] = 1.0 \text{ M}$  [42],  $76.6 \times 10^{-6} \text{ mol cm}^{-2} \text{ s}^{-1}$  from  $[\text{H}^+] = 1.0 \text{ M}$  [41], and  $5.8 \times 10^{-6} \text{ mol cm}^{-2} \text{ s}^{-1}$  from  $[\text{H}^+] = 1.0 \text{ M}$  [46]). Apart from the result obtained by Durand [41], our results are close to other values in the literature [40,42,46]. The slight discrepancy may be attributed to different concentrations of  $\text{H}^+$  used, the technique applied, and estimating the roughness factor and hence the real surface area of the WE. For example, in our results the real area was estimated from the measured charges under the hydrogen desorption peaks, with a reference point of  $1\text{H}/\text{Pt} = 220 \mu\text{C cm}^{-2}$ . Other workers [46] had determined the Pt true surface area by integrating the faradaic capacitance-potential curves at low frequencies using the A.C. impedance method.

Our average absolute values of  $k_1^\circ$  and  $k_{-1}^\circ$  are  $0.97 \times 10^{-6}$  mol cm<sup>-2</sup> s<sup>-1</sup> and  $1.62 \times 10^{-6}$  mol cm<sup>-2</sup> s<sup>-1</sup> respectively. At a concentration of 4M and higher the overall rate constant stops rising as [H<sub>2</sub>SO<sub>4</sub>] is increased. The symmetry factor was found to be 0.32 at all concentrations of H<sub>2</sub>SO<sub>4</sub> solutions.

The Sweep-Step method has shown to be useful in quantitative and qualitative studies of surface reactions. In future work, this technique may be used to study surface reactions on single crystals, for example deriving a relationship which explains the behaviour of the hydrogen sorption reaction on Pt(111), or studying the iodine oxidation reaction on polycrystalline platinum and Pt(111).

The latter reaction is studied in the next section using the A.C. impedance technique.

## CHAPTER FIVE

Studying the Iodine Oxidation Surface Reaction  
on Polycrystalline Platinum5.1) Introduction:

The iodine oxidation reaction on polycrystalline platinum is one of those electrochemical reactions that is yet to be well understood. When a platinum electrode is immersed in a solution of aqueous iodide, an uncharged monolayer of iodine forms on the surface of the electrode [48,49,51,52]. The neutral chemisorbed iodine causes the surface to be positively charged [48]. In one paper[59], it was concluded that the iodine oxidation reaction is thermodynamically allowed at an electrode potential of approximately 0.5 V vs RHE, but it is activated at a higher potential of 1.2 V due to the onset of the formation of the oxide layer on the surface of platinum. However, halides are known to inhibit oxide formation [48,49], so the reason for the delayed activation should be sought instead in the kinetic stability of the iodine layer. On this basis, a reaction mechanism is proposed in this chapter where the reaction is initiated in the absence of adsorbed oxo-groups like PtO, PtOH, and Pt(H<sub>2</sub>O).

Since it is already known that the product of the iodine oxidation reaction on platinum is the iodate anion (IO<sub>3</sub><sup>-</sup>), and the oxidation process involves five electrons[48-50], then it is expected that iodine undergoes multiple charge transfer

steps which should be detectable by the a.c. impedance technique. This technique is capable of probing fast charge-transfer processes when operating at high frequencies (i.e. from 10 kHz to 50 kHz). If the technique detects separate charge transfer steps then a plot of impedance in the complex plane is expected to produce multiple semi-circles, each corresponding to one step as shown schematically in fig. 5.1. However, this ideal situation was not found in the present study.

The reaction was also analysed using Bode plots to obtain an equivalent circuit (fig. 5.11, section 5.4.5), which characterises the reaction mechanism. The change in the circuit parameters such as the faradaic resistance or double-layer capacitance with electrode potential was also examined. A reaction mechanism was devised for the iodine oxidation

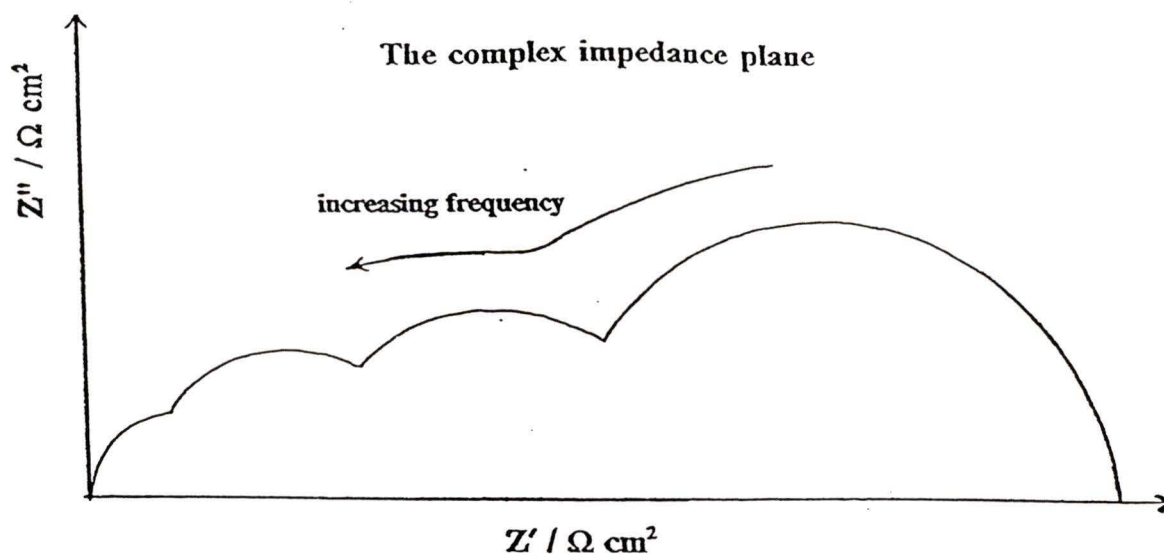


Figure 5.1 Nyquist plot of impedance of the expected reaction mechanism. Each arc indicates a detected charge transfer process.

reaction on platinum, where the reaction kinetics and current density equations were derived and simulated in order to compare with experimental results.

#### 5.2) Experimental Procedure:

The function generator FG was used to produce a d.c. voltage sweep at  $10 \text{ mV s}^{-1}$ . This sweep rate allows measurements at frequencies as low as 2 Hz without the system producing errors in magnitude and phase above 2% and 0.5 degrees respectively. The sweep signal was passed to the input of the potentiostat, and was also recorded by a 16 bit A/D converter (in the Lock-in-amplifier (LIA)). Through the latter the signal was digitized and transferred to the computer. Two sinusoidal voltage signals, of the same frequency and phase but not necessary of the same amplitude, come out of the oscillator in the LIA and were fed to two different inputs. One was passed to an input of the potentiostat where it was divided by a hundred, and the other signal was fed to the reference input of the LIA. The purpose of the latter was to detect the phase difference between the sinusoidal signal traversing the cell and the reference signal.

The real and imaginary parts of the current ( $I'$ ,  $I''$ ) and the voltage ( $V'$ ,  $V''$ ) were detected across the terminals of the Current Measuring Resistor ( $R_1$ ), (fig. 2.2), and the output of the voltage follower respectively. A double-throw switch was used to simplify changeover between the two separate

measurements (i.e. of  $V'$ ,  $V''$  and then of  $I'$ ,  $I''$ ). The phase angle of the reference channel was adjusted until  $V''$  was zero. In this way, the magnitude is equal to the real component  $V'$ . All voltages are quoted as root-mean-squared values ( $V_{\text{rms}}$ ). The  $V_{\text{rms}}$  for a sinusoid is the peak-to-peak voltage divided by  $2\sqrt{2}$ . It was found that at low frequencies the LIA filter time constants should be set to high values (300 ms to 1 s) and the  $R_1$  to high resistance (typical 60  $\Omega$ ) for better sensitivity. As the frequency was raised the time constant was made shorter and  $R_1$  was adjusted to lower values. Table 5.1 shows all the settings for this experiment.

During the experiment the LIA was controlled by a computer using the manufacturer's software (SR575).

The experiment was run using the following procedure. The electrolyte in the electrochemical cell was sulfuric acid (BDH ANALAR, dissolved in UHP water, concentration of 1.0 mol dm<sup>-3</sup>). The iodide solution was potassium iodide (BDH ACS 684 dissolved in UHP water to give 0.01 mol dm<sup>-3</sup>), which was placed in a separate bottle. The working electrode was set at a starting potential of 500mV using the FG. The electrode was then removed from the electrochemical cell, washed with (UHP) water, dipped in the iodide solution for few seconds, then removed and washed again with UHP water. Before placing the WE back into the electrochemical cell, the computer program was initiated in order to record the events before and after dipping the electrode in the sulfuric acid solution.

Table 5.1 :

## Instrumental settings for the a.c. impedance experiment

$V_{rms}$ (mV)	Frequency (Hz)	Load Resistance ( $\Omega$ )
7.43	2.0	60.0
7.55	5.0	60.0
7.51	10.0	60.0
7.43	20.0	60.0
7.47	40.0	60.0
7.37	60.0	60.0
7.46	80.0	60.0
7.44	100.1	60.0
7.47	200.0	30.0
7.47	300.0	30.0
7.55	400.0	20.0
7.55	500.0	10.0
7.51	600.0	10.0
7.51	800.0	10.0
7.59	1004.0	10.0
7.65	2000.0	10.0
8.12	5000.0	10.0
8.68	7500.0	10.0
8.46	10020.0	10.0
8.22	15000.0	10.0
7.78	20000.0	10.0
4.85	50000.0	10.0

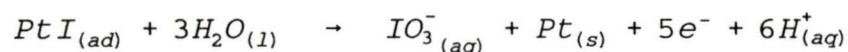
Then the FG was set to sweep the potential from 500 mV to 1600 mV and back down to 10 mV. During this sweep,  $I'$  and  $I''$  were being continually sampled and stored, ( $V_{rms}$  was measured in a separate sweep).

This completes one measurement run, but at least four complete cycles are needed to remove the iodine monolayer. In this experiment, six complete cycles were used for proper cleaning of the electrode before starting the experiment at a

different frequency. Data was collected over the frequency range 2 Hz to 50 kHz.

### 5.3) Results:

A d.c. cyclic voltammogram showing the anodic oxidation of iodine on platinum is shown in fig. 5.2. The peak at 1.4 V is attributed to the reaction.



The data of the current ( $I'$ ,  $I''$ ) and the  $V_{rms}$  voltage recorded at each electrode potential by the SR575 program were read by another software program. This program calculates the values of the real and imaginary parts of the admittance ( $Y'$ ,  $Y''$ / S cm<sup>-2</sup>, where  $Y=Y'+iY''$ ) and the impedance ( $Z'$ ,  $Z''$ / Ω cm<sup>2</sup> where  $Z=Z'-iZ''$ ). It also calculates the logarithm of the magnitude of the impedance  $\log(|Z|/\Omega\text{ cm}^2)$ , and the phase angle (degrees) in the complex impedance plane for all frequencies at a particular electrode potential. Sample plots of the real part of the admittance ( $Y'$ ) versus electrode potential for the iodine oxidation reaction are shown in figs. 5.3 and 5.4 for one sweep cycle. Compare these plots to the two admittance plots (fig. 5.5) of the oxidation of a Pt surface in pure sulfuric acid solution, ranging in frequency from 5 Hz to 500 Hz. Note how the trailing edge of the anodic peak (i.e. the peak showing iodine oxidation) rises as the frequency is increased, while this feature is absent in pure

## Cyclic Voltammogram of Iodine Oxidation on Platinum

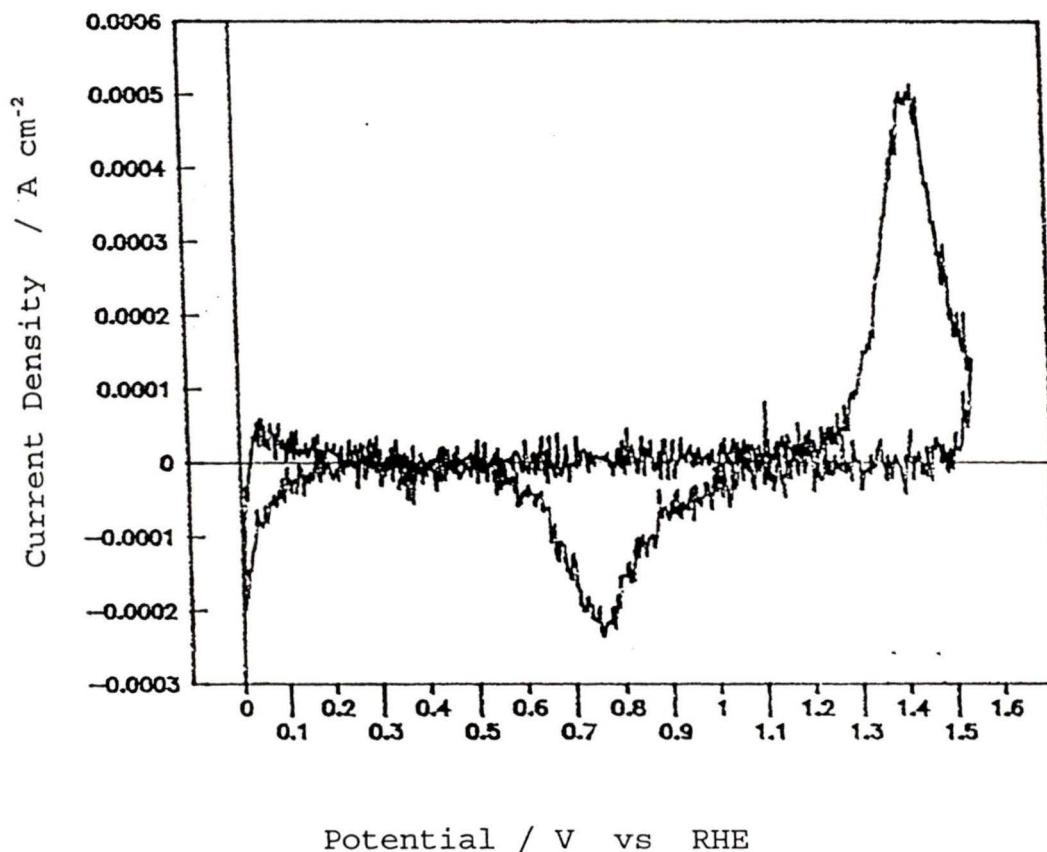


Figure 5.2 The d.c. cyclic voltammogram of iodine oxidation on platinum in  $\text{H}_2\text{SO}_4$  solution ( $1 \text{ mol dm}^{-3}$ ). Area of WE =  $0.6 \text{ cm}^2$ ,  $\nu = 5 \times 10^{-2} \text{ V s}^{-1}$ .

sulfuric acid, (fig. 5.5). Plots showing the change of  $\log|Z|$  and phase versus the logarithm of frequency ( $\log(f/\text{Hz})$ ) for potentials ranging from approximately 0.8 V up to 1.6 V are shown in figs. 5.6-5.8. Note the characteristic maximum yielded by the change in phase and the general drop in impedance (fig. 5.7) during the oxidation of the adsorbed iodine. Phase plots are also shown in fig. 5.9 as the potential sweeps down from 1.6 V to 0.707 V.

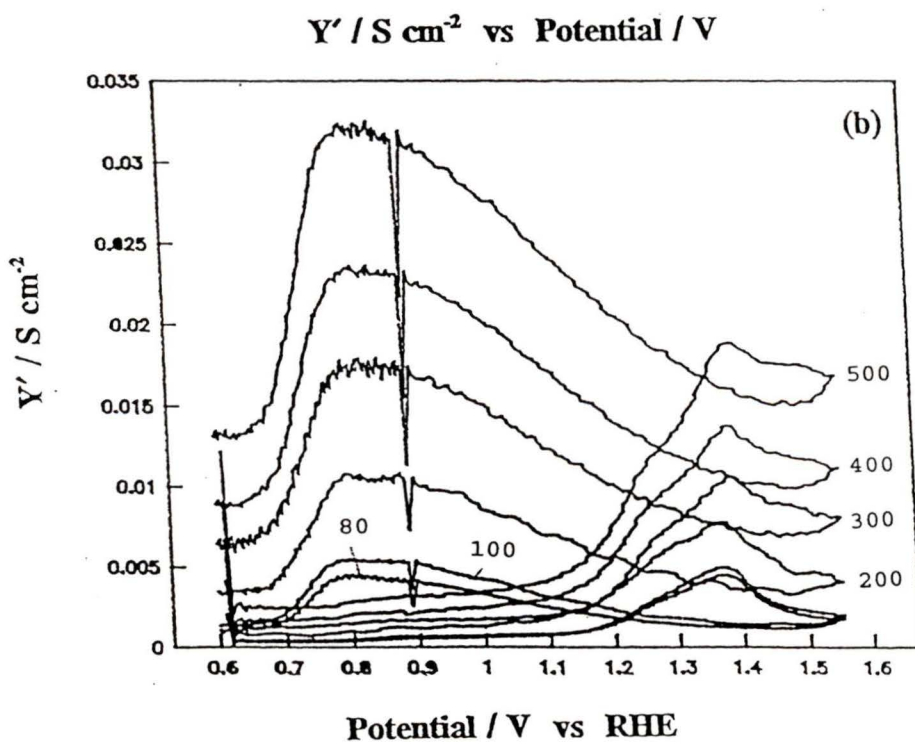
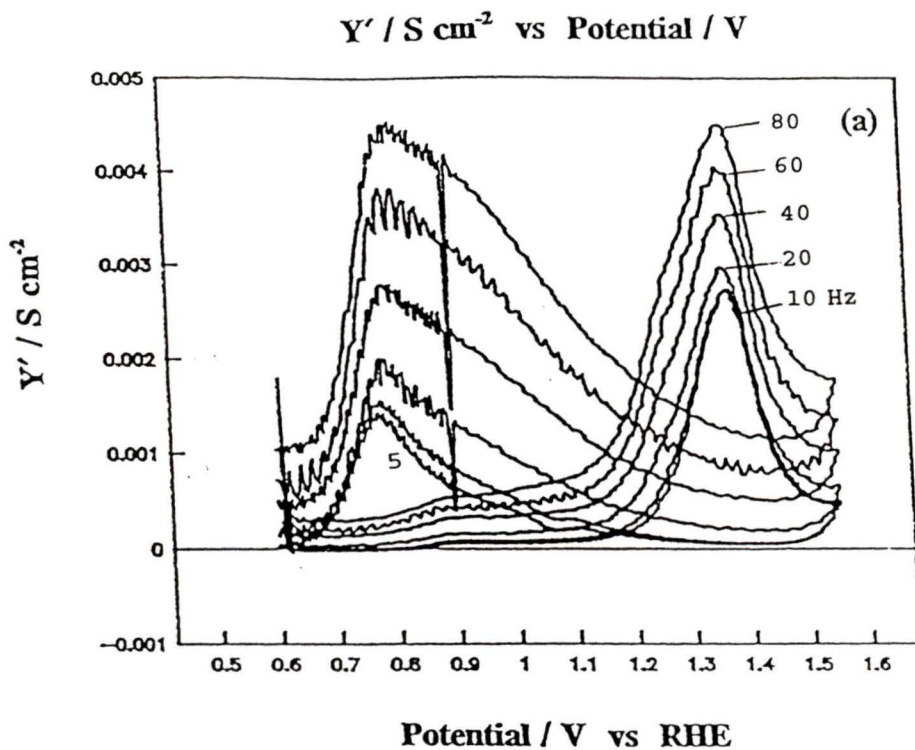


Figure 5.3 A.c. cyclic voltammograms of iodine oxidation on Pt in  $\text{H}_2\text{SO}_4$  solution ( $1 \text{ mol dm}^{-3}$ ). A plot of  $Y' / S \text{ cm}^{-2}$  vs  $E / \text{V}$  at frequencies (a) 5 to 80 Hz (b) 80 to 500 Hz.  $\nu = 10^{-2} \text{ V s}^{-1}$ .

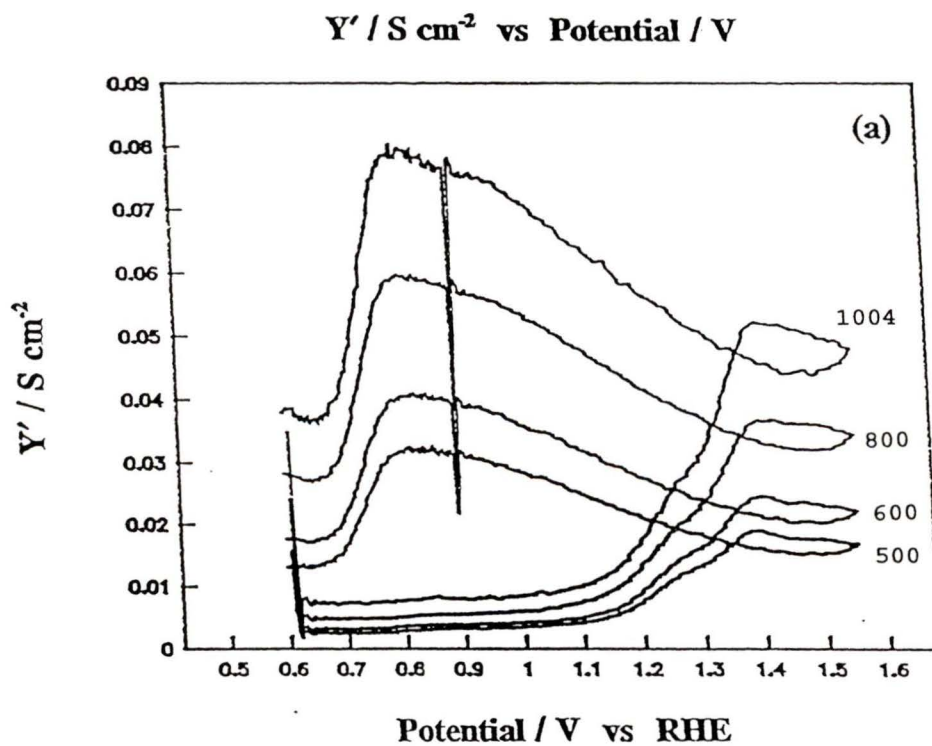
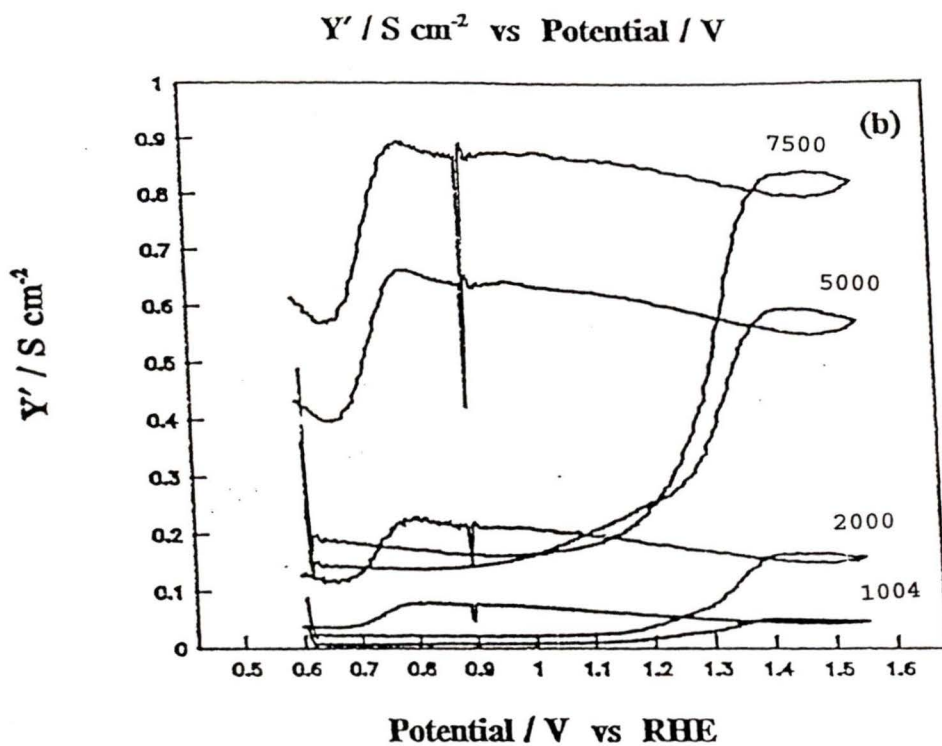


Figure 5.4 A.c. cyclic voltammograms of iodine oxidation on Pt in  $\text{H}_2\text{SO}_4$  solution ( $1 \text{ mol dm}^{-3}$ ). A plot of  $Y' / S \text{ cm}^{-2}$  vs  $E / \text{V}$  at frequencies (a) 500 to 1004 Hz (b) 1 to 7.5 kHz.  $\nu = 10^{-2} \text{ V s}^{-1}$ .

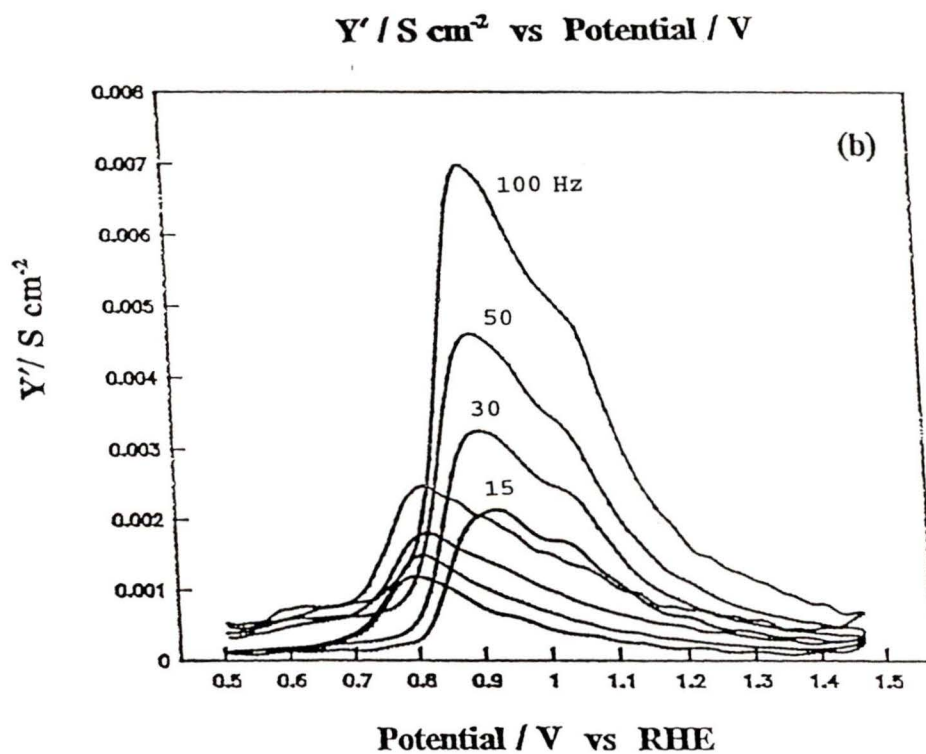
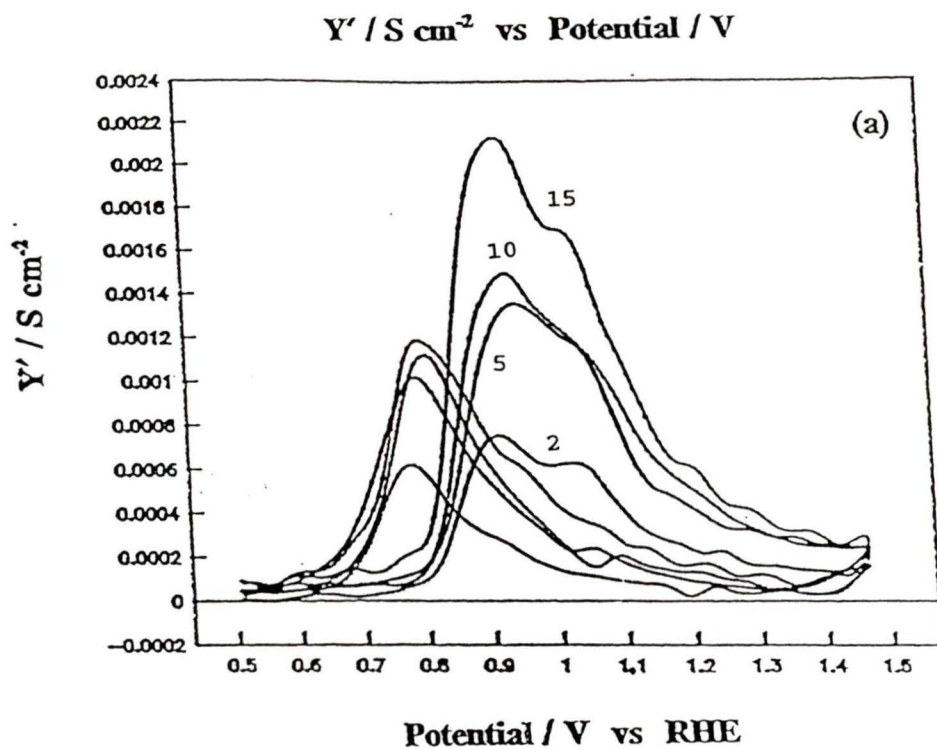


Figure 5.5 A.c. cyclic voltammograms of Pt oxidation in pure  $\text{H}_2\text{SO}_4$  solution ( $0.5 \text{ mol dm}^{-3}$ ). A plot of  $Y' / S \text{ cm}^{-2}$  vs  $E / \text{V}$  at frequencies (a) 2 to 15 Hz (b) 15 to 100 Hz.  $\nu = 10^{-2} \text{ V s}^{-1}$ .



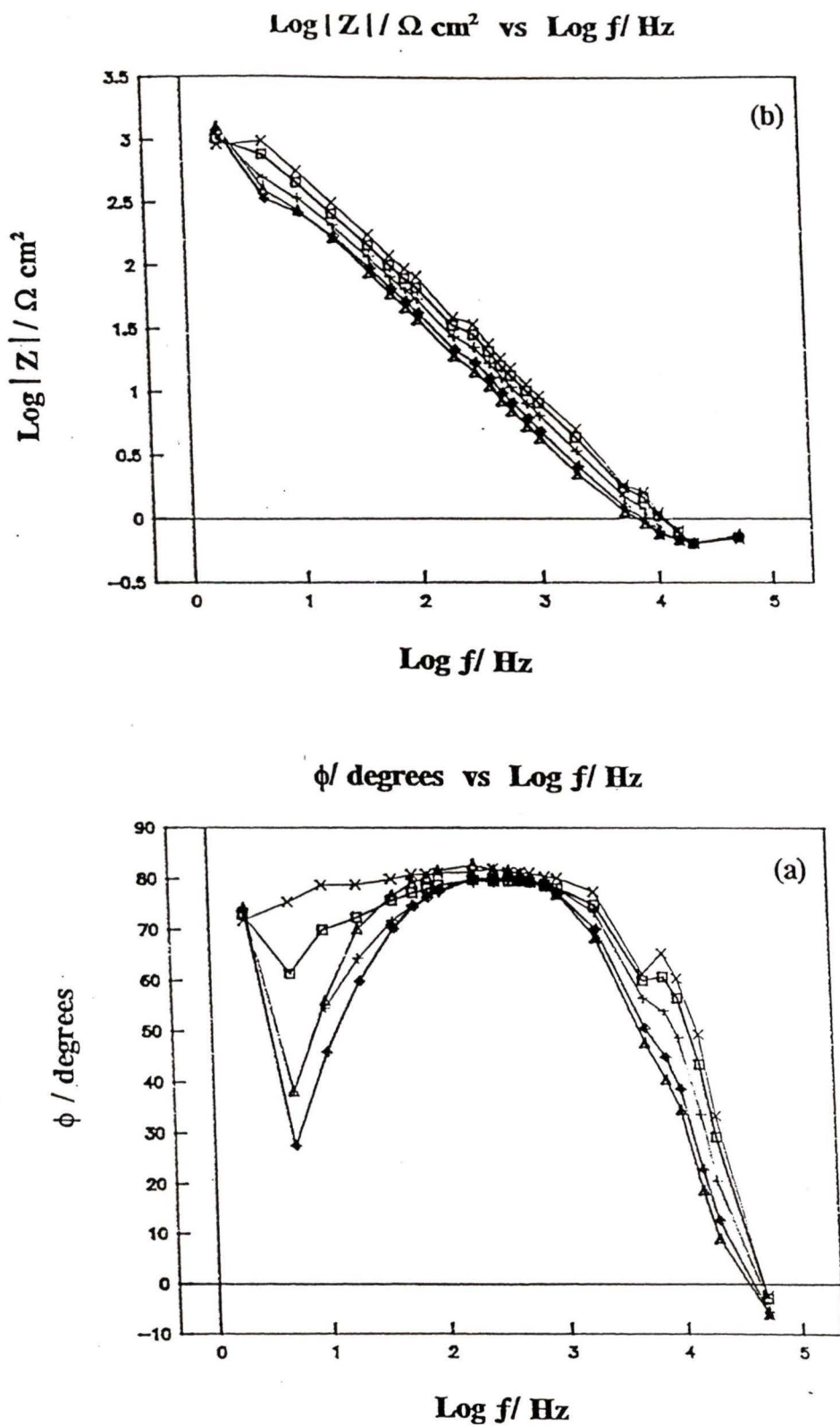


Figure 5.7 Bode plots of iodine oxidation on platinum. Graphs of (a) phase/ degrees and (b) magnitude/  $\Omega \text{ cm}^2$  vs  $\text{Log}(f / \text{Hz})$  at potentials of 1257  $\square$ , 1307  $+$ , 1357  $\diamond$ , 1407  $\Delta$ , and 1207  $\times$  mV.

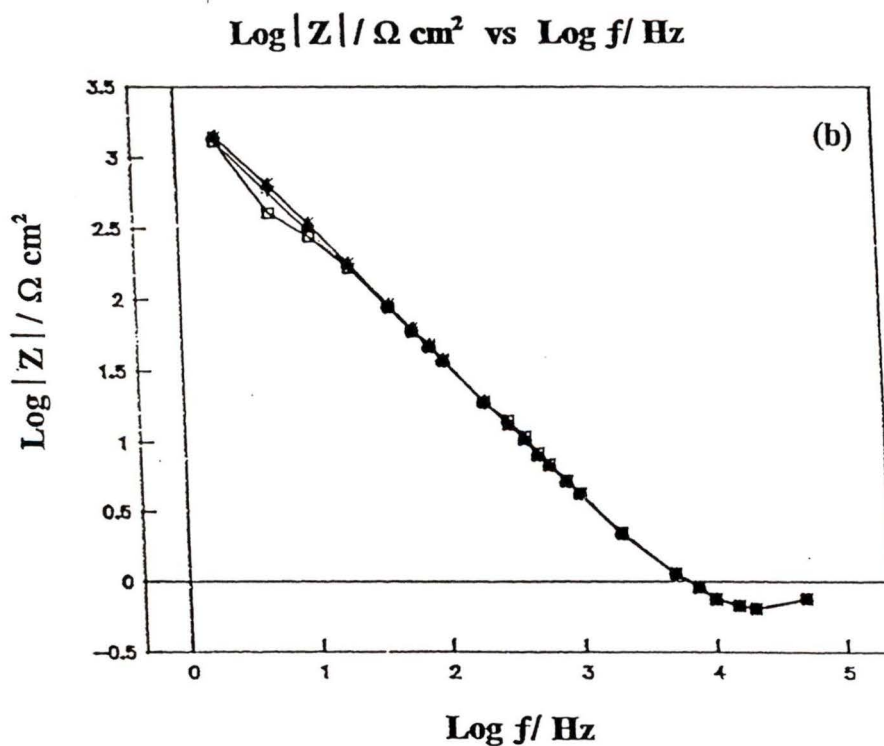
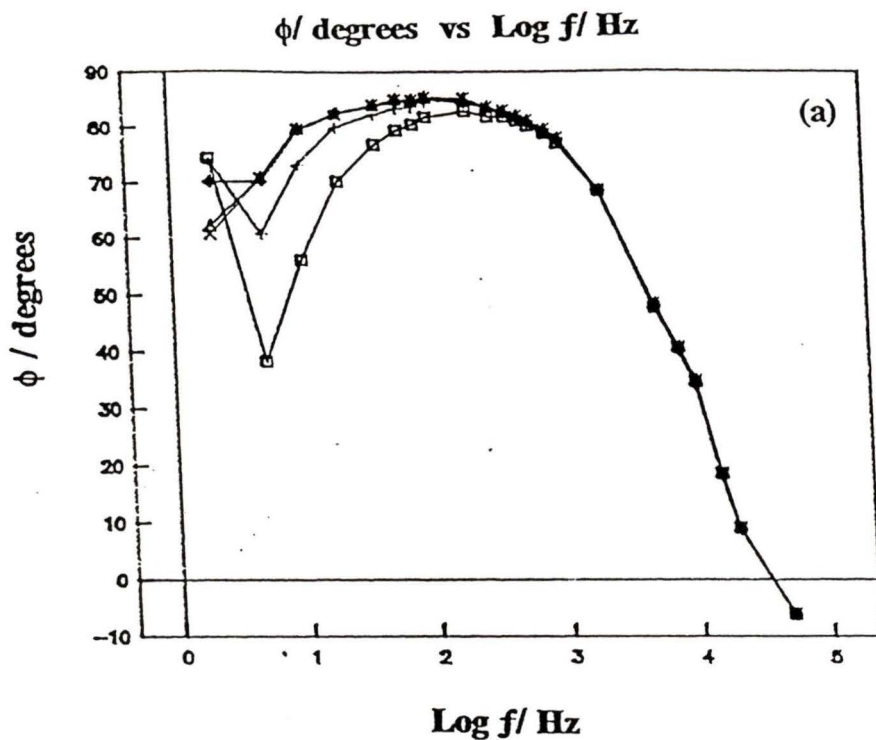


Figure 5.8 Bode plots as the iodine oxidation seized. Graphs of (a) phase/deg. and (b) magnitude/ $\Omega \text{ cm}^2$  vs  $\text{Log}(f / \text{Hz})$  at potentials of 1407  $\square$ , 1457  $+$ , 1507  $\diamond$ , 1557  $\Delta$ , and 1607  $\times$  mV.

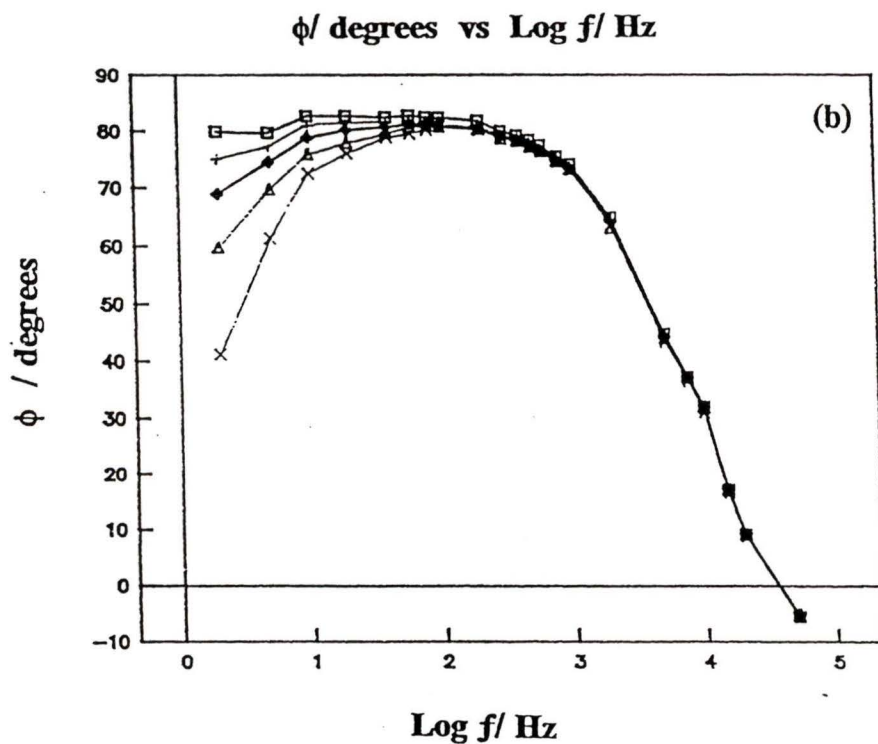
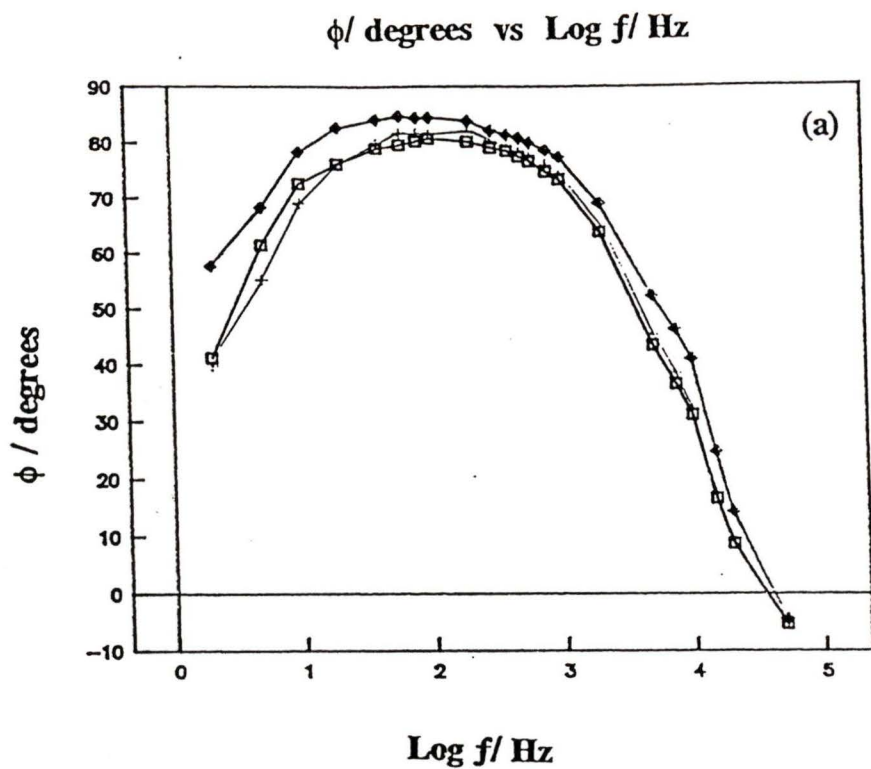


Figure 5.9 Bode plots during the reduction of PtO. Graphs of phase/ degrees vs  $\text{Log}(f / \text{Hz})$  at potentials of (a) 807  $\square$ , 757  $\diamond$ , 707  $\times$ , (b) 1007  $\square$ , 957  $+$ , 907  $\diamond$ , 857  $\Delta$ , and 807  $\times$  mV.

Plots of  $Z''$  versus  $Z'$  at two different potentials (1307 mV and 1357 mV) yielded single semi-circle (fig. 5.10) rather than multiple semi-circles, (fig. 5.1). This suggests that although the reaction might involve multiple steps, the technique is sensitive to species in only one of these steps, which is the rate determining step.

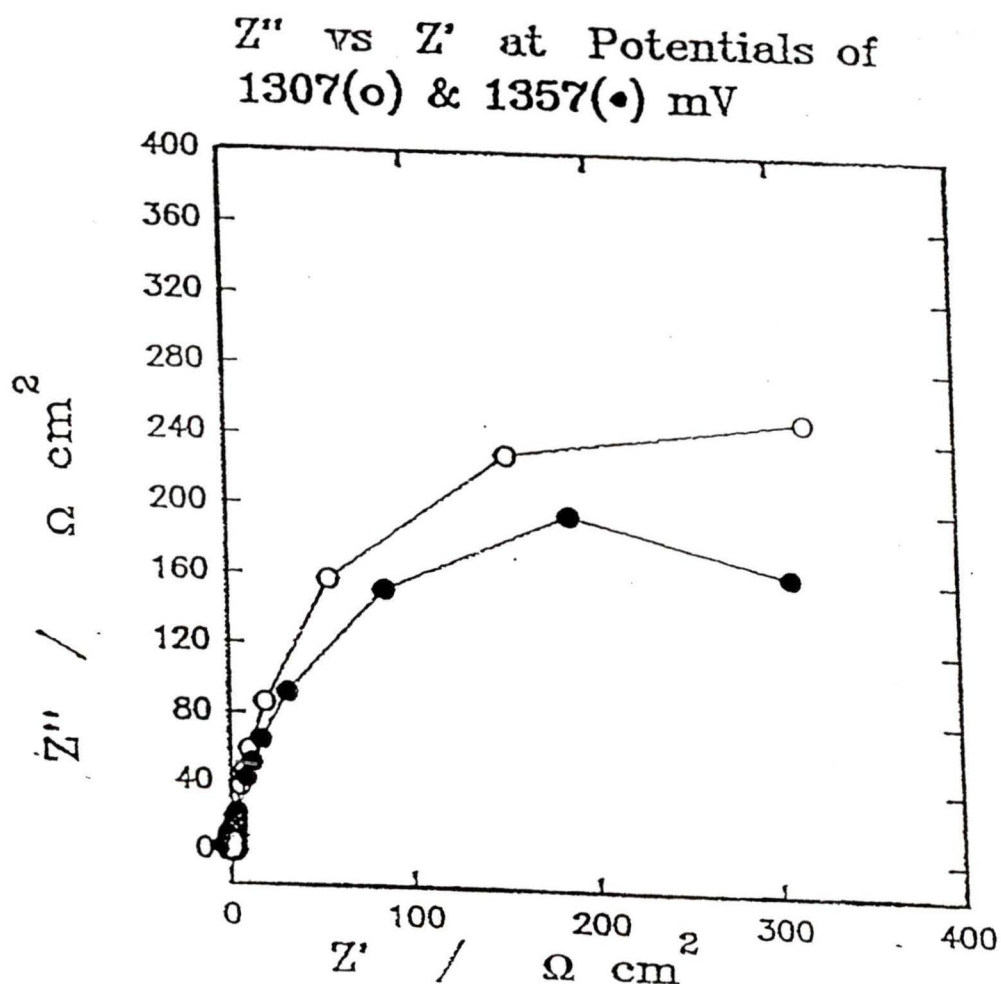


Figure 5.10 Nyquist plot of impedance of the observed reaction of iodine oxidation on platinum at potentials of 1307 ●, 1357 ○ mV. (Frequency range 5 to 50 kHz).

#### 5.4) Theory:

A theoretical background for calculating the magnitude of the impedance  $|Z|$ , the phase and other variables which characterises the iodine oxidation reaction is provided. Then a thorough analysis of the reaction mechanism and kinetics is presented, including predicting the form of the d.c. and a.c. cyclic voltammograms.

##### 5.4.1) Derivation of the magnitude of the impedance $|Z|$ , and the phase $\phi$ from experimental results:

In order to derive the relevant circuit which describes this reaction the values of the magnitude of the impedance  $|Z|$  and the phase shift  $\phi$  were calculated from the experimental data. At each frequency, the values of  $I'$ ,  $I''$  and  $V'$  ( $V'' = 0$ ) are determined as described in the experimental section (5.2). First we can calculate:

$$Y' = \frac{I'}{V'} \quad , \quad Y'' = \frac{I''}{V'} \quad (5.1)$$

$$\therefore Y = \frac{I' + iI''}{V'} \quad \text{for } V'' = 0$$

where  $Y$  is the admittance of the cell.

Therefore, the magnitude of the impedance is:

$$|Z| = \sqrt{Z'^2 + Z''^2} \quad \text{where } Z' = \frac{Y'}{Y'^2 + Y''^2} \quad (5.2)$$

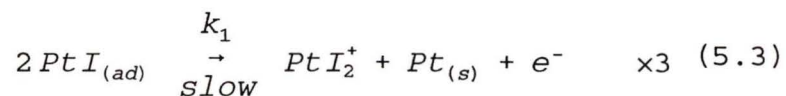
$$Z'' = \frac{Y''}{Y'^2 + Y''^2} \quad , \quad \phi = \arctan\left(\frac{Z''}{Z'}\right)$$

By plotting  $\log(|Z|)$  vs  $\log(f/\text{Hz})$  and  $\phi$  vs  $\log(f/\text{Hz})$  at different potentials we can characterise the circuit evolving as the potential is swept and the reaction progresses (For example, a typical layout of such a circuit is shown in fig. 5.13(b), section 5.4.5). Up to this point we know that there is a faradaic impedance characterising the faradaic reaction, but we cannot characterise the network of resistors, capacitors, and inductors involved in it.

#### 5.4.2) Devising a reaction mechanism for the iodine oxidation reaction:

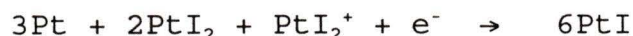
In section (5.3) the impedance results yielded a graph of only one semi-circle (fig. 5.10) at potentials of 1307 mV and 1357 mV. This suggests that the oxidation process is either a one step mechanism or multiple steps controlled by one rate determining step (rds).

We may consider that the whole reaction is comprised of a sequence of steps and one of these is the rate determining step while the rest are relatively fast. The following sequence of steps are proposed to describe the reaction mechanism.

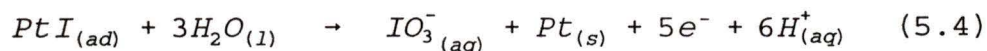


and this is the rate determining step of the reaction. It

occurs three times for every  $\text{IO}_3^-$  produced, as indicated by the  $\times 3$  symbol. The rest were considered relatively fast processes.



These sum to



which is the net ionic equation of these reactions. There is a platinum site left uncovered which is readily oxidised to PtO:



During the oxidation process the surface of platinum is occupied by the covered PtI, PtO,  $[\text{Pt-I-O}]^*$ , and  $\text{PtI}_2$  sites, as well as the uncovered platinum sites (Pt).

As formulated above the formation of the  $[\text{Pt-I-O}_3]^*$  complex occurs in a single step involving simultaneous formation of three I-O bonds. Statistically, this seems unlikely and there is some likelihood that instead its evolution may involve parent complexes like  $\text{Pt-IO}^*$  and  $\text{Pt-IO}_2^*$ . The hypothetical reaction mechanism then proceeds as follows.



The corresponding physical changes are sketched in fig. 5.11.

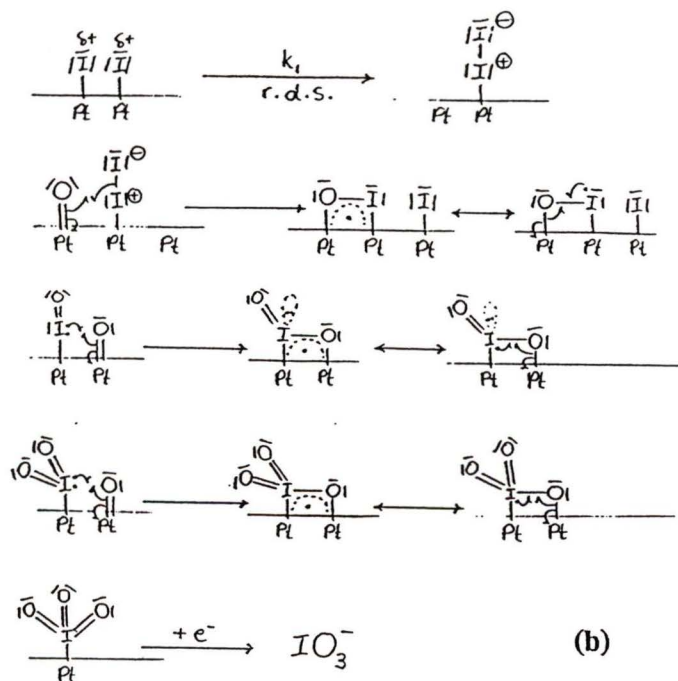
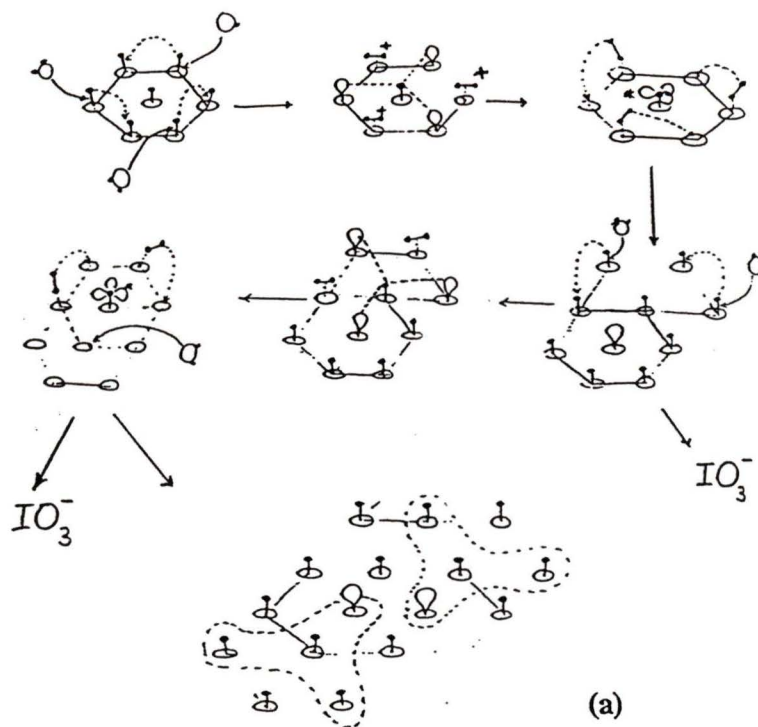


Figure 5.11 Schematic of the likely mechanism of the iodine oxidation reaction (a) case of one complex (b) formation of many complexes (section 5.4.2).

### 5.4.3 ) Reaction Kinetics:

Having described the reaction mechanism, we can proceed to derive the overall rate equation. The rate of the rate determining step (eq. 5.3) is:

$$-\Gamma_m \frac{d\theta_1}{dt} = r_{(rds)} = k_1' \theta_1^2 [H_2O] = k_1 \theta_1^2 \quad (5.5)$$

where  $\theta_1$  is the fractional coverage by iodine adatoms (i.e. PtI sites),  $\Gamma_m$  is the surface concentration of the iodine adatoms and  $k_1$  is the rate constant of the rate determining step of the overall reaction. Eq. 5.5 is the differential equation to be solved. We then need to relate the change of  $\theta_1$  as a function of potential to the experimental current density.

From the net ionic equation we can write the following relations:

$$j = -\sigma_m \frac{d\theta_1}{dt} \quad (5.6)$$

where  $j$  is the current density due to iodine oxidation and  $\sigma_m$  is the charge density characterising the oxidation of a full monolayer of iodine adatoms on the surface of platinum. The value of  $\sigma_m$  can be determined experimentally by integrating the anodic oxidation peak in the cyclic voltammogram, (fig. 5.2), to find the total amount of charge liberated by the reaction and then divided by the surface area

of the WE.  $F$  is the Faraday constant.

$$\text{but } \sigma_m = 5F\Gamma_m \quad (5.7)$$

Combining eqs. 5.5, 5.6 and 5.7:

$$\frac{j}{F} = 5k_1\theta_1^2 \quad (5.8)$$

and the differential equation:

$$-\frac{\sigma_m}{5F} \frac{d\theta_1}{dt} = k_1\theta_1^2 \quad (5.9)$$

#### 5.4.4) Simulating the d.c. cyclic voltammogram (fig. 5.2):

If eq. 5.5 faithfully describes the oxidation reaction of adsorbed iodine on platinum then we should obtain an expression for the current density which agrees with the experimental cyclic voltammogram, (fig. 5.2). An equation for the current density as a function of potential or time (the two are simply related by the sweep rate,  $t=E/\nu$ ) was obtained after solving the differential equation eq. 5.9.

In eq. 5.9, the rate constant  $k_1$  is potential dependent in the usual way for electron-transfer steps:

$$-\frac{\sigma_m}{5F} \frac{d\theta_1}{dt} = k_1\theta_1^2$$

$$\text{where, } k_1 = k_1^0 \exp\left[\frac{\beta F}{RT} ((E_s + \nu t) - E^0)\right]$$

where,  $k_1$  ( $\text{mol cm}^{-2} \text{ s}^{-1}$ ) is the forward rate constant of the rds of the oxidation of adsorbed iodine. Let

$k_s = k_1^\circ \exp[\beta F(E_s - E^\circ)/RT]$  where  $k_1^\circ$  is the rate constant at standard potential  $E^\circ$ .  $E^\circ$  is difficult to assign experimentally and only the value of  $k_s$  is determined from the simulation.  $\nu$  is the sweep rate ( $V s^{-1}$ ) and  $E_s$  is the starting potential of the sweep.

In this analysis, the value of the rate constant at peak potential (i.e. at 1.42 V in the CV of fig. 5.2) is the kinetic parameter of interest and is calculated from  $k_s$ :

$$k_1^p = k_s \exp\left[\frac{\beta F}{RT}(E_p - E_s)\right] \quad (5.10)$$

First, the change of coverage  $\theta_1$  with potential was examined by rearranging eq. (5.9) and integrating taking  $\theta_1=1$  at  $t=0$ ,

$$\theta_1 = \frac{1}{5 \left( \frac{Fk_s}{\sigma_m a} (\exp[at] - 1) + 1 \right)} \quad (5.11)$$

$$\text{where, } a = \frac{\beta F \nu}{RT}$$

Differentiating eq. (5.11) with respect to time gives an expression for  $d\theta_1/dt$ , which may then be substituted for  $d\theta_1/dt$  in eq. (5.6):

$$\frac{d\theta_1}{dt} = \frac{-\sigma_m F}{5} \frac{k_s \exp[at]}{\left( \frac{Fk_s}{a} (\exp[at] - 1) + \frac{\sigma_m}{5} \right)^2} \quad (5.12)$$

$$\therefore j = \frac{\sigma_m^2 F}{5} \frac{k_s \exp[at]}{\left( \frac{Fk_s}{a} (\exp[at] - 1) + \frac{\sigma_m}{5} \right)^2} \quad (5.13)$$

The following values are appropriate to our experimental conditions.

$$\nu = 50 \text{ mV s}^{-1}$$

$$T = 25 \pm 1 \text{ } ^\circ\text{C}$$

$$E_s = 500 \text{ mV}$$

$$A_v = 0.059 \pm 0.003 \text{ V s}$$

$$\text{Area of the WE} = 0.6 \text{ cm}^2$$

In this simulation, the value of  $(j/\sigma; \text{s}^{-1})$  which is equal to  $(V/A_v; \text{s}^{-1})$  was plotted against time(s).  $V$  is the measured CV signal in volts, and  $A_v$  is the integral area under the peak. The parameters of  $k_s$  and  $\beta$  were then adjusted to give the best agreement between experimental and theoretical results, (fig. 5.12), The following values of  $\beta$  and  $k_s$  were optimal:

$$\beta = 0.63$$

$$k_s = 5 \times 10^{-11} \text{ s}^{-1}$$

Using the standard value of  $\Gamma_m$  in the literature ( $1.42 \times 10^{-9} \text{ mol cm}^{-2}$ ) we can obtain the value of the rate constant at the starting potential in  $\text{mol cm}^{-2} \text{ s}^{-1}$  as:

$$k_s' = 7.1 \times 10^{-20} \text{ mol cm}^{-2} \text{ s}^{-1}$$

Although we do not know  $E^\circ$ , and hence can not calculate  $k_1^\circ$ , we give the rate constant at the peak maximum. Using eq. 5.11 the value of the rate constant at peak maximum is:

$$k_1^p = (5.8 \pm 1) \times 10^{-10} \text{ mol cm}^{-2} \text{ s}^{-1}$$

A value of  $\beta$  less than one proves that the first charge transfer step, which involves one electron, is the rate determining step [84].

$j/\sigma / \text{s}^{-1}$  vs Time / s  
Observed and calculated data

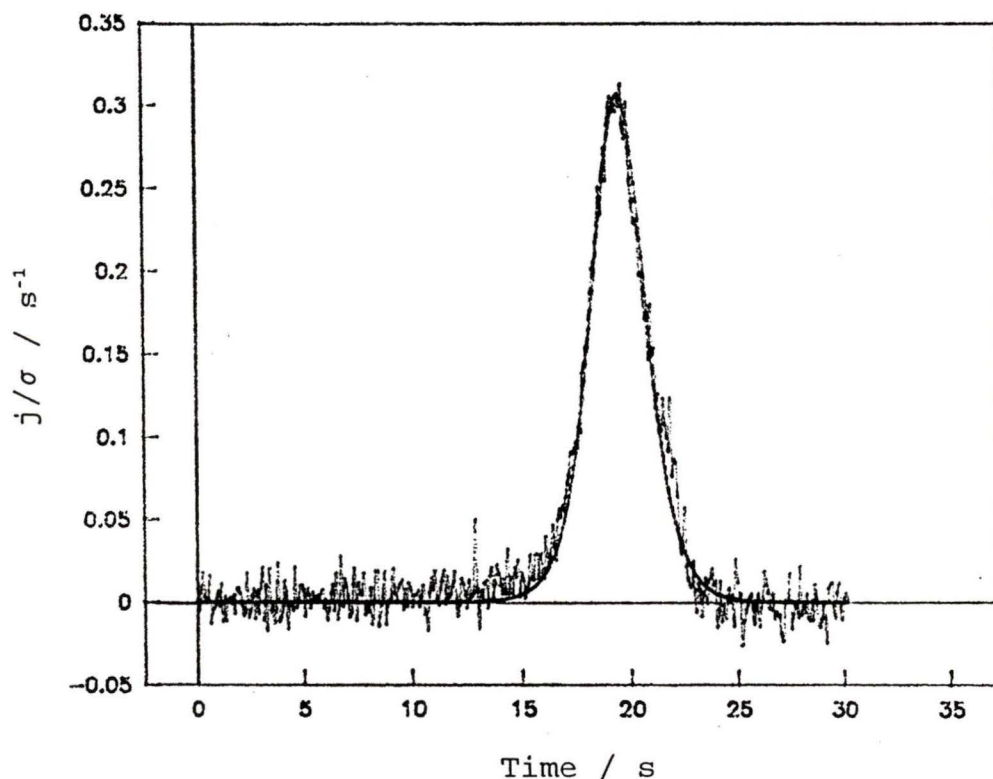


Figure 5.12 The d.c. cyclic voltammogram of iodine oxidation on platinum in  $\text{H}_2\text{SO}_4$  solution ( $1 \text{ mol dm}^{-3}$ ) for the observed and calculated results (the calculated  $j/\sigma$  is the smooth line).

#### 5.4.5) A.c. impedance analysis:

In a.c. impedance analysis, the d.c. component of the input voltage signal provides the desired electrode potential at which the surface reaction is studied, and the a.c. component perturbs the surface reaction. Both components generate a total current  $j$  characteristic of the surface process. The response of the faradaic current  $j$  to a sinusoidal potential perturbation for a process that involves  $n$  state coverages  $(\theta_1, \theta_2, \dots, \theta_n)$  at an electrode potential  $E$ ,

where  $j = f(E, \theta_1, \theta_2, \dots, \theta_n)$  is expressed as:

$$\delta j = \left( \frac{\partial j}{\partial E} \right)_{\theta_1, \dots, \theta_i} \delta E + \sum_{i=1}^n \left( \frac{\partial j}{\partial \theta_i} \right)_{\theta_j, E} \delta \theta_i \quad (5.14)$$

where,

$$\delta E = \Delta E \exp[i\omega t] \quad \text{and} \quad \delta \theta_i = \Delta \theta_i \exp[i\omega t]$$

where  $\delta \theta_i$  is the finite change in coverage  $\theta_i$  due to a sinusoidal signal  $\delta E$ , i.e. the departure from the d.c. value. Dividing both sides of the equation by  $\delta E$  the faradaic admittance  $Y_f$  is obtained as  $Y_f = (\delta j / \delta E)$ . In the d.c. cyclic voltammogram (fig. 5.2) the peak current density observed, between 1.2 V and 1.6 V, is due to non-steady-state conditions. However, we may assume that the surface process is under quasi-steady state conditions and there is no contribution to  $\delta j$  from non steady state processes. This is because the changes in coverage and rate with d.c. potential are much slower than the a.c. changes.

In this a.c. impedance experiment the a.c. cyclic voltammogram was obtained as a change of total admittance ( $Y_T$ ) against potential. The first step in this calculation is to derive an expression for the faradaic admittance  $Y_f$ . According to eq. 5.6 the change in  $Y_f$  is affected by only one state of coverage  $\theta_1$ . Since the current density  $j$  is a function of electrode potential  $E$  and coverage ( $\theta_1$ ) then the partial derivative of  $j$  is:

$$\delta j = \left( \frac{\partial j}{\partial E} \right)_{\theta_1} \delta E + \left( \frac{\partial j}{\partial \theta_1} \right)_E \delta \theta_1 \quad (5.15)$$

where  $\delta \theta_1$  is the finite change in coverage  $\theta_1$  due to a sinusoidal signal  $\delta E$ . Here  $\delta E$  is a sinusoidal function with magnitude  $\Delta E$  and angular frequency  $\omega$ , i.e.  $\delta E = \Delta E \exp(i\omega t)$ . Dividing both sides of eq.(5.15) by  $\delta E$  we get an expression for  $Y_f$ :

$$\Rightarrow \tilde{Y}_f = \frac{\delta j}{\delta E} = \left( \frac{\partial j}{\partial E} \right)_{\theta_1} + \left( \frac{\partial j}{\partial \theta_1} \right)_E \frac{\delta \theta_1}{\delta E} \quad (5.16)$$

However, referring back to section 5.4.3 and utilizing eq. 5.9 for the d.c. current density  $j$ :

$$j = 5 F k_1 \theta_1^2 = -\sigma_m \frac{d\theta_1}{dt}$$

$$\Rightarrow j = 5 F k_1^0 \exp\left(\frac{\beta F}{RT} E\right) \exp\left(-\frac{\beta F}{RT} E^0\right) \theta_1^2 \quad (5.17)$$

$$\Rightarrow j = 5 F k^0 \exp[bE] \theta_1^2 = -\sigma_m \frac{d\theta_1}{dt} \quad (5.18)$$

where  $k^0 = k_1^0 \exp[-\beta F E^0 / RT]$  and  $b = \beta F / RT$

and  $k_1 = k^0 \exp[\beta F E / RT]$

The partial differentials of  $j$  with respect to  $E$  and  $\theta_1$  evaluated at steady-state d.c. conditions are  $(\partial j / \partial E)_{\theta_1}$  and  $(\partial j / \partial \theta_1)_E$ , where,

$$\left( \frac{\partial j}{\partial E} \right)_{\theta_1} = 5 b F k^0 \exp(bE) \cdot \theta_1^2 \quad (5.19)$$

$$\left(\frac{\partial j}{\partial \theta_1}\right)_E = 10 F k^o \exp(bE) \cdot \theta_1 \quad (5.20)$$

which upon substitution in eq. 5.15 and utilizing eq. 5.18, gives:

$$\begin{aligned} \delta j &= 5 b F k^o \exp(bE) \cdot \theta_1^2 \delta E + 10 F k^o \exp(bE) \cdot \theta_1 \delta \theta_1 \\ &= -\sigma_m \delta \frac{d\theta_1}{dt} \end{aligned} \quad (5.21)$$

The next task is to evaluate  $\delta(d\theta_1/dt)$ . For a sinusoidal perturbation the coverage changes with the sinusoidal signal such that:

$$\delta \theta_1 = \Delta \theta_1 \exp[i \omega t] \quad (5.22)$$

$$\Rightarrow \frac{d(\delta \theta_1)}{dt} = i \omega \delta \theta_1 \quad (5.23)$$

$$\text{Here, } \frac{d(\delta \theta_1)}{dt} = \delta \frac{d\theta_1}{dt} \quad (5.24)$$

Substituting for  $\delta(d\theta_1/dt)$  in eq. 5.21, and rearranging,

$$\frac{\delta \theta_1}{\delta E} = \frac{-5 b F k^o \exp[bE] \theta_1^2}{\sigma_m i \omega + 10 F k^o \exp[bE] \theta_1} \quad (5.25)$$

Substituting for  $(\partial j / \partial E)_{\theta_1}$  and  $(\partial j / \partial \theta_1)_E$  and  $\delta \theta_1 / \delta E$  in eq. 5.16, and rearranging, we obtain  $Y_f$  as a function of frequency,

$$\tilde{Y}_f = 5 b F k^o \exp[bE] \theta_1^2 \left[ 1 - \frac{1}{\frac{\sigma_m}{10 F k^o \exp[bE] \theta_1} + 1} i \omega \right] \quad (5.26)$$

From eq. (5.26) the equivalent circuit which corresponds to the iodine oxidation reaction on platinum can be deduced. If eq. (5.26) is put into standard form and simplified, then the faradaic admittance can be written as:

$$\tilde{Y}_f = \frac{5bFk_1\theta_1^2\omega^2\sigma_m^2}{W} + i\omega\left(\frac{50bF^2k_1^2\theta_1^3\sigma_m}{W}\right) \quad (5.27)$$

where,  $W = \omega^2\sigma_m^2 + (10Fk_1\theta_1)^2$

and,  $k_1 = k^0\exp(bE)$

Eq. 5.27 may be recast in a form which gives the faradaic admittance as:

$$\tilde{Y}_f = \frac{1}{R_f + \frac{1}{i\omega C_f}} \quad (5.28)$$

$$\text{where } C_f = \frac{1}{2}b\theta_1\sigma_m \quad (5.29)$$

$$\text{and } R_f = \frac{1}{5bFk_1\theta_1^2} \quad (5.30)$$

Here  $C_f$  is the faradaic capacitance and  $R_f$  is the faradaic resistance, and therefore the faradaic reaction is a combination of a capacitor and a resistor in series. The values of  $C_f$  and  $R_f$  can be determined by using the values of  $k_1^p$  and  $\beta$  obtained in section 5.4.5. The value of  $C_f$ , at half coverage, was calculated to be  $4201 \mu\text{F cm}^{-2}$  and the contribution of the  $1/\omega C_f$  part of  $Y_f$  to the overall faradaic admittance at 2Hz is  $18.9 \Omega \text{ cm}^{-2}$ . The corresponding value of  $R_f$  at half coverage was approximately  $588 \pm 100 \Omega \text{ cm}^{-2}$ . This

shows that the contribution of  $C_f$  to the overall process is insignificant at the range of frequencies we are working with (i.e. 2Hz to 50 kHz), and the dominant contribution comes from the faradaic resistance suggesting that the reaction is largely resistive.

The equation for  $R_f$  eq.(5.30) clearly shows that as the potential is increased  $k_1$  or  $k^o$  increases while  $\theta_1$  decreases and therefore the resultant change of  $R_f$  with potential should yield a minimum. Well, this is what the suggested reaction mechanism predicts for  $R_f$  but will the experimental results obtained in the a.c. impedance technique show the same behaviour of  $R_f$ ?

The answer to this problem is analysed using the circuit shown in (fig. 5.13). The circuit contains all the significant electrochemical parameters for the WE-solution interface. It should be noted that no faradaic capacitance is included in this circuit since it was concluded that it is insignificant.

The values of  $R_f$  at each potential can be determined from the calculated values of the admittance( $Y$ ) and impedance( $Z$ ) obtained from the experimental results section(5.3). In the next section the values of  $R_f$  and the double-layer capacitance at the WE ( $C_d$ ) are calculated.

#### Calculating the values of $R_f$ and $C_d$ :

To simplify the calculation, the double-layer capacitance was considered to be a pure capacitor but such an assumption

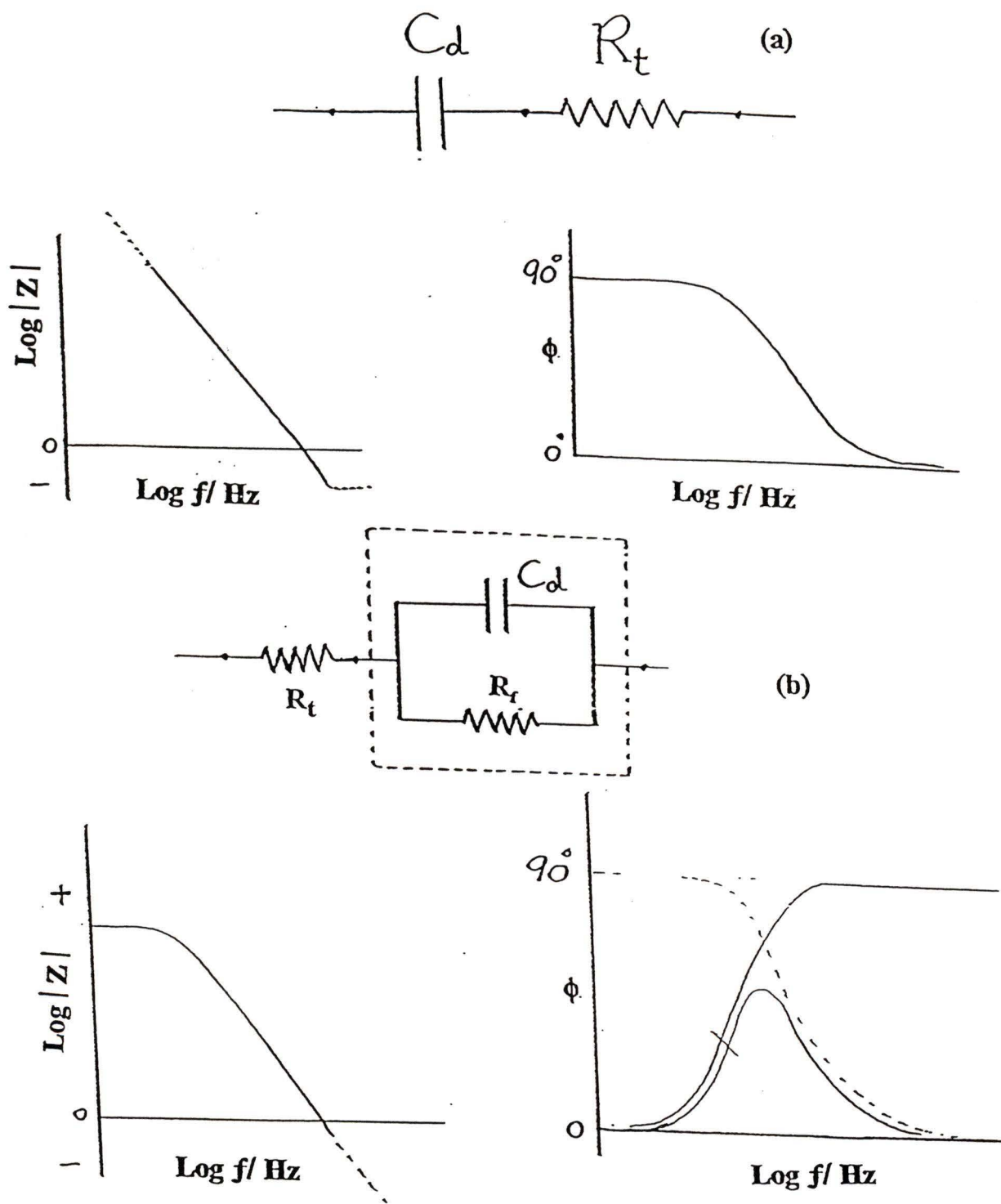


Figure 5.13 Equivalent circuit showing the electrochemical parameters for (a) the adsorbed iodine monolayer and (b) the iodine oxidation reaction on platinum.

did not give a good representation of the experimental data. Instead, the double-layer capacitance was considered to be a constant phase element (CPE). The CPE is characterised by a coefficient  $\varphi$  where  $\varphi$  has a particular value for a particular potential. This is illustrated mathematically as shown below. By definition for a constant phase element, let:

$$Z = \frac{1}{(i \omega C_d)^\varphi} = \frac{1}{\left(G \exp\left[i \frac{\pi}{2}\right]\right)^\varphi} \quad (5.31)$$

where  $G^{-\varphi}$ , and  $\pi^\varphi/2$  are the magnitude and the phase of the impedance respectively. According to the above equation:

$$G^\varphi = (\omega C_d)^\varphi \quad (5.32)$$

For a parallel combination of  $C_d$  and  $R_f$ , (dotted box in fig. 5.13):

$$Y = (i \omega C_d)^\varphi + \frac{1}{R_f} \quad (5.33)$$

$$\Rightarrow Y = \left(\omega C_d \exp\left[\frac{i \pi}{2}\right]\right)^\varphi + \frac{1}{R_f}$$

$$\Rightarrow Y = (\omega C_d)^\varphi \cos\left(\frac{\pi \varphi}{2}\right) + \frac{1}{R_f} + i (\omega C_d)^\varphi \sin\left(\frac{\pi \varphi}{2}\right) \quad (5.34)$$

By analogy and considering the circuit of (fig. 5.13), the solution resistance  $R_t$  should be subtracted out from the experimentally determined  $Z'$  to get the parallel combination, and we can write:

$$Y_{\varphi}'' = \frac{Z''}{|Z|^2} = (\omega C_d)^{\varphi} \sin\left(\frac{\pi\varphi}{2}\right) \quad (5.35)$$

$$Y_{\varphi}' = \frac{Z' - R_t}{|Z|^2} = (\omega C_d)^{\varphi} \cos\left(\frac{\pi\varphi}{2}\right) + \frac{1}{R_f} \quad (5.36)$$

From the slope of a plot of  $\log(Y_{\varphi}'')$  vs  $\log(\omega/\text{rad s}^{-1})$  we may determine the parameter  $\varphi$  at a particular electrode potential, (fig. 5.14). Using the value of  $\varphi$  obtained at a particular potential, and plotting  $Y_{\varphi}'$  vs  $\omega^{\varphi}$ , we can then

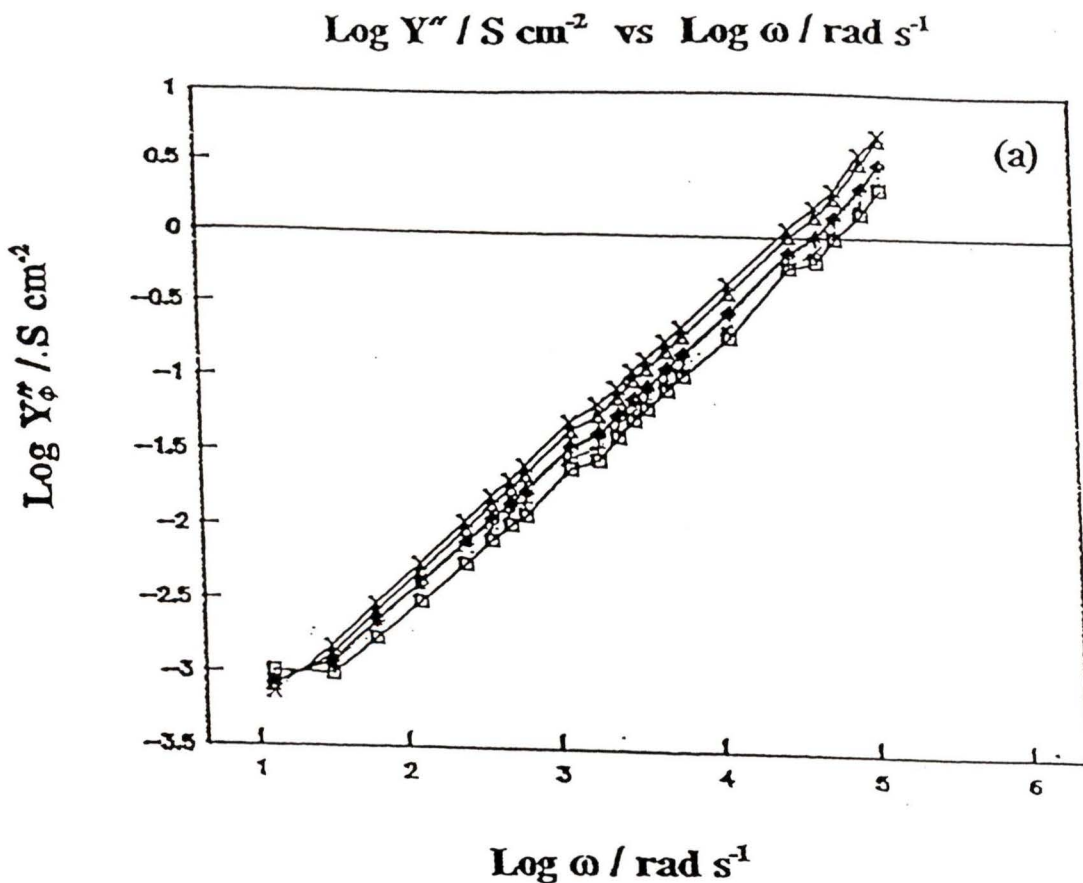


Figure 5.14 CPE sample plots to determine the CPE coefficient  $\varphi$ , hence  $C_d$  during the iodine oxidation reaction at potentials of 1207  $\square$ , 1257  $+$ , 1307  $\diamond$ , 1357  $\Delta$ , and 1407  $\times$  mV.

deduce the value of  $R_f$  from the reciprocal of the intercept (fig. 5.15) using linear regression analysis. The pattern of change of  $C_d$  and  $R_f$  with potential is shown in figs. 5.16 and 5.17 (pages 133 and 134) respectively. Note the sigmoidal rise of  $C_d$  with potential, and the minimum in  $R_f$  as the potential is increased. The latter observation is a direct verification to eq. 5.30.

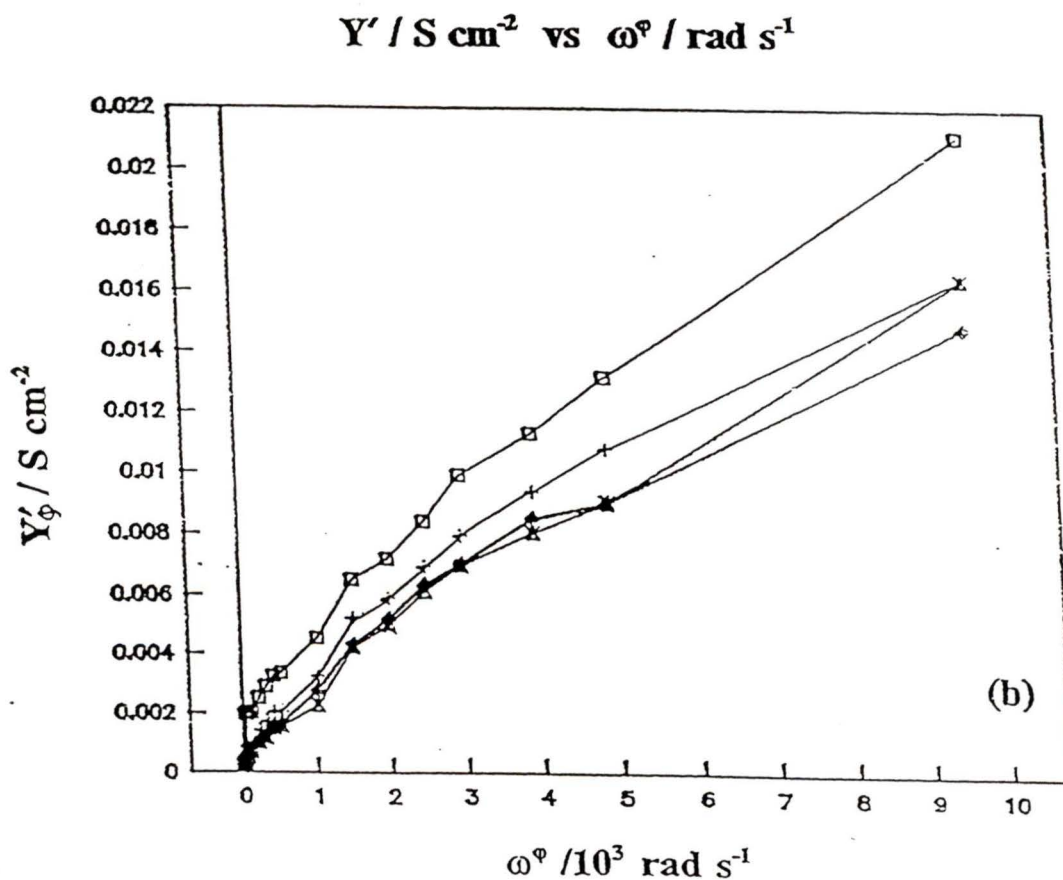


Figure 5.15 CPE sample plots to determine the  $R_f$  value during the iodine oxidation reaction at potentials of 1207  $\square$ , 1257  $+$ , 1307  $\diamond$ , 1357  $\triangle$ , and 1407  $\times$  mV.

Simulating the a.c. cyclic voltammogram:

$Y_f$  represents the admittance due to the reaction. But the total admittance  $Y_T$  in the a.c. cyclic voltammogram (fig. 5.18), plotted from experimental data, includes also both the solution resistance and double-layer capacitance. So, both quantities should be included in this calculation.

### DOUBLE LAYER CAPACITANCE vs POTENTIAL for iodine oxidation on Platinum

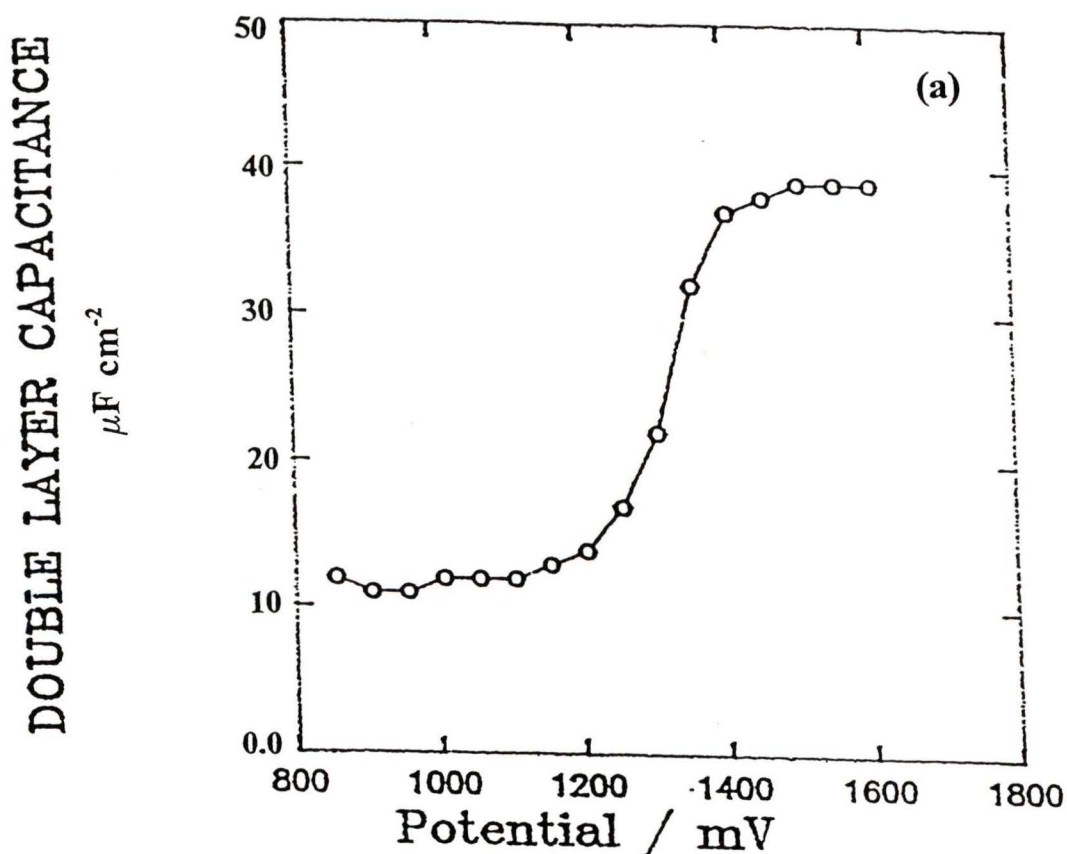


Figure 5.16 Change in the double layer capacitance/  $\mu\text{F cm}^{-2}$  with potential/ V during the iodine oxidation reaction.

The total admittance is calculated in the following way:

$$\tilde{Y}_{f-c_d} = \tilde{Y}_f + i\omega C_d \quad (5.37)$$

$$\Rightarrow \tilde{Z}_{f-c_d} = \frac{1}{\tilde{Y}_{f-c_d}} = \frac{1}{\tilde{Y}_f + i\omega C_d} \quad (5.38)$$

$$\text{but } \tilde{Z}_T = R_t + \tilde{Z}_{f-c_d} = R_t + \frac{1}{\tilde{Y}_f + i\omega C_d} \quad (5.39)$$

$$\therefore \tilde{Y}_T = \frac{1}{\tilde{Z}_T} = \frac{1}{R_t + \frac{1}{\tilde{Y}_f + i\omega C_d}} \quad (5.40)$$

Faradaic Resistance /  $\Omega \text{ cm}^2$  vs potential / V  
for iodine oxidation on platinum

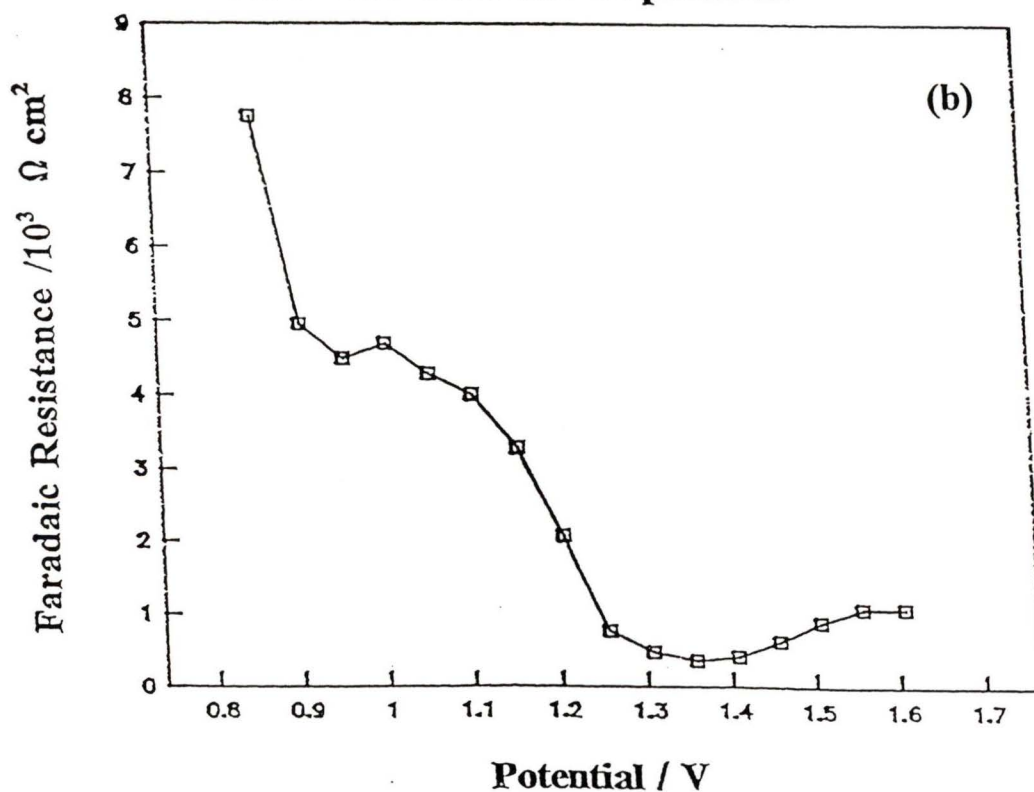


Figure 5.17 Change in the Faradaic Resistance/  $\Omega \text{ cm}^2$  with potential/ V during the iodine oxidation reaction.

Actually, we have already shown that the double-layer capacitance  $C_d$  is not constant but changes sigmoidally with potential fig. 5.16, hence it is necessary to replace  $C_d$  in eq.(5.40) by a relation which expresses this change. For a first approximation, we assumed that  $C_d$  changes linearly with the coverage:

$$C_d = C_h(1 - \theta_1) + C_l \quad (5.41)$$

Admittance( $Y'$ )/S cm<sup>-2</sup> vs Potential/V

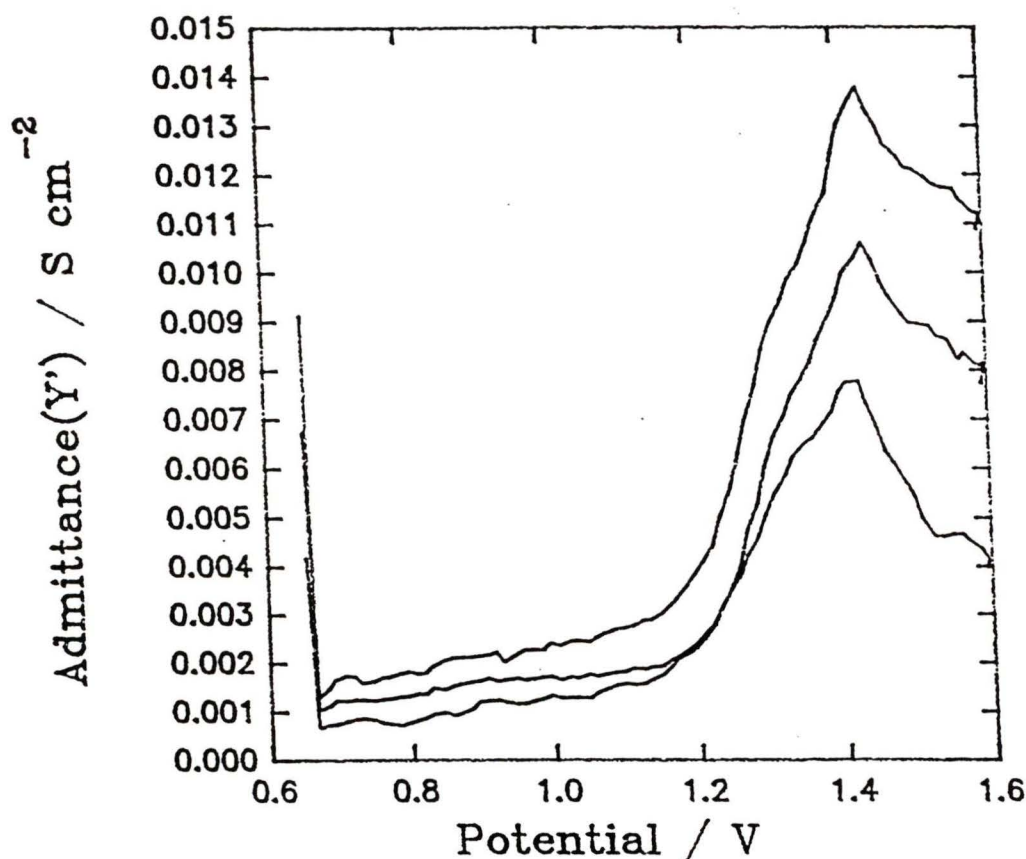


Figure 5.18 The observed a.c. cyclic voltammograms of iodine oxidation on platinum in  $H_2SO_4$  solution ( $1 \text{ mol dm}^{-3}$ ) at  $f=200$ ,  $300$ , and  $400 \text{ Hz}$ . Area of WE= $0.6 \text{ cm}^2$ ,  $\nu=0.01 \text{ V s}^{-1}$ .

where  $C_h$  and  $C_1$  are the double-layer capacitances appropriate to the oxide and iodine covered surfaces respectively. The value of  $\theta_1$  is substituted according to eq.(5.11) section(5.4.4). The complex quantity  $Y_T$  can be solved to find the real part of the admittance, appendix I.6.

The following data are appropriate for the experiment:

$$\begin{array}{lll} R_s = 0.45 \Omega \text{ cm}^2 & \nu = 10 \text{ mV s}^{-1} & E_s = 500 \text{ mV} \\ C_h = 40.0 \mu\text{F cm}^{-2} & A = 0.6 \text{ cm}^2 & \\ C_1 = 12.0 \mu\text{F cm}^{-2} & A_v = 0.059 \pm 0.003 \mu\text{C cm}^{-2} & \end{array}$$

and it is already known from section(5.4.4) that:

$$k_1^p = (5.8 \pm 1) \times 10^{-10} \text{ mol cm}^{-2} \text{ s}^{-1} \text{ at peak maximum.}$$

$$\beta = 0.63$$

Substituting these values in their respective equations, and working at frequencies of 200,300 and 400 Hz, the a.c. cyclic voltammograms shown in (fig. 5.19) were simulated. The simulated a.c. cyclic voltammograms are in semi-quantitative agreement with experiment.

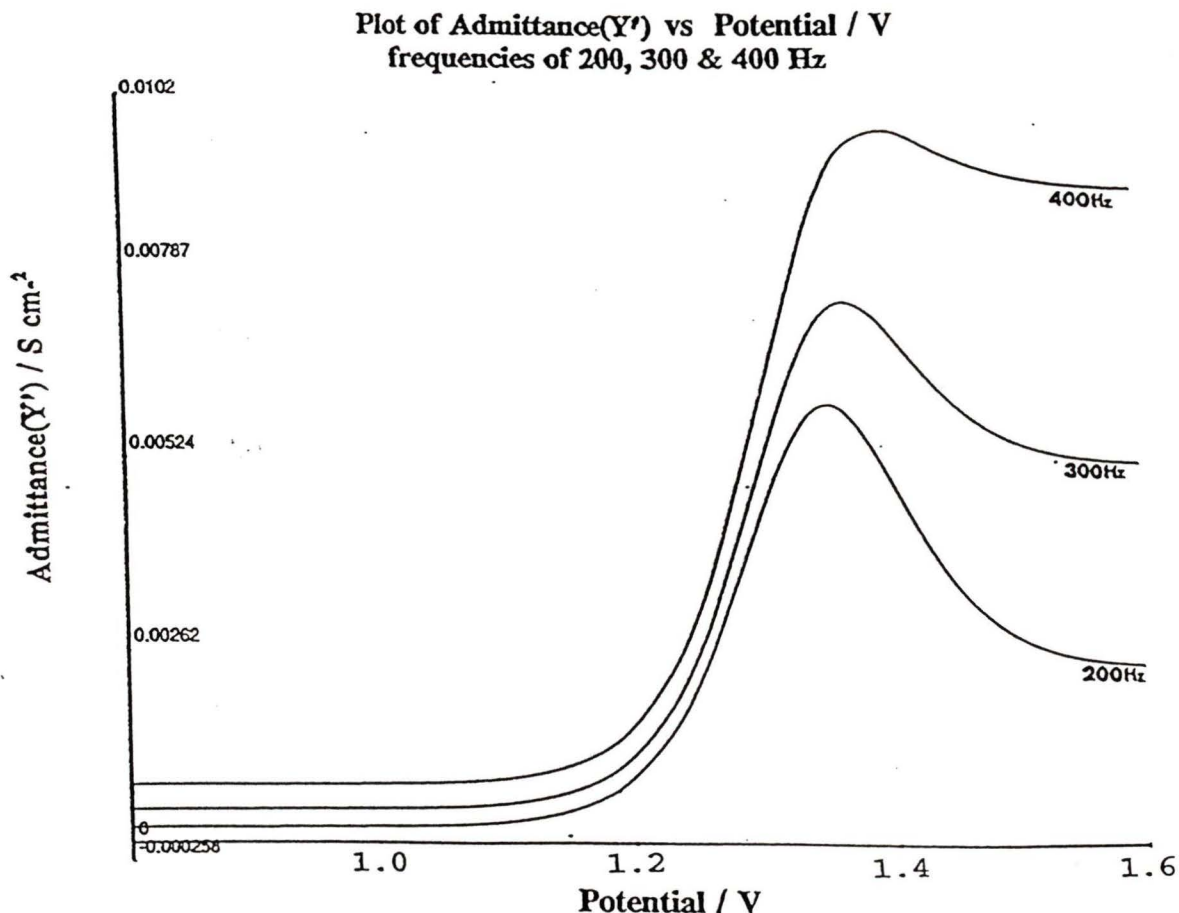


Figure 5.19 The calculated a.c. cyclic voltammograms of iodine oxidation on platinum in  $\text{H}_2\text{SO}_4$  solution ( $1 \text{ mol dm}^{-3}$ ) at  $f=200, 300, \text{ and } 400 \text{ Hz}$ . Area of  $\text{WE}=0.6 \text{ cm}^2$ ,  $\nu=0.01 \text{ V s}^{-1}$ .

### 5.1) Discussion:

Basically, this section discusses the experimental data presented in section 5.3, and the corresponding theoretical results obtained in section 5.4.

#### 5.5.1 ) The d.c. cyclic voltammogram (fig. 5.2):

The d.c. cyclic voltammogram clearly shows that when iodine is chemisorbed on a platinum surface it prevents the

formation of a hydrogen adlayer, and delays the oxidation of the platinum surface from 0.9 V to 1.2 V versus RHE. At this higher potential, the current density rises quickly due to the oxidation of both the iodine monolayer and platinum surface. The reason for the delay could be attributed to the following effects:

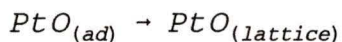
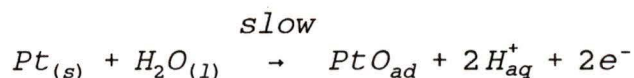
- 1) The chemisorbed iodine may sterically hinder the water molecules from coming into close contact with the surface.
- 2) The electron withdrawing effect of the iodine monolayer may cause partial passivation of the surface towards water molecules at +0.9 V.

When the linear sweep reverses no major changes are noticed.

#### 5.5.2 ) The a.c. cyclic voltammogram (figs. 5.3, 5.4):

The oxidation peak in the a.c. cyclic voltammogram of a pure acidic solution, (fig. 5.5) gave rise to two poorly resolved peaks due to platinum oxidation and surface restructuring, [85]. The trailing edge of the higher potential peak keeps falling until is nearly level with the background signal. The profile of the voltammogram basically stays the same at all frequencies suggesting that the first electron transfer is the rate determining step:

On the contrary, the oxidation peak due to the iodine



oxidation, (fig. 5.3), showed no structure at low frequencies (5 to 30 Hz). A slight hump appeared at the rising edge of the oxidation peak at 40 Hz and became more pronounced at 300 to 400 Hz (fig. 5.3). At this stage, a new hump appeared at the trailing edge of this peak. These humps could be indicating that reaction steps other than the rds are having some minor influence. In fact, in the derivation of the rate equations we did not consider other steps explicitly, section 5.4.5. The most noticeable feature is the trailing edge of the oxidation peak which did not stay at the same level with respect to the background signal, but rose as the frequency was increased. It was proved theoretically in section 5.4.5, that this rise is due to an increase in the double-layer capacitance with electrode potential as the reaction progresses towards formation a PtO monolayer.

### 5.5.3) The Bode plots:

In the double-layer region where the iodine is adsorbed on the surface of platinum (10mV to 1200mV), and no reactions are occurring, the faradaic resistance  $R_f$  is expected to be infinite. Consequently, the impedance should be that of an RC series circuit made from a combination of solution resistance

$R_t$  and double-layer capacitance  $C_d$  (fig. 5.13a). The phase and magnitude diagrams for an ordinary RC series circuit are shown schematically in the same figure. The phase and magnitude plots obtained from the a.c. impedance experiment show the same pattern of change (fig. 5.6).

As the potential was increased towards 1.2 V the circuit evolved from an RC series combination to the ( $R_t$  series ( $C_d$  parallel  $R_f$ )) combination shown in fig. 5.13b. The reason for this behaviour is the gradual drop of  $R_f$  as the potential became more positive. Theoretically, the change of phase with frequency for this circuit shows a maximum and our experimental results (fig. 5.7) also exhibit such a maximum. On the other hand, further mathematical analysis showed that the  $C_d$  is not simply a pure capacitor but a CPE (section 5.4.5), and therefore, the circuit takes a more complex form. It should be noted that the constant phase element has not adequately fitted the data. As the potential increases above 1.4 V, the reaction rate reduces to zero and the  $R_f$  rises again (as predicted from the reaction mechanism eq. (5.30)). At this stage, the circuit is again the RC series combination where the phase (fig. 5.8) is close to 90 degrees.

On the reverse sweep the RC series combination persists down to a potential of 0.75V, figs.(5.9) where the reduction of the platinum oxide occurs (there is also the possibility that some iodate is reduced to iodine). Here again there is a tendency towards forming a maximum (fig. 5.9), indicating a

drop in the faradaic resistance accompanying the reduction process.

#### 5.5.4) The Reaction Mechanism and Kinetics:

When the electrode potential is driven to high positive values, an electron withdrawing effect occurs from the adsorbed iodine monolayer towards the platinum surface leaving the adsorbed iodine adatoms with partial positive charge. Consequently, the repulsion between the iodine adatoms creates an unstable condition which is stabilised if two iodine adatoms coalesce to form an iodine admolecule with the liberation of one electron, (fig. 5.11). This is the rate determining step. Then the reaction proceeds until it leaves an exposed platinum site which is readily attacked by a water molecule to form PtO, a part of the oxide monolayer.

The suggested second order reaction for iodine oxidation on platinum looks acceptable since the simulated graphs (figs. 5.12 and 5.19), obtained from the suggested rate equation fitted the experimental ones to a good degree of accuracy. The value of the forward rate constant at peak maximum ( $k_1^p = (5.8 \pm 1) \times 10^{-10} \text{ mol cm}^{-2} \text{ s}^{-1}$ ) positioned the oxidation peak at the observed peak potential and the calculated value of  $R_f$  at peak potential ( $588 \pm 100 \text{ } \Omega \text{ cm}^{-2}$  from eq. 5.30) is close to the observed value,  $355 \pm 50 \text{ } \Omega \text{ cm}^{-2}$  (fig. 5.17) determined from the CPE analysis. The discrepancy is attributed to many factors:

- 1) Ignoring the faradaic capacitance in the suggested circuit

(fig. 5.13).

- 2) Locating the exact position of the peak potential.
- 3) Error in determining the experimental charge density due to noise in the CV, and assigning the exact values of surface area of the WE and the current measuring resistor. The latter problem is overcome by calculating the ratio  $V/A_v$  (section 5.4.4).
- 4) Determining the experimental  $R_f$  value from CPE-linear regression analysis (fig. 5.15). The value of  $R_f$  from the Nyquist plot was estimated at  $400 \Omega \text{ cm}^{-2}$  assuming that the plot is a semi-circle.

The value of the symmetry factor ( $\beta=0.63$ ) has fitted the width of the calculated peak to the observed oxidation peak. In fact,  $\beta$  and the rate constant are quite interrelated in determining the exact position of the oxidation peak along the potential axis.

#### 5.6) Conclusion:

According to the suggested reaction mechanism the iodine oxidation reaction is a second order process represented by a series combination of a faradaic capacitance ( $C_f$ ) and a faradaic resistance ( $R_f$ ) where the contribution from the  $C_f$  part to the faradaic admittance was shown to be insignificant at frequencies above 2 Hz. Therefore, the process is largely represented by  $R_f$ . The suggested rate equation (eq. 5.5) has predicted that  $R_f$  goes through a minimum as the reaction

progresses (i.e. as the potential is increased), and this prediction was verified experimentally, (fig. 5.15). In addition, the calculated ( $588 \pm 100 \Omega \text{ cm}^{-2}$  from eq. 5.30) and observed ( $355 \pm 50 \Omega \text{ cm}^{-2}$  from fig. 5.17) values of  $R_f$  are relatively close. The reaction occurs via a multiple step mechanism where the first step is the rate determining step and the rest are assumed to be relatively fast processes. The value of the forward rate constant of the oxidation of adsorbed iodine on platinum at peak potential of 1.4 V is  $k_1^p = (5.8 \pm 1) \times 10^{-10} \text{ mol cm}^{-2} \text{ s}^{-1}$ , while that of the symmetry factor is 0.63 which proves that the first charge transfer step, which involves one electron, is the rate determining step. In the reaction region, between 1.2V and 1.6V vs RHE, the double-layer capacitance is a constant phase element in which  $C_d$  was found to change linearly with coverage. The suggested rate equation has faithfully reproduced the observed d.c. and a.c. cyclic voltammograms.

Further work could involve non-linear least-square fitting of the a.c. data to get the optimized values of  $k_1$  and  $\beta$ . Eq. (5.15) could also be extended to include other intermediates which would likely improve the agreement with the shape of the a.c. cyclic voltammogram.

## CHAPTER SIX

Conclusion

The aim of this thesis was directed towards studying the kinetics of the hydrogen sorption and the iodine oxidation electrochemical reactions. In both areas, mechanistic information including new experimental values of the rate constant and symmetry factor, was obtained. The value of the standard overall rate constant of H-sorption on platinum was  $2.5 \times 10^{-6} \text{ mol cm}^{-2} \text{ s}^{-1}$  and  $2.52 \times 10^{-6} \text{ mol cm}^{-2} \text{ s}^{-1}$  for 1M  $\text{H}_2\text{SO}_4$  and 1M  $\text{HClO}_4$  solutions respectively. This shows that the effect of the anion on the rate constant is negligible. The values of  $k_1^\circ$  and  $k_{-1}^\circ$  were  $0.97 \times 10^{-6} \text{ mol cm}^{-2} \text{ s}^{-1}$  and  $1.62 \times 10^{-6} \text{ mol cm}^{-2} \text{ s}^{-1}$  respectively. The value of the symmetry factor is 0.32. The rate constant of the iodine oxidation reaction on platinum was determined at peak potential to be  $5.8 \pm 1 \times 10^{-10} \text{ mol cm}^{-2} \text{ s}^{-1}$  and the corresponding value of the symmetry factor is 0.63.

The Sweep-Step method was used to study the hydrogen sorption reaction. It is a transient technique and it is crucial to confirm that its response performance is such that the signal is due to real electrochemical reactions on the surface, while the effects of the double-layer capacitance and solution resistance are minimal. A transfer function analysis of the electrochemical system allowed us to study the effect of the non-faradaic parameters on the response of a

potentiostat. The results obtained in this analysis can be utilized by experimentalists working in the same area of research.

The Sweep-Step method was shown to be a successful method for studying the hydrogen sorption reaction. For example, we were able to detect the change in the kinetic parameters as a function of potential for hydrogen desorbing from different crystallographic facets (i.e. Pt(100) and Pt(111)). Moreover, the potential dependence of the rate constants showed that :

- 1) The time constant of the hydrogen desorption reaction depended only on the final potential, and not on the potential programme before the step, i.e. memory effects such as might be attributed to surface diffusion were absent.
- 2) The reaction obeys simple Langmuir kinetics to a good approximation. An exception is that it fails to explain the details of the change of the overall rate constant with the sign of the potential step. This phenomenon is worth investigating in future to determine an improved rate equation.

A.c. voltammetry was used to study the adsorbed iodine monolayer on platinum, the oxidation of the adsorbed iodine to  $\text{IO}_3^-$  and the PtO layer left after oxidation.

Enough results were obtained in the frequency range we studied to carry out thorough theoretical analysis. A reaction mechanism was put forward to describe the oxidation reaction. The mechanism produced good agreement between observed and

simulated results of both d.c. and a.c. voltammograms. The calculated faradaic resistance of  $588 \pm 100 \Omega \text{ cm}^2$  is close to the observed value of  $355 \pm 50 \Omega \text{ cm}^2$ . The circuit which characterises this reaction is a faradaic resistor in series with a faradaic capacitor ( $4201 \mu\text{F cm}^{-2}$  at  $E_p$ ) where the capacitor has little influence above 2 Hz. In future work, this reaction should be studied at a lower frequency range (0.01 Hz to 2 Hz) in order to detect any other faradaic processes that might be influencing the kinetics. The reaction could be investigated by other experimental techniques giving direct structural information. This would help to confirm our hypothesis that the oxidation reaction is initiated by repulsive deformation of the iodine adlayer, due to increasing potential, and that oxo-groups like PtO, PtOH, and Pt(H<sub>2</sub>O) are not required for the initial event.

REFERENCES:

- 1) G.L. Booman and W.B. Holbrook, *Anal. Chem.*, 35 (1963) 1793-1809.
- 2) G.L. Booman and W.B. Holbrook, *Anal. Chem.*, 37 (1965) 795-802.
- 3) W.M. Schwarz and I. Shain, *Anal. Chem.*, 35 (1963) 1770-1778.
- 4) J.E. Harrar and I. Shain, *Anal. Chem.*, 38 (1966) 1148-1158.
- 5) J.E. Mumby and S.P. Perone, *Chem. Instrumentation*, 3 (1971) 191-227.
- 6) Ronald R. Schroeder and I. Shain, *Chem. Instrumentation*, 1 (1969) 233-259.
- 7) D.E. Tallman, G. Shepherd and W.J. Mackellar *J. Electroanal. Chem.*, 280 (1990) 327-340.
- 8) P. Jayaweera and I. Ramaley, *Anal. Instrumentation*, 15 (1986) 259-277.
- 9) E.R. Brown, H.L. Hung, T.G. McCord, D.E. Smith, and G. Booman, *Anal. Chem.*, 40 (1968) 1424.
- 10) J.E. Harrar and C.L. Pomernaki, *Anal. Chem.*, 45 (1973) 57.
- 11) W.C. Carter, *Instrum. Contr. Syst.*, 40 (1967) 107.
- 12) D.T. Pence, and G.L. Booman, *Anal. Chem.*, 38 (1966) 1112.
- 13) D.D. Macdonald, *Transient Techniques in Electrochemistry*, Plenum press, New York.
- 14) E.V. Bohn, *The Transform Analysis of Linear Systems*, Addison-Wesley, Massachusetts, 1963.
- 15) F.G. Will and C.A. Knorr, *Z. Elektrochem.* 64 (1960) 258-270.
- 16) B.E. Conway and E. Gileadi, *Transactions of the Faraday Society*, 58 (1962) 2493.

- 17) S. Srinivasan and E. Gileadi, *Electrochimica Acta* 11 (1966) 321-335.
- 18) H. Angerstein-Kozłowska, J. Klinger and b.E. Conway, *J. Electroanal. Chem.*, 75 (1977) 45-60.
- 19) B.E. Conway, E. Gileadi and H. Angerstein-Kozłowska, *J. Electrochem. Soc.*, 112 (1965) 341.
- 20) E.K. Krauskopf, L.M. Rice and A. Wieckowski, *J. Electroanal. Chem.*, 244 (1988) 347-352.
- 21) K. Christmann and G. Ertl, *Surface Science*, 60 (1976) 365-384.
- 22) D. Armand and J. Clavilier, *J. Electroanal. Chem.*, 233 (1987) 251-265.
- 23) J. Clavilier, *J. Electroanal. Chem.*, 107 (1980) 211.
- 24) R. Parsons, *J. Electroanal. Chem.*, 318 (1991) 1-24.
- 25) M.P. Soriaga, *Ultra High Vacuum techniques in the study of single crystal electrode surfaces in progress in surface science*, S.G. Davidson, Ed., in press, 1993, *Chap.* 3.
- 26) A.T. Hubbard, R.P. Ishikawa and J. Katekaru, *J. Electroanal. Chem.*, 86 (1978) 271.
- 27) G.G. Will, *J. Electrochemical Society*, 112 (1965) 451.
- 28) (a) D. Armand, J. Clavilier, S.G. Sun and M. Petit, *J. Electroanal. Chem.*, 205 (1986) 267-277.  
(b) B. Love, K. Seto and J. Lipkowski, *J. Electroanal. Chem.*, 199 (1986) 219-228.
- 29) H. Kita, S. Ye, A. Aramata and N. Furuya, *J. Electroanal. Chem.*, 295 (1990) 317-331.
- 30) J. Clavilier, J. Ganon and M. Petit, *J. Electroanal. Chem.*, 265 (1989) 231-245.
- 31) J. Clavilier, *J. Electroanal. Chem.*, 127 (1981) 281-287.
- 32) (a) D. Armand and J. Clavilier, *J. Electroanal. Chem.*, 135 (1982) 159-166. (b) *ibid* 199 (1986) 187-200.
- 33) P.N. Ross, *Surf. Sci.*, 102 (1981) 463-485.
- 34) K. Al-Jaaf-Golze, D.M. Kolb and D. Scherson,

- J. Electroanal. Chem., 200 (1986) 353.
- 35) S. Motoo and N. Furuya, Ber. Bunsenges. Phys. Chem., 91 (1987) 457-461.
- 36) D. Armand and J. Clavilier, J. Electroanal. Chem., 263 (1989) 109-126.
- 37) D. Armand and J. Clavilier, J. Electroanal. Chem., 270 (1989) 331-347.
- 38) M.P. Soriaga, Electrochemical Surface Science-Molecular Phenomenon at Electrode Surfaces, ACS, Washington, DC 1988, Chaps. 3,14 and 34.
- 39) R.J. Nichols and A. Bewick, J. Electroanal. Chem. 243 (1988) 445-453.
- 40) H. Angerstein-Kozłowska, and B.E. Conway, J. Electroanal. Chem., 95 (1979) 1-28.
- 41) R. Durand, Electrochimica Acta 24 (1979) 1095-1100.
- 42) V.I. Lukyanycheva, Soviet Electrochemistry, 7, (1971) 267-271.
- 43) P. Dolin and B. Ershler, Acta Physicochimica U.R.S.S, 13 (1940) 747.
- 44) M.W. Breiter, in Symposium on Electrode Processes, Electrochem. Society, John Wiley, New York, 1961, p.307.
- 45) M.W. Breiter, C.A. Knorr and W. Volk, Z. Elektrochem. 59 (1955) 681.
- 46) D.R. Flinn and S. Schuldiner, Electrochimica Acta, 19 (1974) 421-425
- 47) A.T. Hubbard, R.A. Osteryoung and F.C. Anson, Anal. Chem., 38 (1966) 692.
- 48) R. Flane, A.T. Hubbard, The J. Phys. Chem., 79 (1975) 808-815.
- 49) M.P. Soriaga, Chem. Rev., 90 (1990) 771-793.
- 50) J.F. Rodriguez, Inorg. Chim. Acta., 148 (1988) 123-131.
- 51) A.T. Hubbard, Chem. Rev. , 88 (1988) 633.

- 52) J.L. Stickney, S.D. Rosasco, D. Song, M.P. Soriaga, and A.T. Hubbard, *Surf. Sci.*, 130 (1983) 326.
- 53) V.A. Safonov, M.D. Faerman, V.N. Andreev, V.E. Kazarinov and O.A. Petrii, *Elektrokhimiya*, 12 (1976) 834.
- 54) N.A. Balashova, *Z. Phys. Chem. (Leipzig)* 207 (1957) 340.
- 55) G. Horanyi and E.M. Rizmayer, *J. Electroanal. Chem.*, 83 (1977) 367.
- 56) R.A. Osteryoung, *Anal. Chem.*, 35 (1963) 1100.
- 57) R.A. Osteryoung and F.C. Anson, *Anal. Chem.*, 36 (1964) 975.
- 58) R.A. Osteryoung, G. Lauer and F.C. Anson, *J. Electrochem. Soc.*, 110 (1963) 926.
- 59) D.S. Austin, D.C. Johnson, *Anal. Chem.*, 55 (1983) 2222-2226.
- 60) J.W. Schultze, *Electrochim. Acta*, 21 (1977) 327.
- 61) G.A. Garwood, A.T. Hubbard, *Surf. Sci.*, 92 (1980) 617.
- 62) J.L. Stickney, S.D. Rosasco, G.N. Salaita and A.T. Hubbard, *Langmuir*, 1 (1985) 66.
- 63) T.E. Felter and A.T. Hubbard, *J. Electroanal. Chem.*, 100 (1979) 473.
- 64) M.P. Soriaga, *J. Electroanal. Chem.*, 240 (1988) 309-315.
- 65) J.H. White and H.D. Abruna, *J. Phy. Chem.*, 92 (1988) 7131-7134.
- 66) F. Lu, G.N. Salaita, H. Baltruschat and A.T. Hubbard, *J. Electroanal. Chem.*, 222 (1987) 305-320.
- 67) L.C. Pauling, *The Nature of the Chemical Bond*, 3rd. Edition, Cornell, Ithaca, NY, 1960.
- 68) S.B. Diczno, G.K. Wertheim and D.N.E. Buchanan, *Physical Review B*, 30 (1984) 553-557.
- 69) S.K. Jo and J.M. White, *Surf. Sci.*, 261 (1992) 111-117.
- 70) N.C. Gibson, P.M. Saville and D.A. Harrington, *J. Electroanal. Chem.*, 318 (1991) 271-282.

- 71) T. Mebrahtu, J.F. Rodriguez, B.G. Bravo and M.P. Soriaga, *J. Electroanal. Chem.*, 219 (1987) 327-333.
- 72) M.L. Lynch, B.G. Barner and R.M. Corn, *J. Electroanal. Chem.*, 300 (1991) 447-465.
- 73) B.C. Schardt, S.Y. Yau, F. Rinaldi, *Science*, 243 (1989) 1050
- 74) S.C. Chang, S. Yau, B.C. Schardt and M.J. Weaver, *J. Phy. Chem.* ,95 (1991) 4787-4794.
- 75) B.C. Schardt, S.Y. Yau, F. Rinaldi, *Science*, 243 (1989) 981.
- 76) R. Vogel and H. Baltruschat, *Surf. Sci. lett.*, 259 (1991) L739-L742.
- 77) T. Solomun, A. Wieckowski, S.D. Rosasco, and A.T. Hubbard, *Surf. Sci.*, 147 (1984) 241.
- 78) A.T. Hubbard, *J. Vac. Sci. Technol.*, 17 (1980) 49-54.
- 79) T. Bejerano, E. Gileadi, *J. Electroanal. Chem.*, 82 (1977) 209-225.
- 80) S. Swathirajan and S. Buckenstein, *J. Electroanal. Chem.*, 143 (1983) 167-178.
- 81) S. Swathirajan and S. Bruckenstein, *J. Electroanal. Chem.*, 125 (1981) 63-71.
- 82) R. Guidelli and G. Piccardi, *Anal. Lett.* , 1 (1968) 779.
- 83) V.I. Astashko, *Khimija I Kimicheskaja Tekhnologia (Minsk)*, 1 (1987) 33-37.
- 84) J.O'M. Bockris and A.K.N. Reddy, *Modern Electrochemistry* vol. 2, Plenum, New York, 1973, *Chapter 9*.
- 85) D.V. Heyd and D.A. Harrington, *J. Electroanal. Chem.*, 335 (1992) 91-31.

APPENDIX I

I.1) For a system whose input starts at  $t=0$  and whose output and derivatives have zero values at  $t=0$ , we can write :

$$\mathcal{L}\{k y(t)\} = k \mathcal{L}\{y(t)\} \quad k = \text{constant}$$

$$\mathcal{L}\left\{\frac{dy(t)}{dt}\right\} = s \mathcal{L}\{y(t)\}$$

$$\mathcal{L}\left\{\frac{d^2y(t)}{dt^2}\right\} = s^2 \mathcal{L}\{y(t)\}$$

$$\text{when, } y(0) = y'(0) = y''(0) = 0$$

I.2) The formulae for the transfer functions (TF) at all the junctions are :

$$\frac{\overline{e_{op}}}{\overline{e_i}} = \frac{-gf_b(CC_d(R_t + R_u + R_l) s + C + C_d)}{D}$$

where,

$$D = 2C_d C(R_t + R_u + R_l) s^2 + f_b C_d C[2(R_t + R_l) + R_u(g+2) + 2(C + C_d)] s + f_b[(g+2)C + 2C_d]$$

$$\frac{\overline{e_c}}{\overline{e_i}} = \frac{-gf_b[CC_d(R_t + R_u) s + C + C_d]}{D}$$

$$\frac{\overline{e_t}}{\overline{e_i}} = \frac{-gf_b C[C_d(R_t + R_u) + 1]}{D}$$

$$\frac{\overline{e_s}}{\overline{e_i}} = \frac{CC_d(R_l + R_u + R_t) s^2 + [f_b CC_d(R_l + R_u + R_t) + C + C_d] s + f_b(C + C_d)}{D}$$

$$\frac{\overline{e_{out}}}{\overline{e_i}} = \frac{-gf_b C(R_u C_d s + 1)}{D}$$

$$\frac{\overline{e_d}}{\overline{e_i}} = \frac{-gf_b C}{D}$$

I.3) Formulae for the magnitude and the phase of the transfer function at the tip of the luggin probe (LP) of the reference electrode (RE), (i.e.  $e_{out}/e_i$ ).

The magnitude is :

$$\frac{gf_b C \sqrt{(\omega C_d R_u)^2 + 1}}{\sqrt{D_m}}$$

where  $D_m$  is :

$$\begin{aligned} D_m = & 4C_d C [gf_b (f_b + \omega^2 C_d R_u) + \omega^4 C_d C R_t^2 \\ & (R_l + R_t) \{ (\omega C)^2 [ (f_b C_d)^2 (8+g) R_u - 2gf_b C_d ] \} \\ & + (2f_b \omega C_d C)^2 (R_l + R_t)^2 + 4(C_d + C)^2 (\omega^2 + f_b^2) \\ & + 4(\omega C_d C)^2 [ (R_l + R_u) + \omega^2 R_t ]^2 - 4\omega^4 R_t^2 \\ & + (g+2)^2 \{ (f_b C)^2 [ (\omega C_d R_u)^2 + 1 ] \} - 4 \end{aligned}$$

and the phase in degrees is :

$$57.3 \arctan \left( 2\omega \frac{N_p}{D_p} \right)$$

where

$$\begin{aligned} N_p = & f_b C_d [ C(R_l + R_t) + C_d R_u ] + \omega^2 C_d^2 C R_u (R_u + R_t + R_l) \\ D_p = & 2(f_b (C_d + C) + \omega^2 C_d [ -C(R_l + R_t) \\ & + C_d R_u \{ f_b C [ R_u (g+1) + R_t + R_l ] + 1 \} ] ) \end{aligned}$$

I.4) The output signal, occurring at the LP of the RE, due to an applied step signal, is :

$$y(t)_{out} = \frac{-gC\{\sqrt{X}\cosh U + \sinh U[f_b C_d(R_u(4C_d + C(g+2) + 2R_t C) + 2(C_d + C)) - \sqrt{X}\exp W]\}}{\sqrt{X}}$$

where,

$$\begin{aligned} X = & (f_b C C_d)^2 [(R_u(g+2) + 2(R_t + R_l))]^2 \\ & + f_b C C_d^2 [4R_u(g-2) - 8(R_t + R_l)] \\ & - f_b C^2 C_d [4R_u(g+2) + 8(R_t + R_l)(g+1)] \\ & + 4(C_d + C)^2 \end{aligned}$$

$$U = \frac{1}{4} \frac{\sqrt{X}}{C_d C (R_u + R_t + R_l)} t$$

$$W = -\frac{1}{2(R_u + R_t + R_l)} \left\{ f_b [R_l + R_t + R_u \left(1 + \frac{g}{2}\right)] + \frac{1}{C} + \frac{1}{C_d} \right\} t$$

I.5) The output voltage drop signal across the load resistor is :

$$y(t)_{vd} = \frac{-2g f_b C C_d R_l \sinh(U) \exp W}{\sqrt{X}}$$

I.6) The real part of the total admittance is equal to :

$$\frac{R_t + \frac{L}{L^2 + M}}{\left(R_t + \frac{L}{L^2 + M}\right)^2 + \frac{M}{(L^2 + M)^2}}$$

where,

$$L = Fb k_s \exp(b(E - E_s)) \theta_1^2 \left[ 1 - \frac{1}{1 + \left( \frac{\omega}{V k_s \exp(b(E - E_s)) \theta_1} \right)^2} \right]$$

and,

$$M = \left\{ \omega C_d + \frac{Fb \theta_1 \omega}{V \left[ 1 + \left( \frac{\omega}{V k_s \exp(b(E - E_s)) \theta_1} \right)^2 \right]} \right\}^2$$

$$\text{where, } V = \frac{\sigma_m}{2Fb}$$

#### I.7) Specifications of the OP 27 Op-amp :

-Input Offset Voltage	0.2 $\mu$ V / month
-Bias Current	20.0 nA
-Gain Bandwidth	8.0 MHz
-Slew Rate	2.8 V / $\mu$ s
-Open Loop Gain	1.8 million
-Noise	3.0 nV / $\sqrt{\text{Hz}}$ at 1.0 kHz

#### 2) Specifications of the LM 6321 Op-amp :

-Peak output current	300 mA
-High input impedance	5.0 M $\Omega$
-High Slew Rate	800 V / $\mu$ s
-Wide Bandwidth	50 MHz
-No oscillations with capacitive loads	

VITA

Surname: FARHAT

Given Names: TAREK RAFIC

Place of Birth: LEBANON

Date of Birth: 15 APRIL 1964

Educational Institution Attended:

Queen Mary College 1986 to 1988

Thames Polytechnic 1989 to 1990

Degrees Awarded:

B.Sc. (Honours) Thames Polytechnic 1990

PARTIAL COPYRIGHT LICENSE

I hereby grant the right to lend my thesis to users of the University of Victoria Library, and to make single copies only for such users or in response to a request from the Library of any other university, or similar institution, on its behalf or for one of its users. I further agree that the permission for extensive copying of this thesis for scholarly purposes may be granted by me or a member of the University designated by me. It is understood that copying or publication of this thesis for financial gain shall not be allowed without my written permission.

Title of the Thesis:

ELECTROCHEMICAL STUDIES OF THE HYDROGEN SORPTION AND THE  
IODINE OXIDATION REACTIONS ON PLATINUM

Author



(Signature)

TAREK RAFIC FARHAT

\_\_\_\_\_  
(Name in Block Letters)

27th Sep 1993  
(Date)